VŠB – TECHNICAL UNIVERSITY OF OSTRAVA
FACULTY OF MECHANICAL ENGINEERING
Department of Hydrodynamics and Hydraulic Equipment

Doctoral thesis

NUMERICAL SIMULATION OF THE FLOW IN HYDRODYNAMIC PUMP

Study program:	**P2301 Mechanical Engineering**
Field:	**3901V003 Applied Mechanics**
Supervisor:	**doc. Ing. Drábková Sylva, Ph.D.**
PhD student:	**Ing. Phan Tran Hong Long**

Ostrava 2012

Acknowledgements

I would like to thank doc. Ing. Sylva Drábková Ph.D., my Ph.D. supervisor. With her enthusiasm, she provided me materials, knowledge in my thesis-writing period.

I am grateful to prof. Ing. Jaroslav Janalík, CSc. and prof. RNDr. Milada Kozubková, CSc., whose helped me when I began studying in Czech Republic.

I would also like to thank prof. Ing. František Pochylý and Ing. Pavel Rudolf Ph.D. who helped me when I visited the lectures at Brno University of Technology.

I wish to thank my colleagues in departerment, my parents, and my family for providing a loving environment for me.

Annotation

This thesis deals with numerical modelling of the flow inside the hydrodynamic pump with low specific speed. The geometry of the hydraulic parts was defined according to pump with the impeller that was designed at the Victor Kaplan Department of Fluid Engineering, Energy Institute, Technical University Brno.

The main objective was to determine pump performance characteristics (variation of head, power consumption and efficiency on the flow rate) as well as radial and axial forces using computational fluid dynamics. Two approaches to rotor stator interaction were applied: Moving Reference Frame and Moving Mesh. The method MRF provides only stationary solution of values, but the Moving Mesh approach shows time variation of them and enables to account for interaction of impeller and volute. Different turbulence models and solution parameters were tested. The entire operating range from $Q = 0$ to Q_{max} considered in the design was investigated.

Most of the calculation was performed on simplified geometry consisting only of three parts: intake, impeller and volute. In case of axial thrust prediction the geometry including also the pump casing was applied. The obtained results were compared with the experimental data and the theoretical assumptions. Both advantages and limitations of the numerical modelling are presented. The applied methods can be utilized as an appropriate approach to treat complex turbulent flow encountered in hydraulic machines.

Anotace

Předmětem disertační práce je numerické modelování proudění v hydrodynamickém čerpadle s nízkou hodnotou rychloběžnosti. Geometrie čerpadla byla definována na základě skutečné realizace čerpadla navrženého na Odboru fluidního inženýrství Victora Kaplana VUT v Brně.

Hlavním cílem práce je predikce charakteristik čerpadla (průběh dopravní výšky, příkonu a účinnosti v závislosti na průtoku) a dále určení radiální a axiální síly v celém rozsahu vyšetřovaných průtoků. Byly použity dva rozdílné přístupy k modelování statoru a rotoru, a to technika Multiple Referce Frame vedoucí na stacionární řešení úlohy a Moving Mesh spočívající v řešení časově závislé úlohy.

Většina výpočtů byla realizována pro zjednodušenou geometrii sestávající ze vstupní části, oběžného kola a spirály. V případě predikce axiální síly byla tato geometrie doplněna i o vlastní těleso čerpadla. Výsledky získané pomocí numerického modelování byly srovnány s měřenými charakteristikami čerpadla i teoretickými předpoklady.

Je poukázáno na přínos numerického modelování pro vyšetřování proudění v komplexní geometrii hydraulických strojů stejně jako i na určitá omezení.

Content

List of figures

List of tables

Nomenclature

ROMAN LETTERS

Symbol	***Unit***	***Quantity***
b	[m]	width of channel in the meridional section
b_2	[m]	impeller outlet width
c	$[m.s^{-1}]$	absolute velocity
c_m	$[m.s^{-1}]$	meridional velocity
c_u	$[m.s^{-1}]$	circumferential component of absolute velocity
d	[m]	general diameter
f	$[s^{-1}]$	frequency
g	$[m.s^{-2}]$	acceleration due to gravity
h	[m]	height
k	$[m^2.s^{-2}]$	turbulent kinetic energy
l	[m]	length
n	$[rad.s^{-1}]$	rotational speed
n_s	$[rad.min^{-1}]$	specific speed
p	$[N.m^{-2}]$, [Pa]	pressure, static pressure
q	$[m^3.s^{-1}]$	volumetric flow rate of flow back
r	[m]	radial coordinate in turbo machine, radius
t	[s]	time
u	$[m.s^{-1}]$	velocity, peripheral velocity of impeller or tangential velocity of impeller
u_i	$[m.s^{-1}]$	velocity component
v	$[m.s^{-1}]$	velocity
w	$[m.s^{-1}]$	relative velocity
z	[m], [1]	elevation, number of blades
A	$[m^2]$	cross-sectional area
C_L	[1]	lift coefficient
C_M	[1]	momentum coefficient
C_D	[1]	emprical constant
D	[m]	diameter
E	$[J.kg^{-1}]$	specific energy
F	[N]	force
F_a	[N]	axial thrust
F_r	[N]	radial force
H	[m]	total head rise
K	[1]	coefficient
M	[N.m]	moment, torque
P	[W], [kW]	power
P_h	[W], [kW]	hydraulic power
Q_v	$[m^3.s^{-1}]$, $[dm^3.s^{-1}]$	flow rate, capacity

Q_m	[kg.s^{-1}]	mass flow rate
R	[m.s^{-2}]	force per unit mass
Re	[1]	Reynolds number
S	[m^2]	area of volute's cross-section
T	[N.m]	torque
V	[m^3]	volume
Y	[J.kg^{-1}]	specific energy
Y^+, Y^*	[1]	distance between the cell centroid and the wall for wall-adjacent cell (wall unit)

GREEK LETTERS

Symbol	***Unit***	***Quantity***
α	[^{o}], [rad]	angle of the absolute velocity vector from the circumferential direction
β	[^{o}], [rad]	angle of the relative velocity vector from the circumferential (tangential) direction
γ	[N.m^{-3}]	specific weight
ε	[m^2.s^{-3}]	turbulent dissipation rate
φ	[^{o}], [rad]	orientation angle
η	[1], [%]	pump efficiency
η_h	[1], [%]	hydraulic efficiency
η_v	[1], [%]	volumetric efficiency
η_m	[1], [%]	mechanical efficiency
μ	[Pa.s]	dynamic viscosity
μ_t	[Pa.s]	turbulent viscosity
μ_{eff}	[Pa.s]	effective viscosity
ν	[m^2.s^{-1}]	kinematic viscosity
ρ	[kg.m^{-3}]	density of fluid
σ_k	[1]	emprical constant
σ_ε	[1]	emprical constant
φ	[^{o}], [rad]	orientation angle
ω	[rad.s^{-1}]	angular velocity
ω	[s^{-1}]	specific dissipation rate

SUBSCRIPTS on any variable, Q:

Q_0	initial value, total value
Q_1	value at the impeller blade leading edge
Q_2	value at the impeller blade trailing edge
Q_n	nominal value
Q_r	component in the radial direction
Q_s	component in the *s* direction
Q_{th}	theoretical value (for theoretical flow conditions)
Q_i	pertaining to a section, *i*, of the hydraulic system
Q_{opt}	operation at maximum (best) efficiency (BEP)
Q_{sp}	value at seal (Figure 52)

ABBREVIATIONS

BEP	Best Efficiency Point
CFD	Computational Fluid Dynamics
DNS	Direct Numerical Simulation
LES	Large Eddy Simulation
MRF	Moving Reference Frame model
NPSH	Net Positive Suction Head
RAM	Reynolds-Averaged model
RANS	Reynolds-Averaged Navier-Stokes (equations)
RNG	Re-Normalization Group
SMM	Sliding Mesh Model
SST	Shear Stress Transport

Remark: Other variables that are not mentioned here are explained in the text.

1. Introduction

Pumps are used very commonly to provide liquids transport through hydraulic systems, thus they are very important. Pumps are used in water supply for agriculture, industry, human life, and other liquid handling applications. Some products are used in fluid flow and heat transfer applications, others are designed to transport coolants. The pumping system is defined by the type of the pump, material of construction, type of pumped liquid, field of applications, pressure and flow rate, and other aspects.

In Vietnam, the first pumping station was built in 1928, completed in 1932, equipped with three vertical centrifugal pumps run with oil engine, providing flow rate around 9 $m^3.s^{-1}$. Through different periods, in the North of Vietnam, other types of pumps have been used mostly from the Soviet Union, in the South of Vietnam, the U.S. and Japan pumps are often applied. Currently, most types of small pumps are of domestic production, while other lager types are imported from various countries in the world, depending on investors or the designing company. The largest domestic producer is Hai Duong Pump Manufacturing Joint Stock Company with the web site in English: <http://www.hpmc.com.vn/Homepage/2/0/163/Home.aspx>.

Water management has always played an important role in the economic and social life of Vietnamese people. Moreover, the economy of irrigated rice production, which emerged in the Red River Delta many centuries ago, constitutes an essential part of Vietnamese civilization and history. Practices, scales and responsibilities with regard to water management have however changed over time. Vast investment efforts have been made by the Vietnamese government during the past decade. The expansion and maintenance of hydraulic infrastructure is aimed to increasing of agricultural production, which is still a top priority of the central regime [4].

There are about 13 305 pumps on North of Viet Nam [30], many of them are old, work over limit and need replacements of devastated parts. Their efficiency is low due to the lack of care and maintenance. Since 2000 the situation is slightly improving. In the period from 2000 - 2010 the Vietnamese government invested about 2.8 billion USD into the preservation and construction of hydraulic infrastructure (including hydropower plants) and, according to the next 5 year plan, investment is expected even to grow. A large share of these funds is aimed into the hydraulic construction business. The business landscape in this field is composed of both state owned enterprises (focusing on the construction of large scale hydraulic schemes) and private companies. Due to market liberalization and privatization in the context of Vietnam's renovation policy, private businesses are increasingly benefiting from these huge investment funds [4].

By issuing decree 1402/BNN-TL the government of Vietnam started a new investment program for upgrading the pumping station infrastructure of the Mekong Delta. This program is a part of the government's new policy on integrated rural development (Tam Nong). Since 2009 to 2015 the Vietnamese government plans to invest about 133 million USD in both the conversion of petrol-run large and medium-sized pumping stations into electric-run pumping stations and the construction of new pumping stations throughout the delta. The program covers 3 129 pumping stations and aims at improving of irrigation and drainage capacity for 658 000 hectares of paddy land. The program will contribute to increasing the drainage capacity during the monsoon season (May to November), when the area is affected by rising water levels and seasonally occurring floods. On the opposite, it will ensure sufficient water supply for agriculture during the dry season, which lasts from December to April.

Figure1 Electric pumping station in Vinh Long Province (photo by S. Benedikter) [4]

In connection with agriculture and irrigation, mostly axial pumps are applied. Hand in hand with the industry development, centrifugal pump technology becomes of growing interest.

Centrifugal pump technology involves a board spectrum of flow phenomena which have a profound impact on design and operation through the achieved efficiency, the stability of the head-capacity characteristic, vibration, noise, component failure due to fatigue, as well as material damage caused by cavitation, hydro-abrasive wear or erosion corrosion. Operation and life cycle costs of pumping equipment depend to a large extent on how well these phenomena and the interaction of the pump with the system are understood.

The dissertation deals with the investigation of single-stage centrifugal pump designed at the Victor Kaplan Department of Fluid Engineering, Energy Institute, Technical University of Brno. Numerical modelling has been applied as a tool for the pump performance prediction. This may be important especially in cases when the pump specific speed is out of the common range and can help to investigate pump performance under various operational conditions.

2. State of the art

The story of pump development started since the Egyptians invented the “shadoof” (a simple device used to raise water from one level to another) in 2000 B.C. Principles of reciprocating pump and Archimedean screw pump were described around 200 B.C. The first pump that could be regarded as a centrifugal was a mud lifting machine which was built in 1475 by the Italian engineer Francesco di Giorgio Martini. This example led to further improvements in the construction and operation of pumps. The first really “centrifugal” pump was not developed until the late 17th century; it was designed by Denis Papin and had straight vanes. The curved vane was introduced by British inventor John Appold in 1851. At the same year, John Gwynne patented his centrifugal pump improvements. By 1959, all the major pump designs had been introduced and mostly developed into commercial products [40].

Since they serve diverse needs, pumps differ in types as well as in size. Pumps had a stage long-term development and are often designed by the hydraulic parameters. From these parameters, based on the empirical formulas and the basic relationships, the shape of the pump main hydraulic parts is calculated and designed.

Past 50 years have brought new trends in pump design, manufacturing, installation and operation. Design has progressed from slide rule and graph paper to experimental and numerical analysis using advanced methods of flow variables measurement and three-dimensional computer modelling. This has brought a new insight into the understanding of fluid flow and phenomena connected with energy transfer in a pump. To transfer a design concept to product can now be completed very quickly.

Machining has switched from multiple machine operations on hand operated lathes and milling machines to multipurpose machining centres. The accuracy increased and surface finish has improved. New materials were introduces like special steels, ceramics, teflon, plastics and others. New non-metals have made possible tiny pumps for human implant. Ceramics and tungsten/silicon carbide have vastly reduced wear rates in pumps of all sizes.

More care is now devoted to the pump installation and operation. Automatic control enables to keep the pump on its operating curve over its best efficiency range. This leads to improvement in pump life.

Increased environmental protection gave a real boost to pumps without shaft seals. Magnetic drive and canned motor units have thrived and even produced a hybrid combining the two technologies. Pump shaft sealing has also changed dramatically. Asbestos in packing is outlawed and today the vast majority of new pumps are supplied with mechanical seals, often in factory-assembled cartridge format to avoid the risk of face damage during handling [40].

There are many types of pumps that have been studied and developed, including centrifugal pumps. Yet there is not one pump ideally suited for every application, there are still many issues that need to be improved to enhance performance and specific parameters for each case. The design is not only focused on geometry and shape definition but also on optimisation of some design parameters to find the optimal operating point and investigate the *Q~H* (or *Q~Y*) curve stability. Flow field optimization by CFD methods enables significant improvements in both pump efficiency and suction performance.

Computational fluid dynamics (CFD) is equal partner with theoretical and experimental fluid dynamics in the analysis and solution of fluid dynamic problems. CFD synergistically complements the two approaches but can never replace them [3].

The end of the second millennium has brought enormous emphasis on computer applications in nearly all fields of engineering. Using CFD, it is possible to investigate the stationary and time dependent flow field in complex geometries. There are many commercial codes like FLOW-3D, FLOTRAN, STAR-CD, N3S, CFD-ACE, FLUENT, CFDS-FLOW3D, and NISA/3D-FLUID [3] that can be applied for this purpose. Nowadays, numerical simulation is often applied to replace physical prototypes. CFD enables to investigate the flow field in a pump in details and to propose improvements that can be further tested without building the prototype. The relatively low cost of this testing enables investigation of large number of impeller blade shape variations as well as casing shape optimization. Such research work can bring the improvement of the efficiency of existing pump design. Numerical modelling allows obtaining a wide variety of information, including not only velocities and pressure, but also the hydrodynamic forces generated due to the pump operation. Evaluation of pump loads can be helpful in case of bearings selection and proposal of axial thrust elimination.

These new trends have also reflection in Vietnam. The import of pumps from aboard prevails but there are also some domestically project as e.g. “Modelling tidal power turbines” [26]; or “Some research result about pump with small head” [30] focused on pump flow investigation and improvement. Some of the designers also use CFD software packages as Ansys or Fluent. The pictures bellow gives an example.

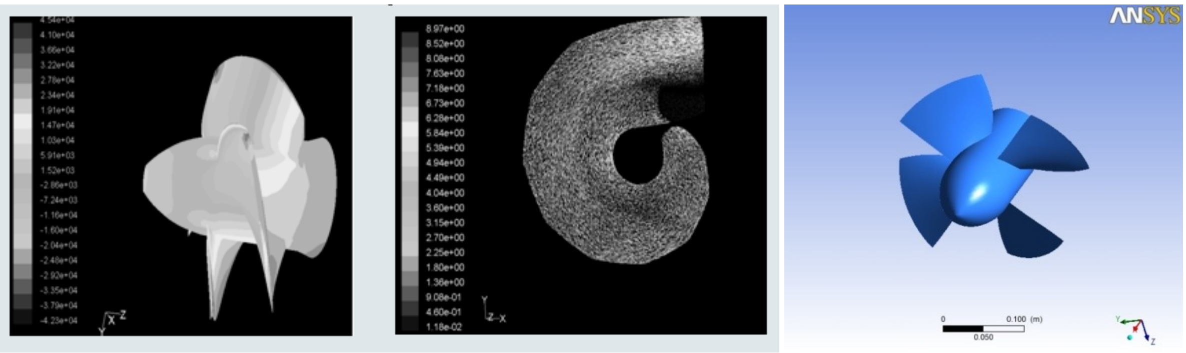

Figure 2 Some research of modelling application in Vietnam [26], [30].

Now, there are some institutes and companies applying numerical modelling in Vietnam as: Centre for Development and Application of Software for Industry (DASI Centre) with the web site <http://dasi.vn/index.php?lang=en>; or Advanced Technology Joint Stock Company with the web site <http://www.advantech.vn/index.php?lang=en>. But most of the research is carried out individually and in Vietnam there aren’t super computer systems for bigger research and more complex applications. Numerical modelling is not widely used as a tool and that is why my thesis and research is focused on application of CFD tools in pump performance investigation.

2.1. Classification of pumps

Pumps can be classified by the way they generate an energy which is added to a fluid. The most significant principle is the transfer of mechanical energy to hydraulic energy. In this field we can distinguish two main categories of pumps:

- positive displacement pumps
- centrifugal pumps (also called “rotor-dynamic pumps”)

Positive displacement pumps work on the principle of direct energy conversion. They deliver a definite volume of liquid with each piston stroke or shaft rotation with no delivery in between. Positive displacement pumps can be further divided into three groups: reciprocating pumps, rotary pumps and diaphragm pumps. Positive displacement pumps are used if the high pressure is required or the viscous fluid is delivered.

Centrifugal pumps deliver continuous flow for different pump operational conditions (i.e. pump speed and discharge resistance). According to the direction, in which the fluid passes through the pump impeller, we can distinguish the axial, mixed-flow, and radial types of impeller. Centrifugal pumps add kinetic energy to a fluid using a rotating impeller. Kinetic energy of the fluid is converted into pressure in the diffuser.

Many factors go into determining which type of pump is suitable for an application. Although many applications can be served by both positive displacement and centrifugal pumps, centrifugal pumps are more common because they are simple and safe to operate, require minimal maintenance, and have long operating lives.

2.2. Specific speed

Optimal use of the various pump types can be defined using the criteria of hydrodynamic similarity. The pump connections with hydraulic system can be defined by the flow rate (capacity) Q and the total head H. Also the dependence on the pump drive must be taken into account using the rotation speed n. These three parameters are included in a pump specific speed, which is an index number that relates to pump geometry and performance. Specific speed corresponds to pump flow characteristics, hydraulic efficiency, power consumption and its Net Positive Suction Head (NPSH). The first concepts of specific speed were formulated in 1937-1938. During the time it has become a useful tool for both pump designers and pump users.

There are different definitions of specific speed. As in all fluid mechanical formulations, one should first seek a non-dimensional parameter which distinguishes the nature of this task. In this case, derivation of specific speed there is based on similarity theory and accounts for the significant forces acting during the pump operation. For the operation of hydraulic machines pressure and pulse forces are very important which are respected in the Euler and Strouhal numbers [5]

$$Eu = \frac{\Delta p}{\rho \cdot c^2}\,,\ Sh = \frac{c}{n \cdot D} \tag{1}$$

This concept of specific speed, denoted by n_b, results in non-dimensional parametric group that is determined by dimensional analysis:

$$n_b = \frac{1}{Sh.Eu^{0.75}} = n \cdot \frac{Q_v^{0.5}}{Y^{0.75}} \tag{2}$$

where

n	rotational speed	[s^{-1}]
Q_v	flow rate	[$m^3.s^{-1}$]
Y	specific energy	[$J.kg^{-1}$]

Second concept of specific speed can be interpreted as follows: pump specific speed is the speed of an ideal pump geometrically similar to an actual pump, which when running at this speed would raise a unit of volume per unit of time, through a unit of head, as following:

$$n_q = n \cdot \frac{Q_v^{0.5}}{H^{0.75}} \quad [\mathrm{min}^{-1}] \tag{3}$$

where

n	rotational speed	[min^{-1}]
Q_v	flow rate	[$m^3.s^{-1}$]
H	head	[m]

Similarly, for unit performance (1 horsepower) and a unit of head the specific speed, denoted by n_s, specific speed is defined as follows:

$$n_s = 3.65 \cdot n \cdot \frac{Q_v^{0.5}}{H^{0.75}} \quad [\mathrm{min}^{-1}] \tag{4}$$

where

n	rotational speed	[min^{-1}]
Q_v	flow rate	[$m^3.s^{-1}$]
H	head	[m]

The importance of the pure number, with or without units, is that of a comparative tool. Lower numbers indicate a low specific speed; higher numbers, of course mean, high specific speed. Specific speed is used to classify pumps as to their type and the range of their application related to their efficiency, as depicted in Figure 3 [34].

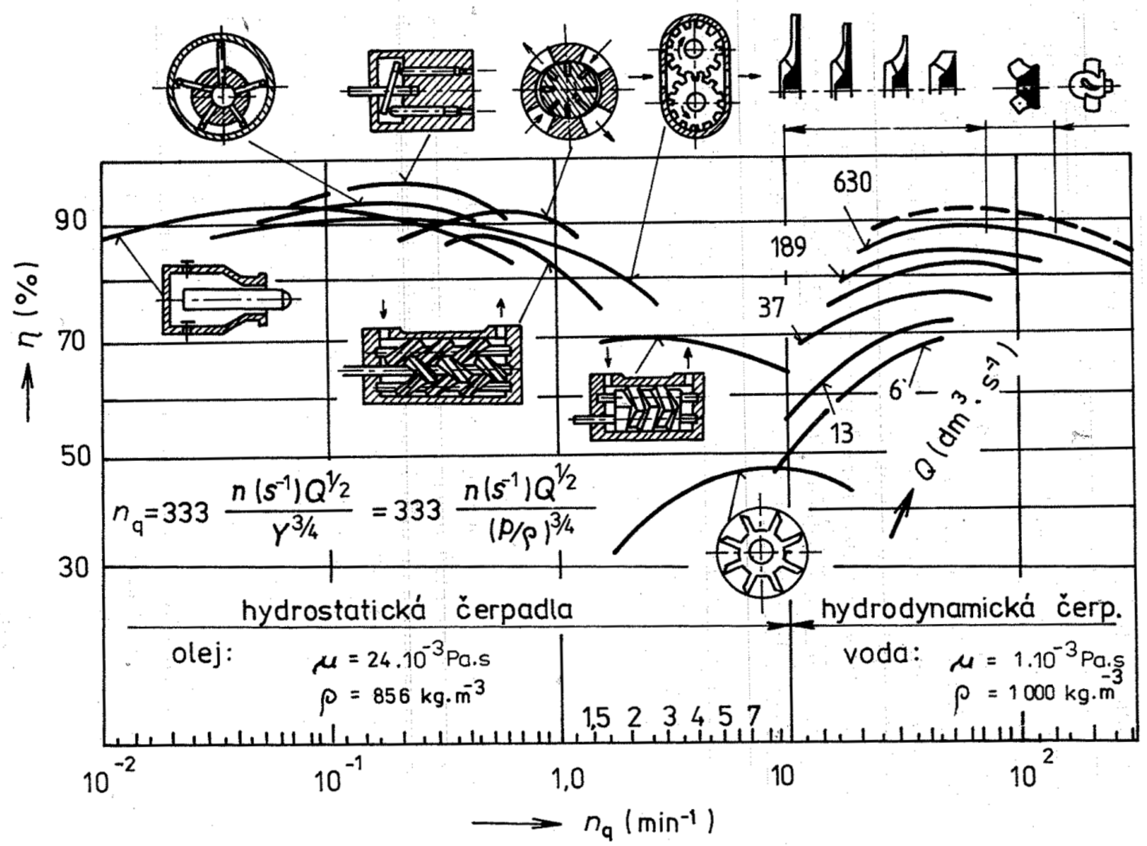

Figure 3 Summary of hydrostatic and hydrodynamic pump types with optimum range of n_q

Concerning hydrodynamic pumps, the specific speed determines the general shape of the impeller as can be seen in Figure 3 and Figure 4.

10 to 30	22 to 60	50 to 70	70 to 120	50 to 135	110 to 410
radial	**radial with wrapped blade**	**Francis**	**diagonal**	**diagonal propeller**	**axial propeller**
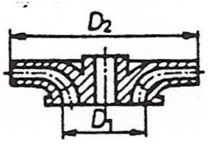	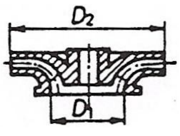	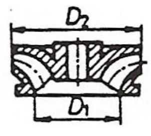	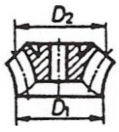	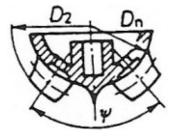	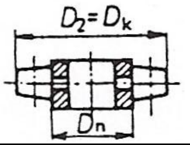

Figure 4 Shape of impeller [17], [34]

As the specific speed increases, the ratio of the impeller outlet diameter D_2, to the inlet or eye diameter D_1 decreases and it becomes 1.0 for the axial type of impeller. Radial impellers generally provide low flow rate and develop high head through centrifugal force. Mixed flow impellers, which are of higher specific speeds, develop head partly by centrifugal force and partly by axial force. Axial flow impellers generate their head through axial forces. They provide high flow rate and low head. "Specific speed" is referred to with many additional charts, curves, and technical plots.

2.3 Approaches to pump design

Design of the right pump for a certain application related to a specific industry and service requires an extensive knowledge of hydraulics. General pump design should respect several basic requirements that are essentially common to all impellers and diffusing parts regardless of the specific type:

- **Stability curve:** This is description for pump's operating, the steadily decreasing head with increasing flow rate is mostly desired, with maximum head at $Q = 0$.
- **Efficiency:** This leads to cheaper cost.
- **Good performance:** Easier for operate this pump.
- **Cavitations' resistance:** This leads to long-time pump's life.

The main task of pump design includes the calculation of main impeller dimensions, drawing median line along pump blade. Then the shape and inlet and outlet angle of the blade is defined. To ensure the required parameters, also number of blades must be specified. Besides the impeller, also the geometry and shape of the cross-section of volute must be designed. Different methods can be applied based on:

- One-dimensional flow
- Two-dimensional flow
- Three-dimensional flow

2.3.1. One-dimensional method

This method is based on the assumption of one-dimensional flow through the impeller and volute. It means that all variables change along the middle streamline of the blade. This approach corresponds to kinematic relationships described with velocity triangles in the impeller.

When the liquid enters a pump and comes in contact with the rotating element, it becomes necessary to deal with both the absolute as well as the relative velocities of flow. The absolute velocity of a body is velocity related to the earth. The absolute velocity is the vector sum of relative velocity (fluid pointed to the impeller) and the peripheral velocity of the impeller [5], [39].

Relation to theoretical specific energy of an infinite number of pump impeller blades can be expressed by the following [5]:

$$Y_{\infty} = \frac{p_2 - p_1}{\rho} + \frac{c_2^2 - c_1^2}{2} = \frac{u_2^2 - u_1^2}{2} + \frac{w_1^2 - w_2^2}{2} + \frac{c_2^2 - c_1^2}{2} = \frac{c_2^2 + u_2^2 - w_2^2}{2} + \frac{c_1^2 + u_1^2 - w_1^2}{2} \quad (5)$$

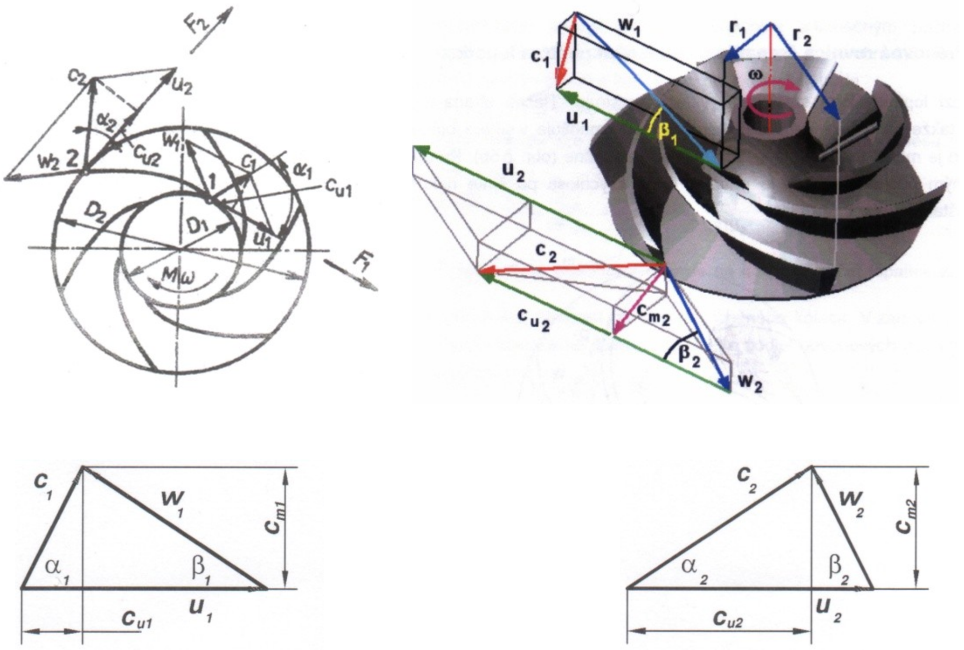

input (subscript 1) output (subscript 2)

Figure 5 Velocity triangles in the impeller at inlet and outlet [5], [15]

where

$\boldsymbol{c}$ is absolute velocity vector

$\boldsymbol{w}$ is relative velocity vector

$\boldsymbol{u}$ is peripheral velocity vector

By law of cosines for velocity triangle

$$w_1^2 = c_1^2 + u_1^2 - 2c_1 u_1 \cos\alpha_1 \tag{6}$$

$$w_2^2 = c_2^2 + u_2^2 - 2c_2 u_2 \cos\alpha_2 \tag{7}$$

put

$$c_{u1} = c_1 \cos\alpha_1 \tag{8}$$

and

$$c_{u2} = c_2 \cos\alpha_2 \tag{9}$$

Subtracting (6) and (7) from (5) we get Euler pump equation:

$$Y_\infty = u_2 c_{u2} - u_1 c_{u1} \tag{10}$$

where

Y_∞ is the theoretical specific energy in (for ideal flow and ideal angle of attack, infinite number of blades).

This equation and pump affinity laws are useful for pump design and experimental investigation. But this method has also many restrictions because it considers only one-dimensional flow.

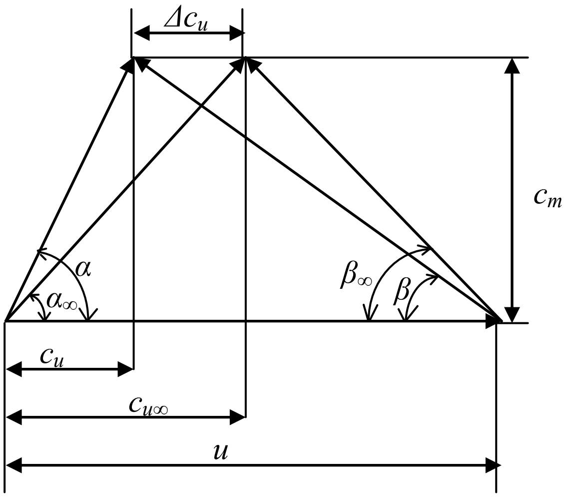

Figure 6 Velocity triangles for ideal and real flow

For the real flow (finite number of blades z) the velocity component c_u decreases in comparison with ideal flow (subscript ∞) and thus we can observe the difference Δc_u as shown in Figure 6.

In this case the specific energy is defined as follows:

$$Y_z = u_2(c_{u2} - \Delta c_u) - u_1 c_{u1} \tag{11}$$

We must account for decreasing of centrifugal pump output. The corrections applied on specific energy were defined by many authors and can be found in literature [15] (e.g. Stodola, Busemann, NEL, Waisser, Pfleiderer and others). The design of meridional cut of blade is then followed by the design of blade shape including the blade angles β_1 and β_2.

The design is based on given quantities: n, Q_{opt}, H_{opt} and the boundary conditions. Based on these parameters, the specific speed n_{b} (n_{s}, n_{q}) is calculated. Additionally, the approach flow conditions must be defined. In many applications the approach flow angle is α_1 = 90°, and the distribution of the meridional velocity c_{m} over the approach flow cross section is assumed constant.

With the help of the “1D” design, fundamental impeller geometry can be determined for prescribed mass flow rate and head. Calculation of the main dimensions and blade angles by one-dimensional methods is based on empirical correlations for slip factors and hydraulic efficiencies that are based on databases and experience. Verification and further optimization of the designed geometry can be done by CFD using the 3D Navier-Stokes equations.

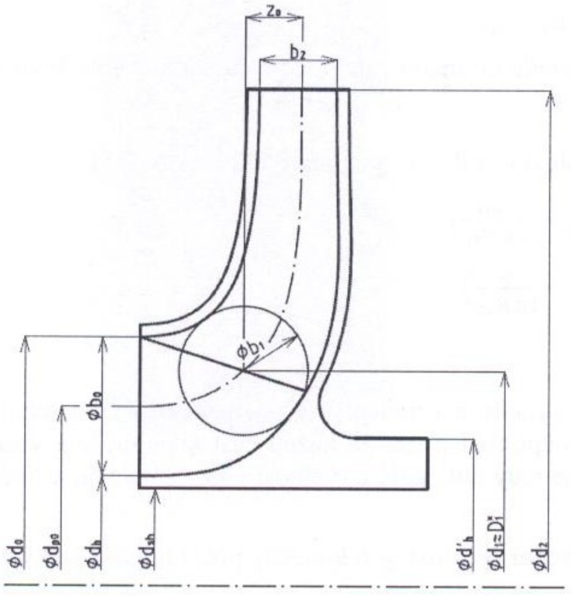

Figure 7 Meridional geometry of the blade [33]

where

d_0	is eye diameter
d_{p0}	is impeller’s diameter at eye axis
d_h	is inside diameter at impeller’s hub
d_{sh}	is shaft’s diameter
d'_h	is outside diameter at impeller’s hub
$d_1 = D^*_1$	is impeller inlet diameter
d_2	is impeller outlet diameter
b_0	is eye width
b_1	is impeller inlet width
b_2	is impeller outlet width
Z_o	is distance from inlet centre to outlet centre of impeller

Similar approach can be applied on volute (spiral) design. The object of the volute is to convert the kinetic energy generated by the impeller into pressure. The pump casing has no part in the generation of the total head and therefore the main purpose is to minimize losses.

There are two basic approaches by which we can define the flow in the volute:

1. The mean speed through all cross-sections of volute is assumed constant

$$c_{mean} = c_4 = konst \qquad (12)$$

2. The vorticity in the volute is assumed constant

$r \cdot c_u = konst$, where $\dfrac{dQ_\alpha}{dS_\alpha} = c_u$ and α is an orientation angle

The first method is applied most often especially for smaller size of volutes. Single-volute design based on constant velocity is more efficient than those using more complicated volute designs. They are also less difficult to cast and more economical to produce because of the open areas around impeller periphery. Theoretically they can be used on large as well as small pumps of all specific speeds. Stepanoff gives a complete description of single-volute casing design. The velocity is calculated from

$$c_4 = K_4\sqrt{2Y_1} \tag{13}$$

where K_4 is coefficient was predicted from [28].

The area of cross-sections is growing linearly from the volute tongue (S_1) to the cross-section S_8 (see Figure 8).

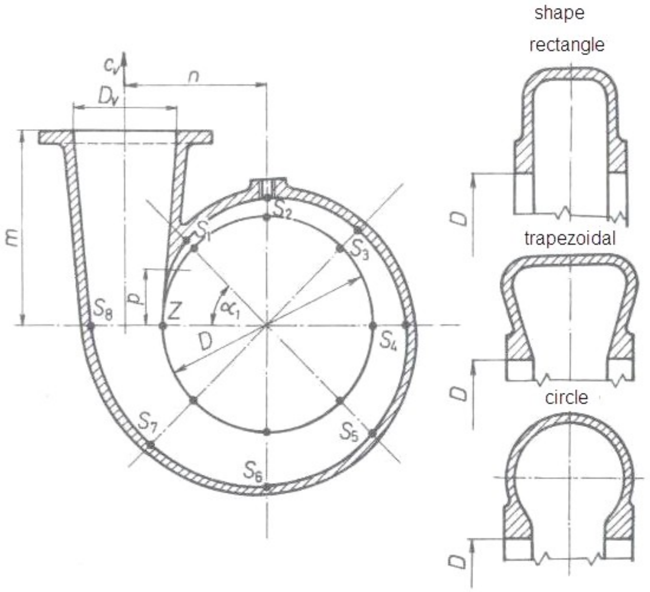

Figure 8 Scheme of volute with various shape of cross-section [5]

Based on the assumption of constant velocity c_4, the areas are calculated from:

$$\left.\begin{aligned} S_n &= \frac{n}{n}.\frac{Q}{c_4} \\ S_{n-1} &= \frac{n-1}{n}.\frac{Q}{c_4} \\ S_{n-2} &= \frac{n-2}{n}.\frac{Q}{c_4} \\ &\vdots \\ S_1 &= \frac{1}{n}.\frac{Q}{c_4} \end{aligned}\right\} \tag{14}$$

The application of the 1D method of pump design is presented on Appendix 13.3.

2.3.2. Two-dimensional method

Assumption of potential flow and orthogonal grid for one medial section of blade is applied in this case. The main difference in comparison with one-dimensional approach is that we can account for meridional velocity variation along the lines perpendicular to the streamlines [29].

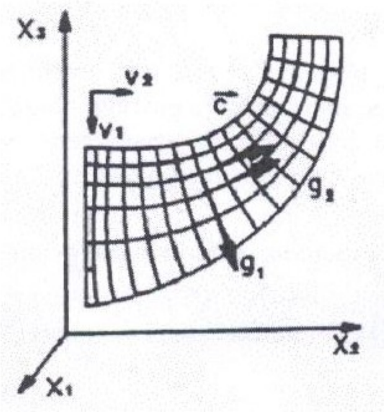

Figure 9 Orthogonal grid in impeller section [2]

This method will not be applied in my research work, as it also brings many restrictions and limiting assumptions, as it does not account for viscosity of the fluid. The main objective of my work is to model complex 3D viscous fluid flow, which enables to predict the fluid flow in details.

2.3.3. Three-dimensional method 3D

This method is based on numerical solution of basic equations describing the flow of fluid, which express basic conservation of mass, momentum, and energy in volume element.

The equation of continuity in case of incompressible flow [20]:

$$\frac{\partial u_j}{\partial x_j} = 0 \qquad (15)$$

Navier-Stokes equation [20]:

$$\underbrace{\frac{\partial u_i}{\partial t}}_{I} + \underbrace{\frac{\partial u_i u_j}{\partial t}}_{II} = \underbrace{-\frac{1}{\rho}\frac{\partial p}{\partial x_j}}_{III} + \nu \underbrace{\frac{\partial^2 u_i}{\partial x_j^2}}_{IV} + f_i \qquad (16)$$

where

$u_{i,j}$	components of velocity vector (*i, j* are couple of *x, y* or *z*)
p	static pressure
ρ	density of fluid
ν	kinematic viscosity
f_i	signs components of external volume forces
I	Transient Term
II	Convection Term
III	Diffusion Term
IV	Source Term

These equations are discretized on volume elements which lead to a system of equations that are solved by numerical methods using boundary condition and initial conditions for the problem. These tasks need computer's aid to create grid and carry out the calculations.

For the 3D method, tetrahedral and hexahedral elements can be applied, as is shown of the Figure 10.

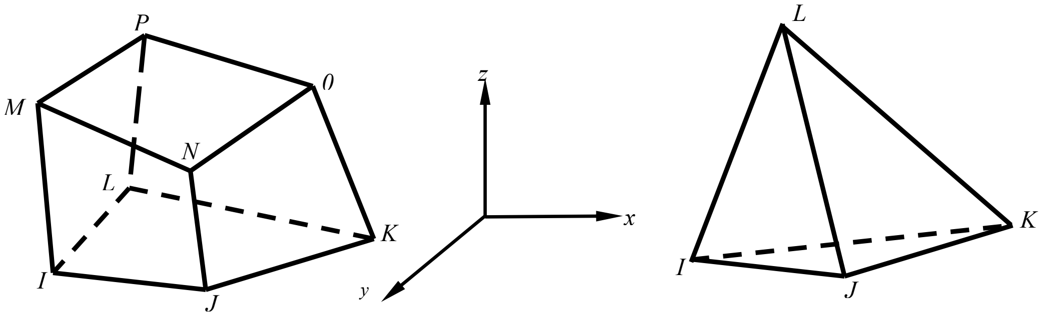

Volume element 3D - 8 nodes

Volume element 3D – 4 nodes

Figure 10 Volume element for calculation [25]

Nowadays, with aid from computer, we can design a very fine grid and to obtain detailed solution of the problem. This method is advantageous and can show any value at any section, also calculate integral value and differential value.

2.4. Modelling of Turbulence

Mathematic models of fluid flow can be applied for two basic fluid flow regimes:

- Laminar flow
- Turbulent flow

Most of the problems of the fluid flow modelling are connected with the modelling of turbulence. Turbulent flows are characterized by fluctuating velocity and pressure fields. These fluctuations mix transported quantities, such as mass, momentum, and cause the transported quantities to fluctuate as well. Since these fluctuations can be of small scales and high frequency, they are computationally too expensive to be simulated directly in practical engineering calculations. Instead, the governing equations can be treated in several ways: time-averaged, ensemble-averaged, or otherwise manipulated to remove the small scales. As a result of this procedure a modified set of equations is obtained that is computationally less demanding to solve. However, the modified equations contain additional unknown variables, and turbulence models are applied to determine these variables in terms of known quantities.

For the purpose of turbulence modelling several approaches can be used. We can distinguish three main methods: DNS, LES or RAM (RANS) model:

+ **DNS-Direct numerical simulation:** In this approach all scales of turbulent eddies are solved using exact Navier-Stokes equations. The grid number required is proportional to the nine-fourth power of the flow Reynolds number, which is unlikely to reach.

+ **LES-Large eddy simulation:** provides an alternative approach in which the large eddies are computed in a time-dependent simulation that uses a set of “filtered” equations. By filtering eddies that are smaller than the mesh size are removed and are modelled by sub-grid models.

+ **RAM** (**RANS**) **- Reynolds-averaged Navier-Stokes equations:** represent the transport equations for the mean flow quantities only, with all the scales of the turbulence being modelled. This greatly reduces the computational effort. This approach is generally adopted for practical engineering calculations. The most popular are two-equation models in which the transport equation is defined for the velocity and length scales of turbulence: standard k-ε, RNG k-ε or k-ω SST.

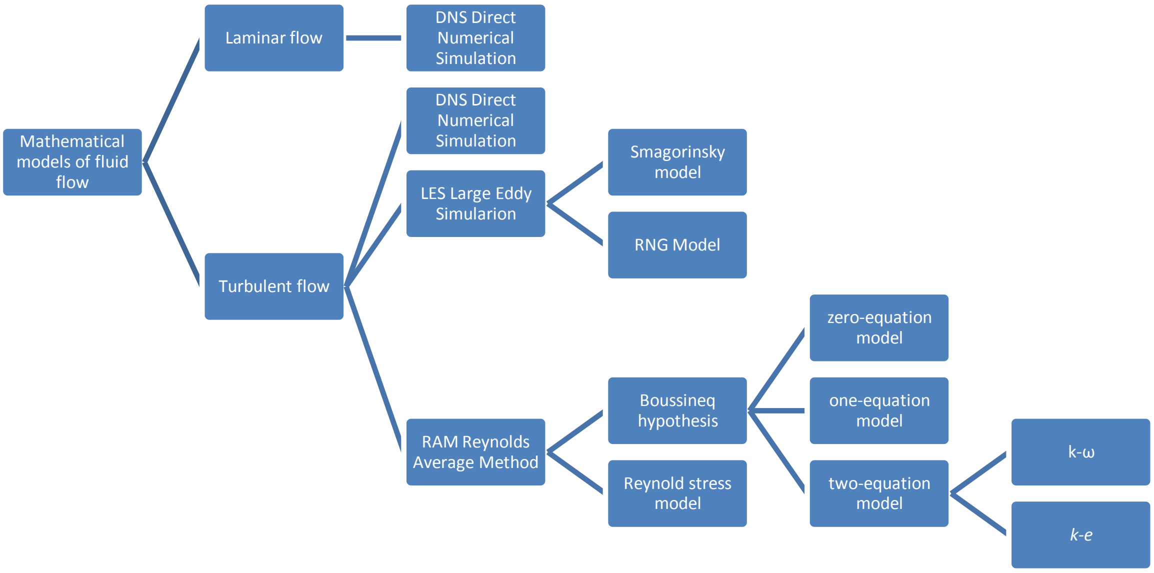

Figure 11 Mathematical models of fluid flow [20]

It is an unfortunate fact that no single turbulence model is universally accepted as being appropriate for all classes of fluid flow problems. The choice of turbulence model depends on many considerations such as the physical phenomena governing the flow, the established practice for a solution of specific class of problem, the required level of accuracy, the available computational resources, and the amount of time available for the simulation. To make the most appropriate choice of the model for certain application, it is necessary to understand the capabilities and limitations of the various models [10], [12].

Pump flow belongs to the most complex cases of internal flows. The geometry contains stationary and rotating parts, curved passages and narrow gaps through sealing rings. The flow is originally three- dimensional, with low turbulence and high turbulence regions, separation, boundary layers. As a result of this complexity of the flow, there are no clear recommendations on the most suitable turbulence model to be used. Various turbulence modelling options have been developed and improved to remove a specific weakness of the standard k-ε model in complex flows similar to those of a pump flow. Some of the recent models have proven to be universally better than the standard k-ε model. The RNG k-ε model is known to be better at predicting flow with complex strain fields and recirculation. Flow separation from surfaces under adverse pressure gradients is more accurately predicted with the SST (shear stress transport) version of the blend between *k*-ω at the wall and *k*-ε away from the wall developed by Menter (1996) [12].

In this work these models were used:

- Standard *k*-*ε* model
- Renormalization-group (RNG) *k*-*ε* model
- Shear-stress transport (SST) *k*-*ω* model

In the following chapter the RNG *k*-*ε* model and the shear-stress transport (SST) *k*-ω model that were applied for the modelling of turbulent flow in a pump are described.

2.4.1. RNG *k-ε* model

The RNG *k*-*ε* model was derived using a rigorous statistical technique (called renormalization group theory). It is similar in form to the standard *k*-*ε* model, but includes the following refinements:

- The RNG model has an additional term in its *ε* transport equation that significantly improves the accuracy for rapidly strained flows.
- The effect of swirl on turbulence is included in the RNG model, enhancing accuracy for swirling flows.
- The RNG theory provides an analytical formula for turbulent Prandtl numbers, while the standard *k*-*ε* model uses user-specified, constant values.
- While the standard *k*-*ε* model is a high-Reynolds-number model, the RNG theory provides an analytically-derived differential formula for effective viscosity that accounts for low-Reynolds-number effects. Effective use of this feature does, however, depend on an appropriate treatment of the near-wall region.

These features make the RNG *k*-*ε* model more accurate and reliable for a wider class of flows than the standard *k*-*ε* model.

The RNG based *k*-*ε* turbulence model is derived from the instantaneous Navier-Stokes equations, using a mathematical technique called “renormalization group” (RNG) methods. The analytical derivation results in a model with constants different from those in the standard *k*-*ε* model, and additional terms and functions in the transport equations for *k* and *ε*. A more comprehensive description of RNG theory and its application to turbulence can be found in [12].

The RNG *k*-*ε* model has a similar form to the standard *k*-*ε* model:

- Continuity equation

$$\frac{\partial \overline{u}_j}{\partial x_j} = 0 \tag{17}$$

- Reynolds averaged equation

$$\frac{\partial \bar{u}_i}{\partial t}+\frac{\partial \bar{u}_i \bar{u}_j}{\partial x_j}=-\frac{1}{\rho}\frac{\partial \bar{p}}{\partial x_i}+\nu\frac{\partial^2 \bar{u}_i}{\partial x_j^2}+f_i-\frac{\partial\left(\overline{u'_i u'_j}\right)}{\partial x_j} \tag{18}$$

where from Boussinesq hypothesis

$$-\overline{u'_i u'_j}=\nu_t\left(\frac{\partial \bar{u}_i}{\partial x_j}+\frac{\partial \bar{u}_j}{\partial x_i}\right)-\frac{2}{3}k\delta_{ij} \tag{19}$$

- Transport equation for turbulence kinetic energy

$$\frac{\partial k}{\partial t}+\frac{\partial \bar{u}_j k}{\partial x_j}=\frac{\partial}{\partial x_j}\left(\frac{\nu_t}{\sigma_k}.\frac{\partial k}{\partial x_j}\right)+\underbrace{\nu_t\left(\frac{\partial \bar{u}_j}{\partial x_i}+\frac{\partial \bar{u}_i}{\partial x_j}\right)\frac{\partial \bar{u}_i}{\partial x_j}}_{P}-\underbrace{C_D\frac{k^{3/2}}{l}}_{\varepsilon} \tag{20}$$

where

P	production of turbulent kinetic engergy
ε	viscous dissipation rate

- Transport equation for dissipation rate

$$\frac{\partial \varepsilon}{\partial t}+\frac{\partial \bar{u}_j \varepsilon}{\partial x_j}=\frac{\partial}{\partial x_j}\left(\frac{\nu_t}{\sigma_\varepsilon}.\frac{\partial \varepsilon}{\partial x_j}\right)+C_{1\varepsilon}\nu_t\left(\frac{\partial \bar{u}_j}{\partial x_i}+\frac{\partial \bar{u}_i}{\partial x_j}\right)\frac{\partial \bar{u}_i}{\partial x_j}-C_{2\varepsilon}\frac{\varepsilon^2}{k} \tag{21}$$

2.4.2. SST *k-ω* model

The shear-stress transport (SST) k-ω model was developed by Menter [12]. In this model the equation for transport of kinetic turbulent energy *k* and specific dissipation rate ω are defined. The main objective is to effectively blend the robust and accurate formulation of the k-ω model in the near-wall region with the free-stream independence of the k-ω model in the far field. To achieve this, the k-ε model is converted into a k-ω formulation. Besides the standard k-ω model, the SST k-ω model was developed, which is similar to the standard k-ω model, but includes the following refinements:

The standard k-ω model and the transformed k-ω model are both multiplied by a blending function and both models are added together. The blending function is designed to be one in the near-wall region, which activates the standard k-ω model, and zero away from the surface, which activates the transformed k-ω model.

The SST model incorporates a damped cross-diffusion derivative term in the ω equation. The definition of the turbulent viscosity is modified to account for the transport of the turbulent shear stress. The modelling constants are different.

These features make the SST k-ω model more accurate and reliable for a wider class of flows (e.g., adverse pressure gradient flows, airfoils, transonic shock waves) than the standard model.

The SST k-ω model has a similar form to the standard k-ω model:

$$\frac{\partial}{\partial t}(\rho k)+\frac{\partial}{\partial x_i}\left(\rho k \overline{u_i}\right)=\frac{\partial}{\partial x_i}\left(\Gamma_k \frac{\partial k}{\partial x_j}\right)+G_k-Y_k+S_k \tag{22}$$

and

$$\frac{\partial}{\partial t}(\rho \omega)+\frac{\partial}{\partial x_i}\left(\rho \omega \overline{u_i}\right)=\frac{\partial}{\partial x_i}\left(\Gamma_\omega \frac{\partial \varepsilon}{\partial x_j}\right)+G_\omega-Y_\omega+D_\omega+S_\omega \tag{23}$$

where

G_k	the generation of turbulence kinetic energy due to mean velocity gradients
G_ω	the generation of ω
Γ_k	the effective diffusivity of k
Γ_ω	the effective diffusivity of ω
Y_k	the dissipation of k
Y_ω	the dissipation of ω
D_ω	the cross-diffusion term
S_k, S_ω	user-defined source terms

3. The main objectives of the thesis

Pump‘s characteristic curves describe the variation of head, power consumption, efficiency and NPSH on the flow rate. They are obtained by measurement and provided by pump producers. During the process of pump design, numerical modelling can be applied as a tool for the pump performance prediction. This may be important especially in cases when the pump specific speed is out of the common range and can help to investigate pump performance under various operational conditions. In addition, it is required to optimize the pump not only for the best efficiency point, but to investigate the entire operating range of $Q = 0$ to Q_{max} considered in the design.

The main objective of the doctoral thesis was to determine pump performance characteristics using numerical modelling of the three-dimensional viscous fluid flow.

The attention was focused on:

- evaluation of different approaches to rotor-stator interaction modelling
- evaluation of the influence of computational grid quality
- determination of Q~H curve and its stability
- determination of Q~η curve
- prediction of the radial force in centrifugal pump
- prediction of the axial force in centrifugal pump
- comparison of experimental results with the results obtained with numerical simulation
- application of various methods of post processing (concerning efficiency)
- investigation of the mathematical model's restrictions.

As a tool for numerical modelling, Fluent software package has been applied. The numerical investigation was done on the pump designed at the Victor Kaplan Department of Fluid Engineering, Energy Institute, Technical University Brno.

For comparison and verification of calculated data the measured performance curves of the given pump and statistical data collected from proven similar hydraulics were used.

4. Numerical Modelling of the Pump Flow

Two-dimensional model does not correspond to reality and that is why complex three-dimensional problem must be modelled. For the numerical modelling CFD code FLUENT Release 6.3 was applied. The incompressible, unsteady (and steady to compare) flow was modelled in 3D geometry. The RANS (RNG *k-ε* model and *k-ω SST* model) have been applied to a strongly unsteady flow.

Conservation equation of mass and momentum is defined in general conservative form for incompressible flow:

$$\frac{\partial(\zeta)}{\partial t} = -\frac{\partial}{\partial x_j}\left(u_j \zeta\right) + \frac{\partial}{\partial x_j}\left[\alpha_\zeta \frac{\partial \zeta}{\partial x_j}\right] + S_\zeta \tag{24}$$

where

t	time
x_j	coordinates
ζ	the variable of interest (swirl function, temperature, additives, or any scalar variable)
α_ζ	is the diffusivity (also called diffusion coefficient)
u_j	component of the velocity vector
S_ζ	describes "sources" or "sinks" of the quantity ζ

and terms on the right hand side are gradually convective, diffusion, and the source term. If ζ is a scalar quantity, then it is a linear equation of second order, if it is a component of velocity, this equation can be regarded as second-order non-linear equations. If diffusion member is outweigh, this problem is an elliptical equation or parabolic equations and leads to adjective transport, or hyperbolic equation leading to pressure changes.

The procedure of numerical solution includes following steps:

+ Create the model geometry and grid
+ Start the appropriate solver for 3D modelling
+ Import the grid into Fluent
+ Check the grid
+ Select the solver formulation (unsteady, 1st Order Implicit)
+ Choose the basic equations to be solved: turbulent model
+ Specify material properties
+ Specify the boundary conditions
+ Adjust the solution control parameters
+ Initialize the flow field
+ Calculate a solution
+ Examine the results
+ Analyse the results and compare with measure

4.1. Definition of problem

Geometry of the impeller and volute (resources) was defined according to design prepared in VUT Brno, see Figure 12.

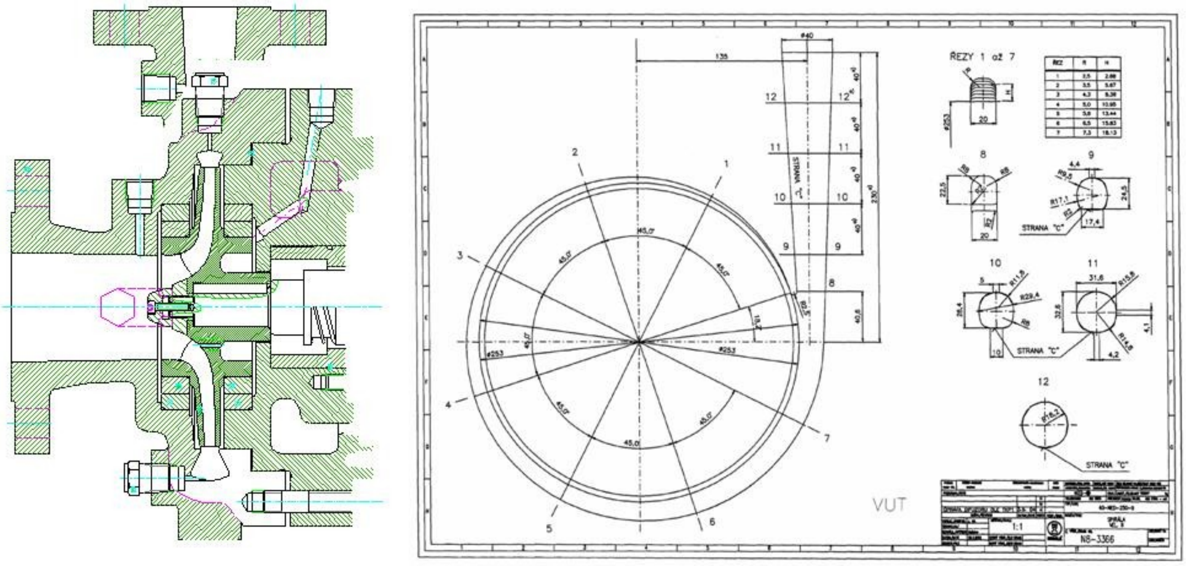

Figure 12 Geometry of the Impeller and Volute (from VUT-Brno)

Basic pump parameters:

Discharge	$Q = 7\ \mathrm{dm^3.s^{-1}} = 0.007\ \mathrm{m^3.s^{-1}}$
Head	$H = 80\ \mathrm{m}$
Speed	$n = 2\,900\ \mathrm{min^{-1}}$
Density	$\rho = 1\,000\ \mathrm{kg.m^{-3}}$

As can be seen from design parameters, the pump provides high head and low flow rate, which yields a low value of non-dimensional specific speed

$$n_{\mathrm{b}} = n\frac{Q_V^{\ 0.5}}{Y^{0.75}} = \frac{2900}{60}\cdot\frac{0.007^{0.5}}{(80.9\cdot 9.81)^{0.75}} = 0.0263 \qquad (25)$$

where:

n_b	specific speed	[1]
n	rotational speed	[s^{-1}]
Q_V	flow rate	[$m^3 \cdot s^{-1}$]
Y	specific energy	[$J \cdot kg^{-1}$]

The obtained value of specific speed ($n_{\mathrm{q}} = 9.08\,\mathrm{min}^{-1}$) is very low. It is caused by the high values of the head in connection with the low values of the flow rate. Such parameters can be reached by twisting the blades of the impeller.

The prediction of pump parameters by empirical formulas in this case often fails, as the specific speed is below the specific speed range considered for the radial type of impeller. Numerical modelling can be helpful tool in this pump flow investigation.

At the beginning of the numerical modelling 3D geometric model of the pump components must be created which describes the calculation domain by coordinates. This calculation domain is then subdivided into a large number of cells, i.e. a grid is generated, the quality of which is essential for the reliable numerical solution. Large number of cells brings better accuracy but also higher demands on computational time.

Impeller and the volute were modelled together to account for their interaction and resulting dynamic effects.

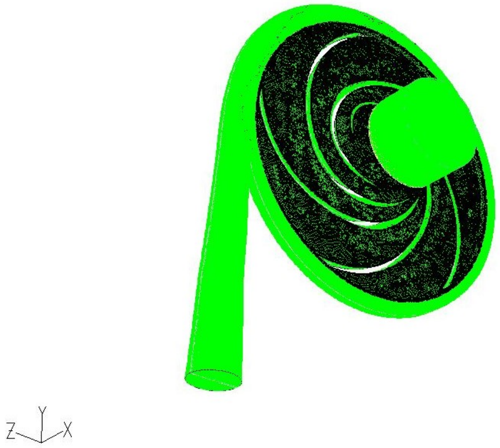

Figure 13 Schematic of the numerical experiment

A computational grid was prepared in Gambit respecting the designed dimensions and shape of impeller and volute. Two different grids were prepared, one consisting of 233 259 cells and the second one with refined boundary layer with 802 555 cells. The grid of inlet (suction pipe), impeller and diffuser (spiral) were connected through interfaces. The detail of the grid for both conformal and non-conformal mesh can be seen on Figure 14. After grid adaption in FLUENT code, the final grid consisted of 1 028 416 cells.

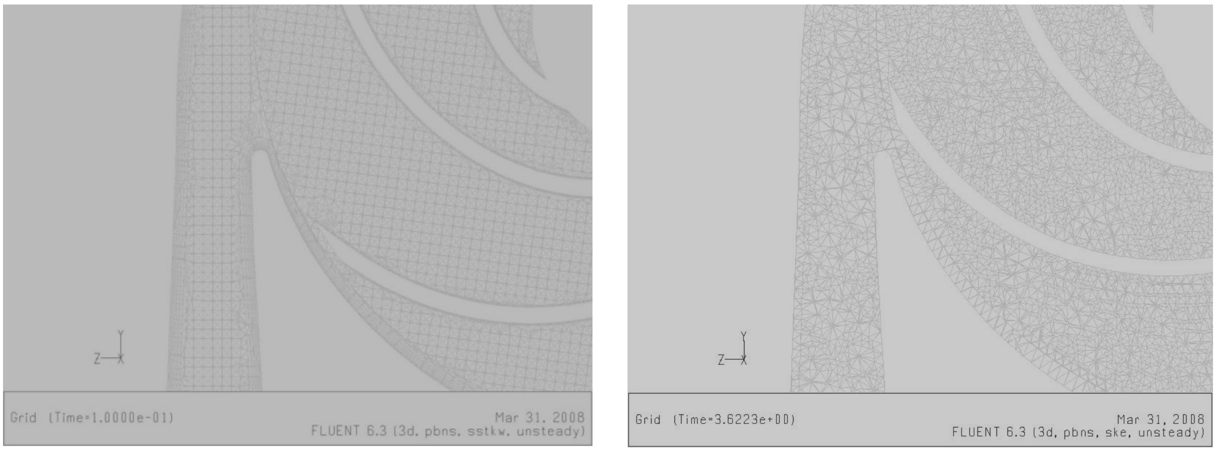

Grid non-conformal 233 259 cells

Grid for conformal 802 555 cells

Figure 14 Cross section of geometry

With the conformal grid, the cells on the interfaces between inlet and impeller, impeller and diffuser have similar size and shape. This preserves many quantities in the calculating.

Boundary conditions were set according to the physical experiment:

- inlet: mass flow rate
- outlet: outflow condition

The relative flow rate has been changed from 0.014 to 2 (multiple of optimal flow rate). The computational parameters leading to the most reasonable result were as follows:

- pressure based solver, 3D, non-stationary, isothermal, turbulent flow.
- *k-ω* SST (2 equations).
- unsteady formulation: 1st Order Implicit.
- time step: 0.0001 [s], max. number of iterations per time step 20.

All the unsteady simulations had to be run for long time. However the calculations were run for a long period, the calculated flow time in all tested did not exceed 0.3 [s], which means that it is difficult to compare the statistical data with experimental measurement, hence we compared data in these cases together (*k-ε* or *k-ω*, time depend or steady, non-conformal or conformal grid). The first part of numerical modelling was focused on testing selected turbulence models and approaches to rotor modelling.

4.2. Approaches to rotor modelling

The problem involves multiple moving parts as well as stationary surfaces which are not surfaces of revolution. Zones which contain the moving components can then be solved using the moving reference frame equations, whereas stationary zones can be solved with the stationary frame equations. In Fluent, two approaches can be applied for the modelling of such cases [12]:

- Moving Reference Frame model (MRF)
- Moving Mesh Model (SMM)

Moving Reference Frame model approach is steady-state approximation and differs primarily in the manner in which conditions at the interfaces are treated. In this case unsteady problem is transferred to the role of stationary due to the rotating coordinate system. Acceleration of the liquid is incorporated into the model as a new element in the motion equation. This case doesn’t solve the interaction between stator and rotor.

The sliding mesh model (SMM approach) is unsteady due to the motion of the mesh with time. During the calculation of the impeller rotates and stator has relative implement to the grid. It allows the calculation of unsteady flow. This model is demanding in calculation time.

This approach was applied in most cases. Data Sampling for Time Statistics was applied which enable to compute the time average (mean) of the instantaneous values and root-mean-squares of the fluctuating values sampled during the calculation.

Both approaches have been tested on the course grid as well as fine grid. The objective of this testing was to evaluate the performance of different methods and make a choice of grid and rotor-stator modelling in the detailed study.

4.3. Calculation on non-conformal mesh

The first calculations were carried out on the course grid consisting of 233 259 cells with equal distribution. The standard *k-ε* model was applied with standard wall function. The simulation was carried for the non-dimensional flow rates ranging from 0.07 to 1. *Q~H* curve was investigated.

Two approaches to rotor modelling were tested: Moving Reference Frame (MRF) and Moving Mesh (SMM).

The moving mesh was applied for unsteady case. The pressure at output of diffuser (volute) exhibits large differences. Max value, min value, and average value was evaluated (see Figure 15 below). These values have been recorded on time dependency and selected for one shaft revolution. The max value is maximum value of all recorded values. The min value is also minimum value of all recorded values. The average value is a mean value of that.

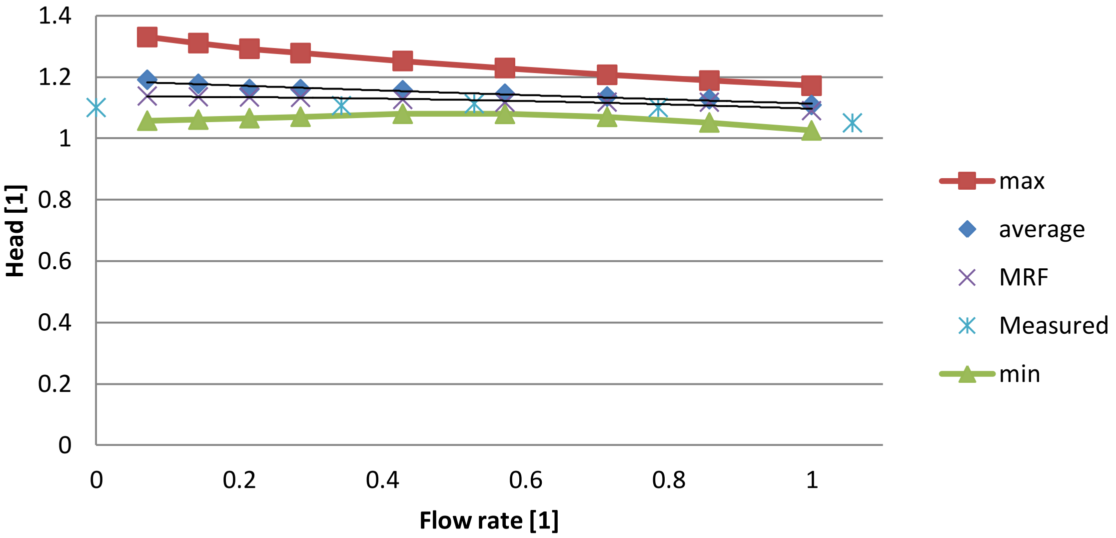

Figure 15 Head at Outlet of Diffuser – case MRF and case SMM – non-conformal mesh

max	stands for max value of Moving Mesh
average	stands for average value of Moving Mesh
MRF	stands for value of Moving Reference Frame
Measured	stands for value of measurement from Sigma Lutín Group
min	stands for min value of Moving Mesh

It can be seen, that the variation of head with flow rate corresponds to measurement in case of both approaches. The head is decreasing with growing flow rate. The *Q~H* curve of Moving Mesh exhibits slightly higher values (2÷5%) of head than MRF's and the difference is growing with decreasing flow rate.

4.4. Calculation with conformal mesh

This mesh has more cells near the boundary and the cells are smaller than in case non-conformal mesh.

- Design model with 802 555 cells.
- Standard *k*-*ε* model was applied with standard wall function

Two approaches to rotor modelling were tested: Moving Reference Frame and Moving Mesh.

With more cells near boundary, the calculation runs slowly but the results aren't better than cases with non-conformal mesh.

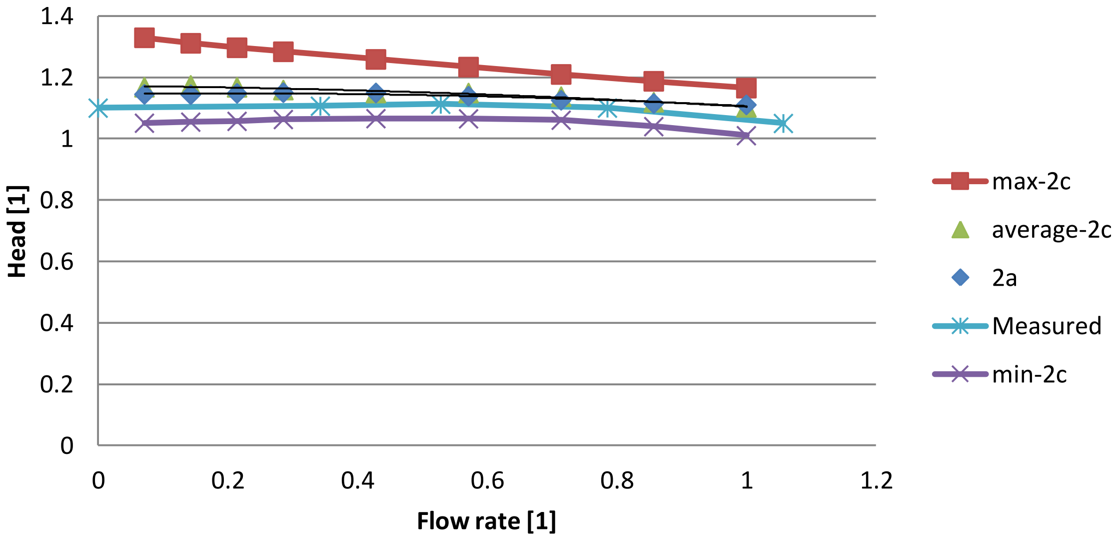

Figure 16 Head at Outlet of Diffuser – case MRF and SMM – conformal mesh

max-2c	stands for max value of Moving Mesh
average-2c	stands for average value of Moving Mesh
2a	stands for moving reference frame
Measured	stands for value of measurement from Sigma Lutín Group.
min-2c	stands for min value of Moving Mesh

As in previous case, the head predicted with Moving Mesh is slightly higher than values obtained with MRF's and the difference is growing with decreasing flow rate. In unsteady cases, the most problems arise in case of small values of flow rate. The calculation for low values of the flow rate is connected with lower accuracy and so it is difficult to confirm the stability of the *Q~H* curve. The difference of predicted values and measured values reach to 5%.

4.5. Moving Mesh Approach with k-ω model of turbulence

For both tested grids, moving mesh approach was applied with *k*-*ω* model of turbulence. This model is recommended for rotational flows and is often applied in turbo machinery. Time dependent solution requires higher computational time, but enables to account for the rotor-stator interaction. During the calculation regular oscillations occur that correspond to passing of the blade along the spiral tongue.

From monitoring of selected variables (velocity, pressure) maximum, average and minimum values of variables can be evaluated, see Figure 17.

It can be seen that the results obtained for both grids are similar, only in the range of dimensionless flow rate from 0.07 to 0.2 a difference can be observed.

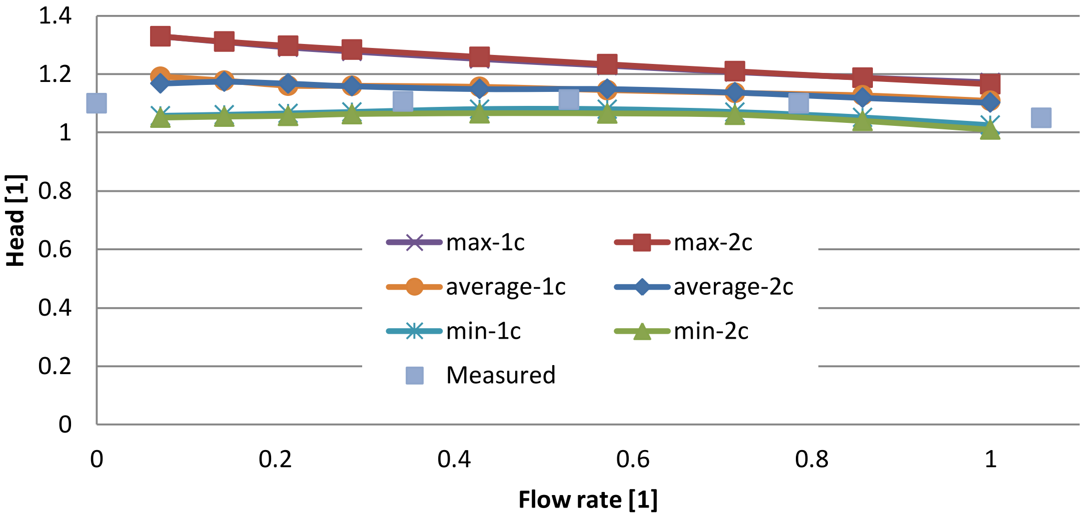

Figure 17 Comparison of results obtained by numerical modelling with Moving Mesh

max-1c	stands for max value of Moving Mesh – non-conformal mesh - 233 259 cells
average-1c	stands for average value of Moving Mesh – non-conformal mesh - 233 259 cells
min-1c	stands for min value of Moving Mesh – non-conformal mesh - 233 259 cells
Measured	stands for value of measurement from Sigma Lutín Group
max-2c	stands for max value of Moving Mesh – conformal mesh - 802 555 cells
average-2c	stands for average value of Moving Mesh – conformal mesh - 802 555 cells
min-2c	stands for min value of Moving Mesh – conformal mesh - 802 555 cells

The head is over predicted for both grids when compared with measurement. This may be caused by the pump geometry simplification. The model does not account for the casing and so the losses are underestimated. In the next chapter, the modelling will be performed on the conformal mesh which will be further adapted to 1 028 416 cells. The difference of predicted values and measured values are about 2÷5%.

5. Comparison of RNG *k-ε* and SST *k-ω* model with measurement

The computational mesh was further refined to 1 028 416 cells. The main objective was to increase the number of grid cells near the blades. Based on Boundary Layer method, Adapt function was applied, which leads to increase of the number of cells. Finally, the number of cells was 1 028 416. RNG *k-ε* model and SST *k-ω* model were applied.

The RNG model was developed using Re-Normalisation Group methods to account for the effects of smaller scales of motion. In SST *k-ω* model transport equations are defined for *k* (turbulent kinetic energy) and *ω* (specific dissipation rate). This model has especially good performance in solution of the flow near wall (boundary). The results in Figure 18 show non dimensional head with value at max, min, and average.

The results are shown below from Figure 18 to Figure 29.

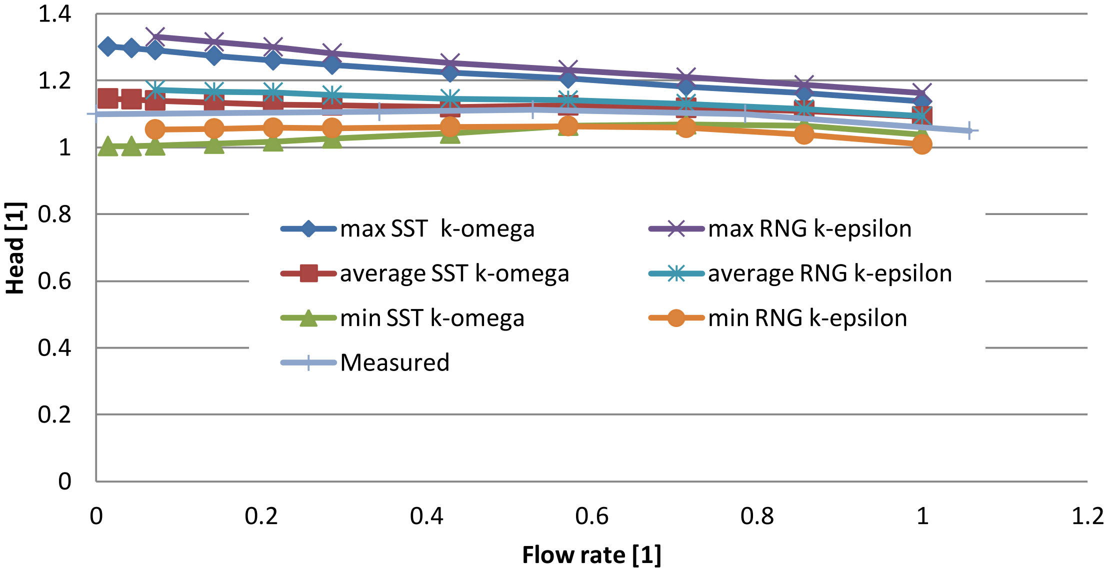

Figure 18 Head at outlet of diffuser for cases RNG *k-ε* and SST *k-ω*

From this comparison we can conclude that the RNG *k-ε* model predicted higher values of head especially for lower values of the flow-rate. The different of predicted values and measured values are only about 2÷3%.

Detail of head oscillation for 0.0207 second (one round) was investigated for various values of relative flow rate and is illustrated in Figure 19.

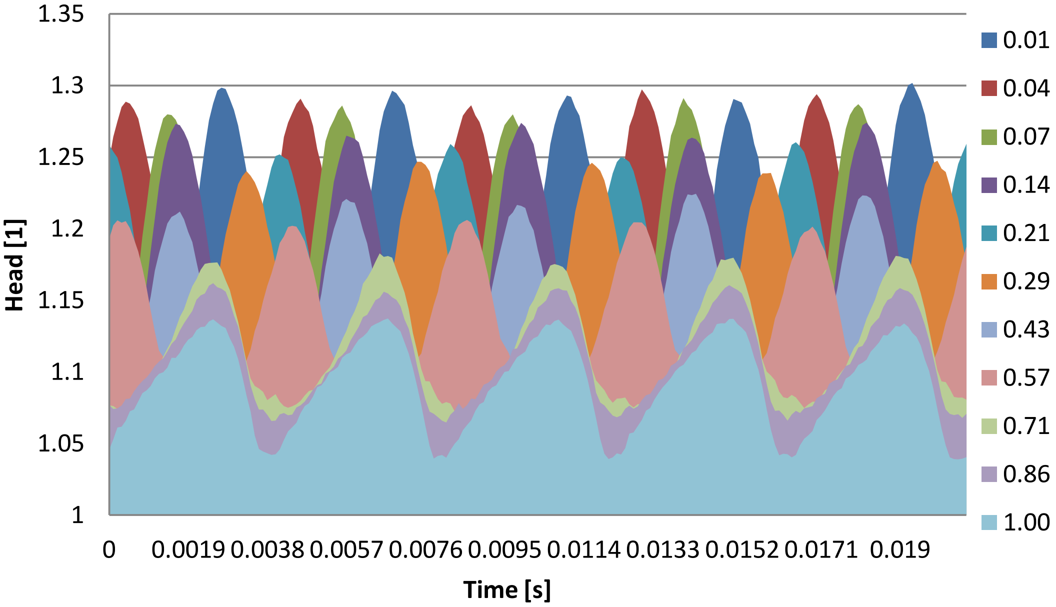

Figure 19 Variable cycle of headwater at outlet in time for difference flow rates

0.01	stands Flow rate = 0.1	$dm^3.s^{-1}$
0.04	stands Flow rate = 0.3	$dm^3.s^{-1}$
0.07	stands Flow rate = 0.5	$dm^3.s^{-1}$
0.14	stands Flow rate = 1	$dm^3.s^{-1}$
0.21	stands Flow rate = 1.5	$dm^3.s^{-1}$
0.29	stands Flow rate = 2	$dm^3.s^{-1}$
0.43	stands Flow rate = 3	$dm^3.s^{-1}$
0.57	stands Flow rate = 4	$dm^3.s^{-1}$
0.71	stands Flow rate = 5	$dm^3.s^{-1}$
0.86	stands Flow rate = 6	$dm^3.s^{-1}$
1.00	stands Flow rate = 7	$dm^3.s^{-1}$ this is $Q = Q_o$

Regular oscillations of head can be observed, the magnitude of which decreases with growing flow rate and reaches the minimum for optimal flow rate. The time period of harmonic function T = 0.0042 [s] and the frequency $f = 1/T = 241$ [s^{-1}], which corresponds to frequency of rotation 48.33 s^{-1} multiplied by number of blades.

To illustrate the results, the contours of static pressure, axial, radial and tangential velocity for Q = 1 [1], k-ω model and unsteady flow are presented from Figure 20 to Figure 23.

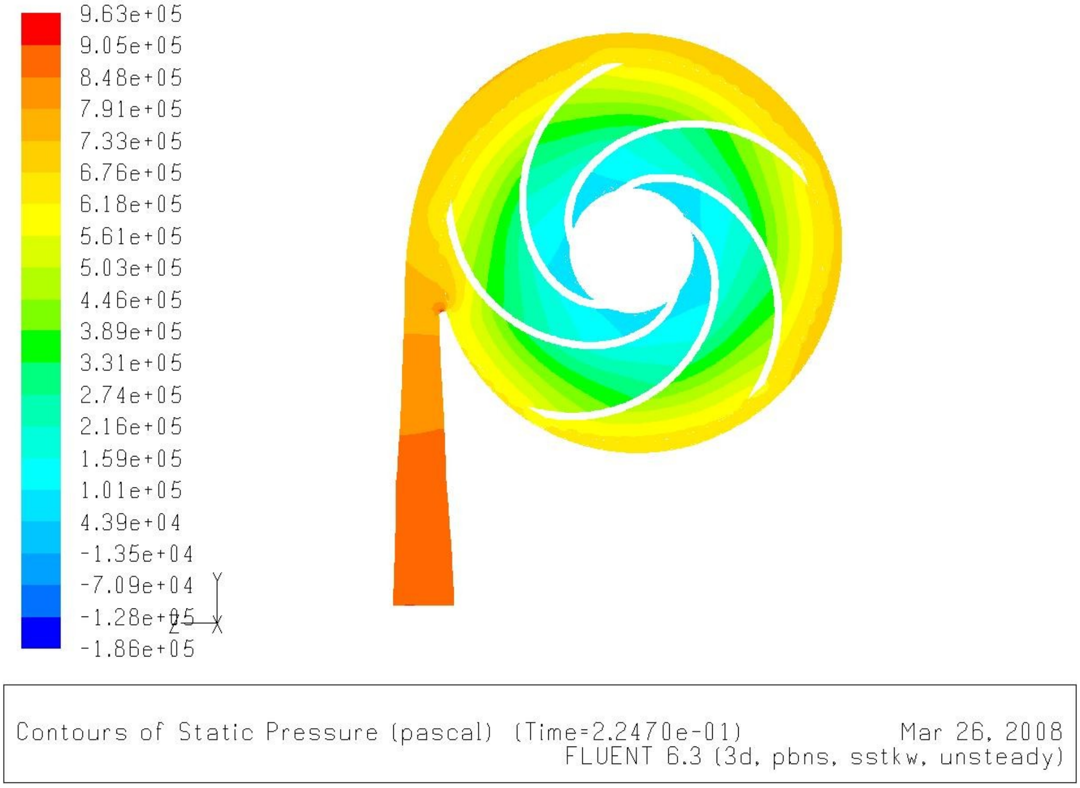

Figure 20 Static Pressure on Radial Cross-Section

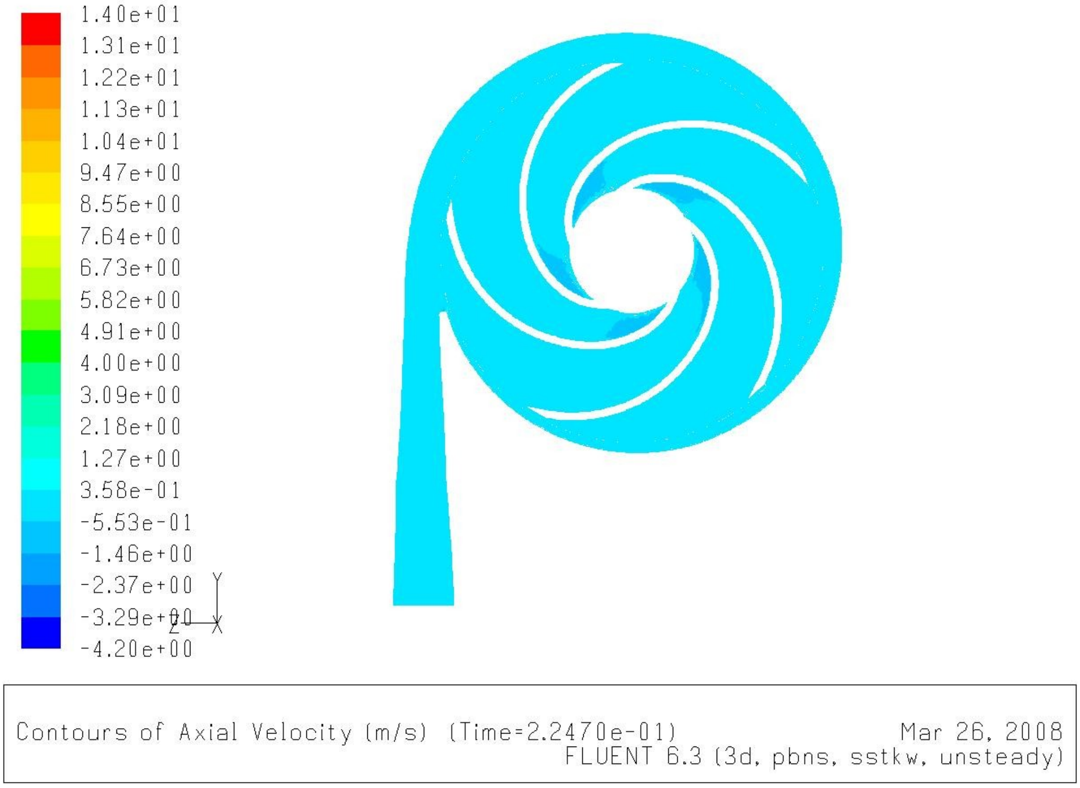

Figure 21 Axial Velocity on Radial Cross-Section

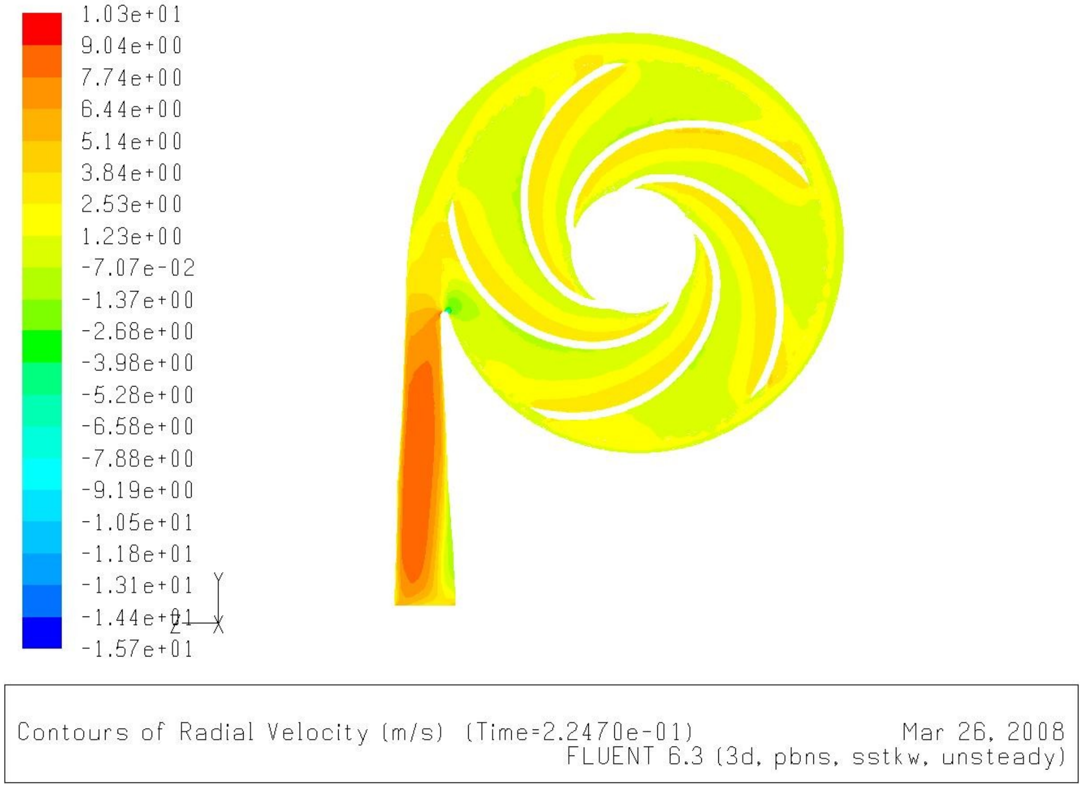

Figure 22 Radial Velocity on Radial Cross-section

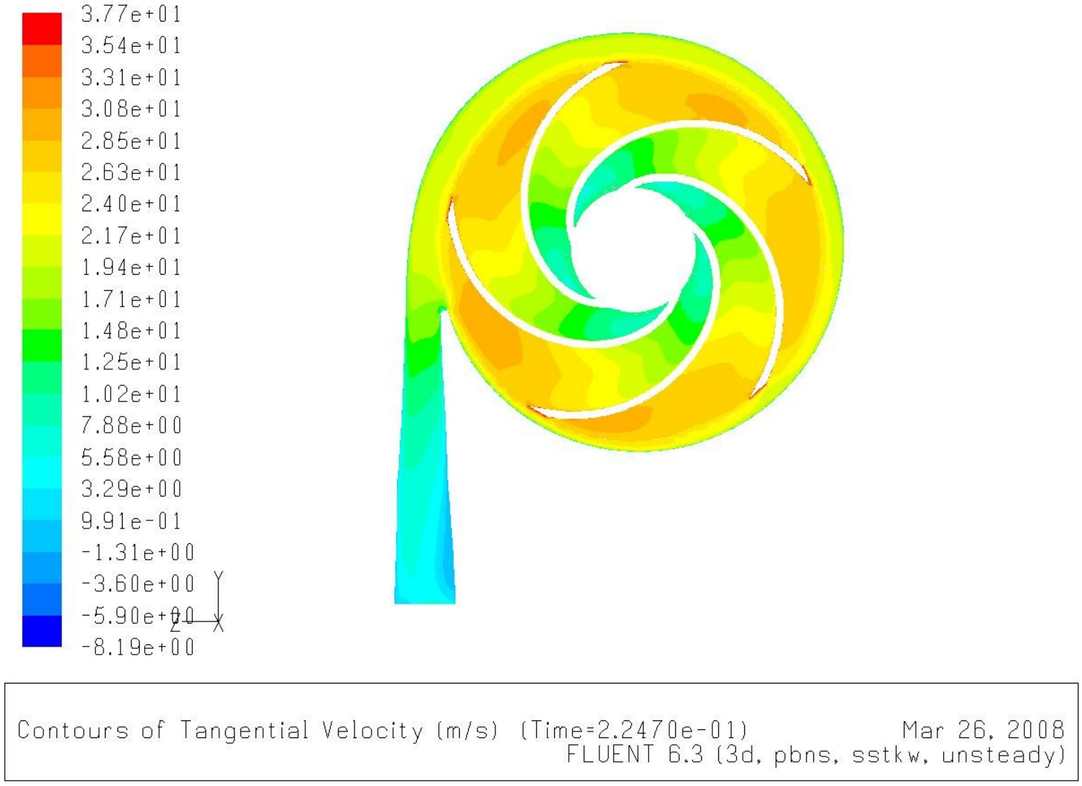

Figure 23 Tangential Velocity on Radial cross-section

From Figure 20, it can be seen the pressure drop at a certain point below the pressure of saturated vapour. This could lead to cavitation. In this work the cavitation model was not applied, but in general Fluent enables solution of problems in which cavitation is of interest.

Convergence history of velocity magnitude was determined for various values of flow rate to evaluate the range of oscillation (see Figure 24).

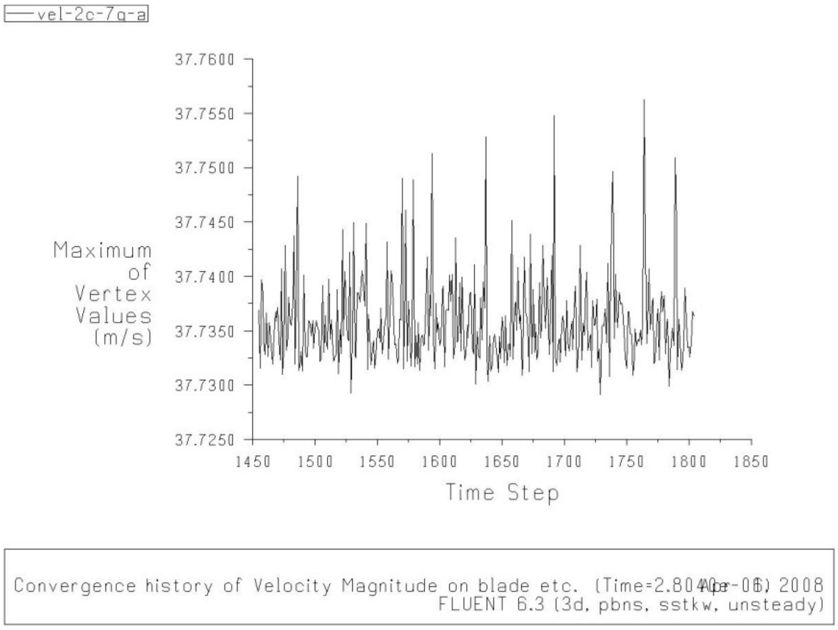

Figure 24 Graph of velocity magnitude on impeller with flow rate *Q* = 7 dm^3.s^{-1}

We can see that velocity magnitude is nearly constant in time which corresponds to Figure 24, where minimal oscillations were evaluated for optimal value of flow-rate. With decreasing flow-rate the variation of velocity magnitude in time increases, as can be seen form Figure 25 to Figure 29.

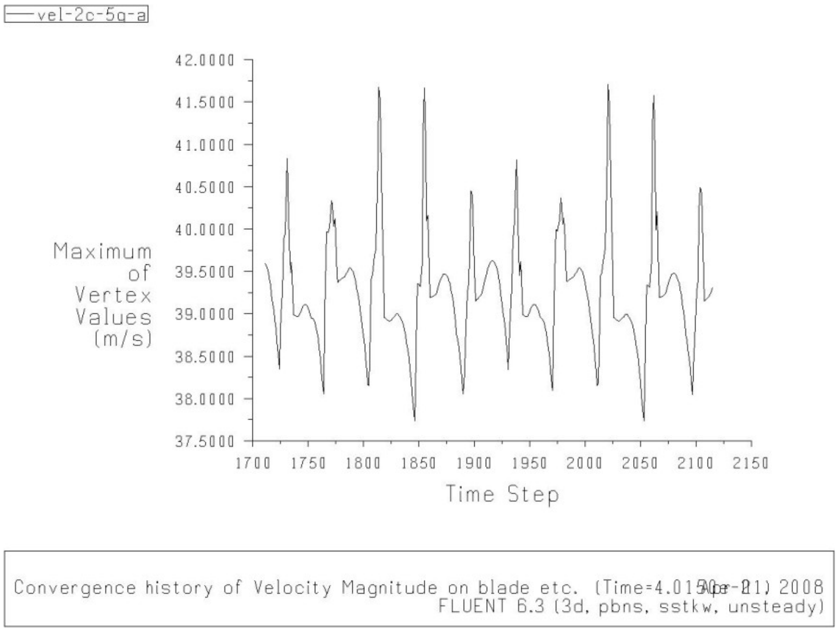

Figure 25 Graph of velocity magnitude on impeller with flow rate *Q* = 5 dm^3.s^{-1}

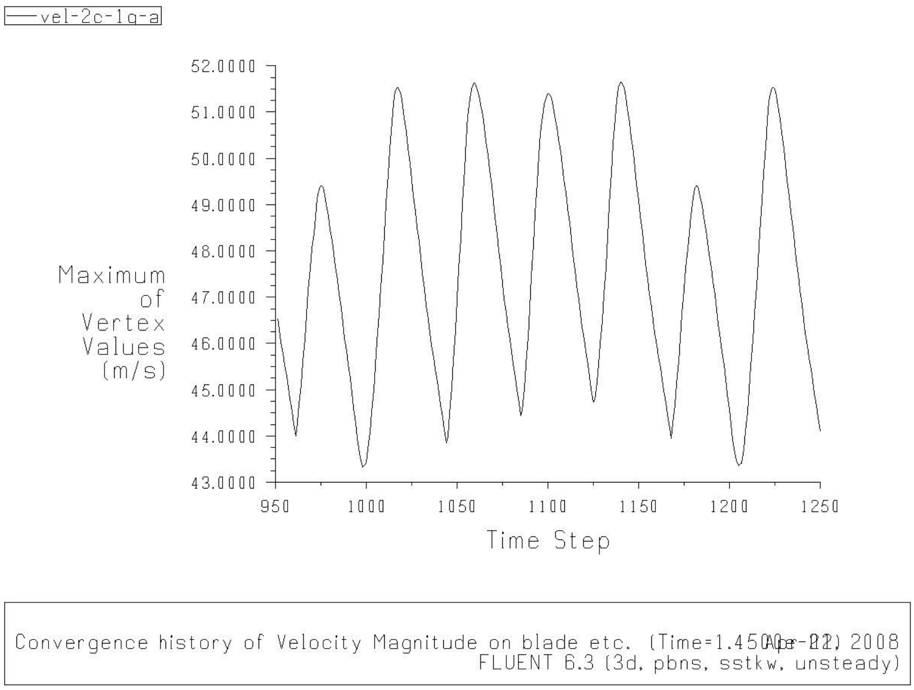

Figure 26 Graph of velocity magnitude on impeller with flow rate Q = 1 $dm^3.s^{-1}$

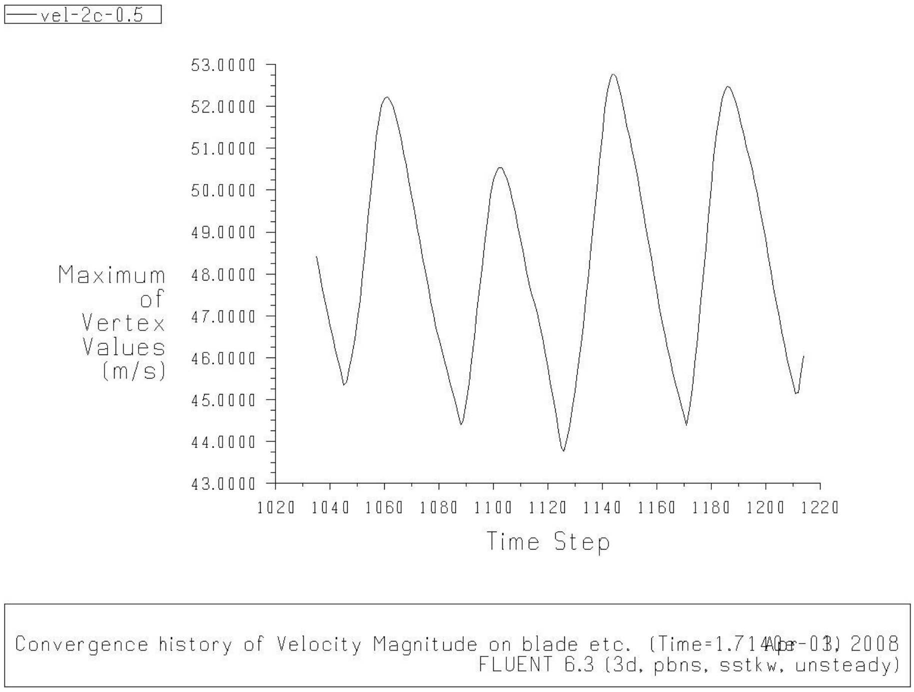

Figure 27 Graph of velocity magnitude on impeller with flow rate Q = 0.5 $dm^3.s^{-1}$

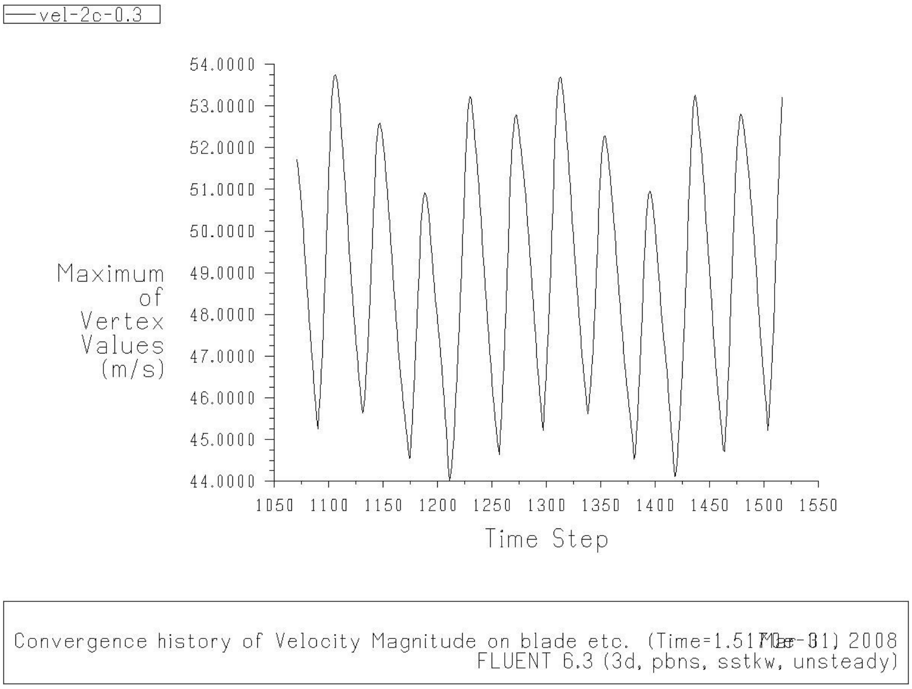

Figure 28 Graph of velocity magnitude on impeller with flow rate *Q* = 0.3 dm^3.s^{-1}

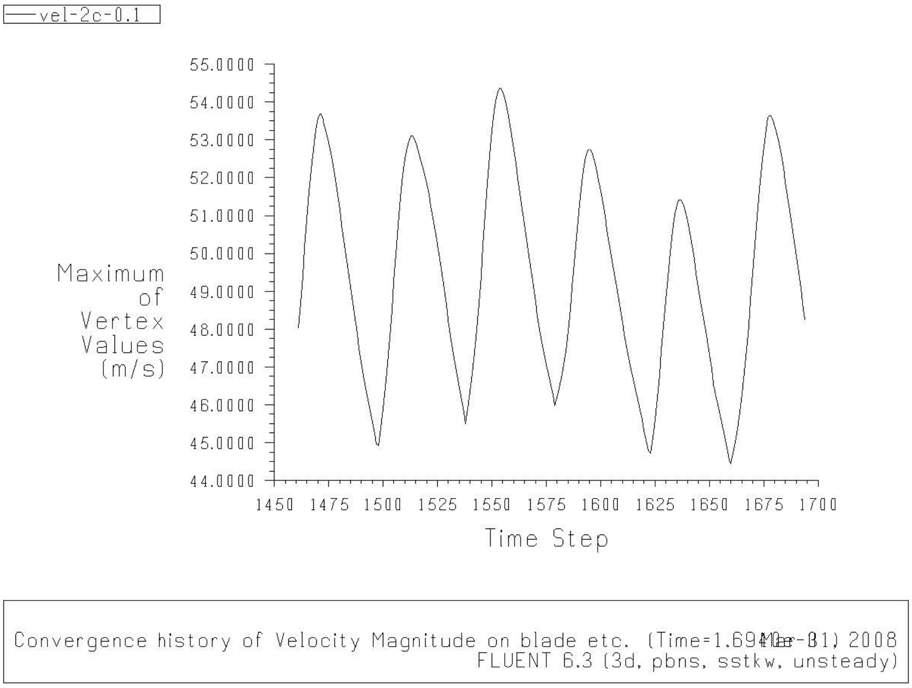

Figure 29 Graph of velocity magnitude on impeller with flow rate *Q* = 0.1 dm^3.s^{-1}

These figures from 24 to 29 show velocity magnitude variation in time for each blade. The impeller has five blades, and result is the same for one round, but for one fifth of round, the max or min velocity is changing.

The differences of max and min velocity are listed in Table 1 below:

Table 1 The range of oscillation of velocity amplitude on blade

Flow rate	[$dm^3.s^{-1}$]	0.1	0.3	0.5	1	5	7
Min value	[$m.s^{-1}$]	44.4	44	43.8	43.3	37.7	37.7290
Max value	[$m.s^{-1}$]	54.4	53.8	52.8	51.5	41.6	37.7575
Difference	[$m.s^{-1}$]	10.0	9.8	9.0	8.2	3.9	0.0285

For $Q = Q_o$, the difference value is minimum 0.0285 $m.s^{-1}$, and it is increasing with decreasing values of flow rate. For $Q = 0.1$ it reaches to 10 $m.s^{-1}$. Oscillations become significant for low values of flow rate Q. It is evident, that prediction of pump performance in case of low flow rates will be less accurate. For these cases it was difficult to achieve converged solution.

6. Physical experiment

The physical experiment was carried out by Sigma Lutín group. *Q~H* curve was measured as well as *Q~P* and *Q~eta* curve. The test results are shown below. The data from measurement were compared with results obtained by numerical modelling.

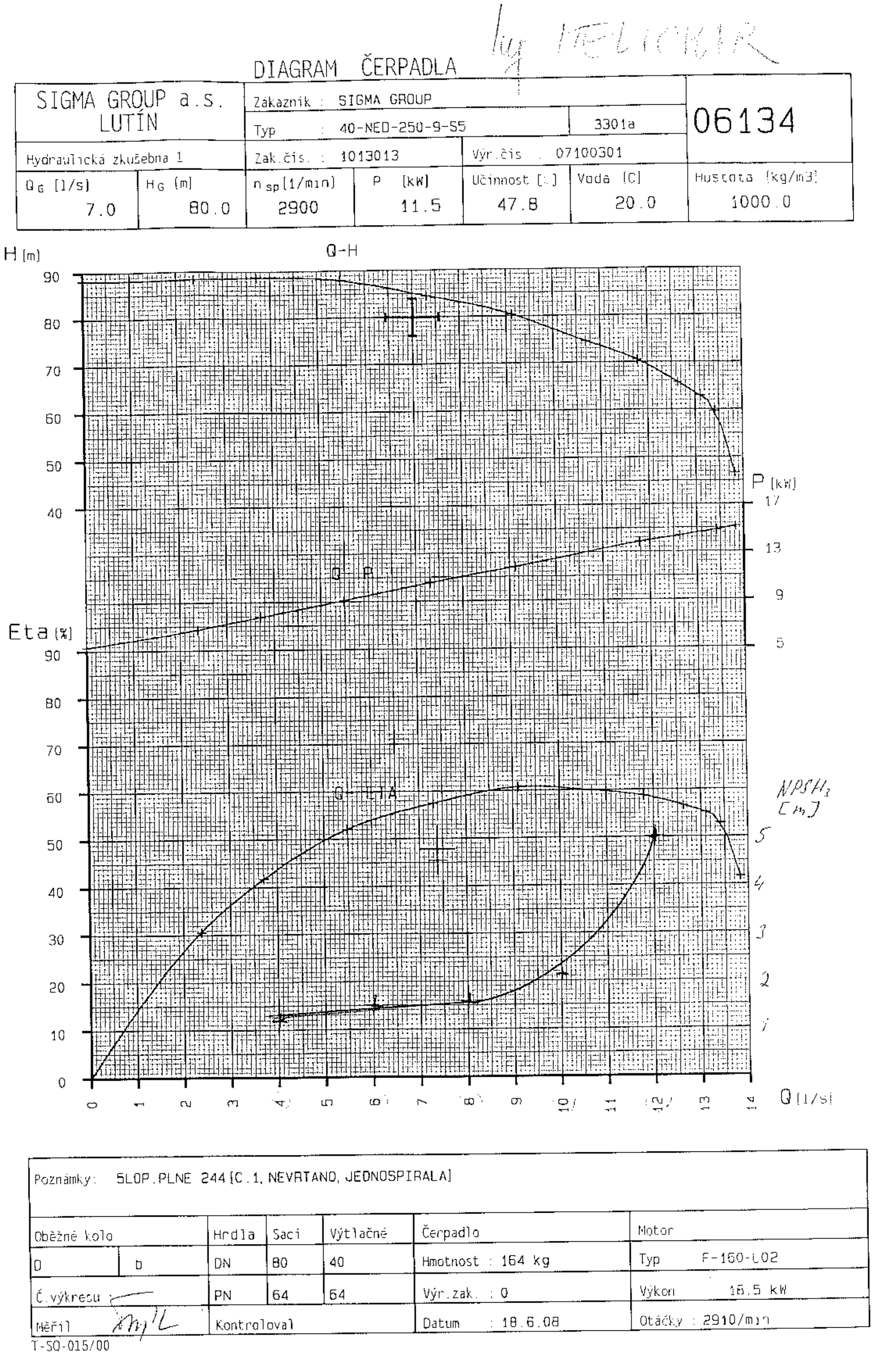

Ing MELICHAR

DIAGRAM ČERPADLA

SIGMA GROUP a.s.
LUTÍN
Hydraulická zkušebna 1
Zákazník : SIGMA GROUP
Typ : 40-NED-250-9-55
3301a
Zak.čis. : 1013013
Výr.čis . 07100301
06134

Q_G [l/s]	H_G [m]	n_{sp} [1/min]	P [kW]	Účinnost [%]	Voda [C]	Hustota [kg/m3]
7.0	80.0	2900	11.5	47.8	20.0	1000.0

Poznámky: 5LOP.PLNE 244 [C.1, NEVRTANO, JEDNOSPIRALA]

Oběžné kolo		Hrdla	Sací	Výtlačné	Čerpadlo	Motor
D	b	DN	80	40	Hmotnost : 164 kg	Typ F-160-L02
Č.výkresu :		PN	64	64	Výr.zak. : 0	Výkon 18.5 kW
Měřil		Kontroloval			Datum : 18.6.08	Otáčky : 2910/min

T-SQ-015/00

Figure 30 Pump performance curves (from Sigma Lutín group)

Values measured on the graph Figure 30 are listed in Table 2 below:

Table 2 Parameters' Relationship of Pump

Q	H	P	ETA
[$dm^3.s^{-1}$]	[m]	[kW]	[%]
0	88	5.4	0
2.4	88.5	6.6	30.5
3.7	89	7.8	42
5.5	88	9	52
7.4	84	10.6	57.5
9.15	80.5	11.8	61
10.7	74.5	13	60
11.78	70.5	13.8	58.7
12.65	65.5	14.2	56.5
13.1	63	14.6	55
13.4	59.5	14.8	53
13.85	46.5	15.2	42

It can be observed that the *Q~H* curve is very flat in the range of flow rate from 0 $dm^3.s^{-1}$ to 5 $dm^3.s^{-1}$ and there is a risk of instability. The *Q~H* curve exhibits a tendency to fall towards shut-off; this type of instability is called “F instability” and is typical in case of low specific speed [32]. The lower the specific speed, the higher is the tendency of a pump towards this type of instability; above n_q = 25 to 30 such instabilities are rather an exception.

The measured head corresponding to the flow rate of 7 $dm^3.s^{-1}$ is higher than assumed in the pump design and reaches about 85 m. Efficiency is about 58%.

The measured data were compared with results obtained with numerical modelling. For this purpose the adapted conformal mesh with 1 028 416 was used. SST *k-ω* model was applied. Modelling was carried out for flow rates ranging from 0.1$dm^3.s^{-1}$ to 14 $dm^3.s^{-1}$, i.e. non-dimensional flow rate varying from 0.014 to 2. Unsteady model was applied.

Boundary conditions were set according to the physical experiment:

- inlet: mass flow rate was set from 0.1 $dm^3.s^{-1}$ to 14 $dm^3.s^{-1}$ with these values: 0.1; 0.3; 0.5; 1; 1.5; 2; 3; 4; 5; 6; 7; 9; 11; 13; 14, and the inlet direction vector x = -1, y = 1, z = 1.
- outlet: outflow condition

The computational parameters leading to the most reasonable result were as follows:

- pressure based solver, 3D, non-stationary, isothermal, turbulent flow.

- *k-ω* SST (2 equations).
- unsteady formulation: 1st Order Implicit.
- time step: 0.0001 [s], max. Number of iterations per time step 20.

The precision of residual was set to 10^{-4} for ω and to 10^{-6} for continuity, x-velocity, y-velocity, z-velocity, and k.

During the computation, the option of monitoring of selected parameters was applied to obtain data for further evaluation.

6.1. Comparison of Q~H curve

To compare relationship *Q~H* with Figure 30, the results obtained with SST *k-ω* model and adapted grid were used. The comparison is in figure below:

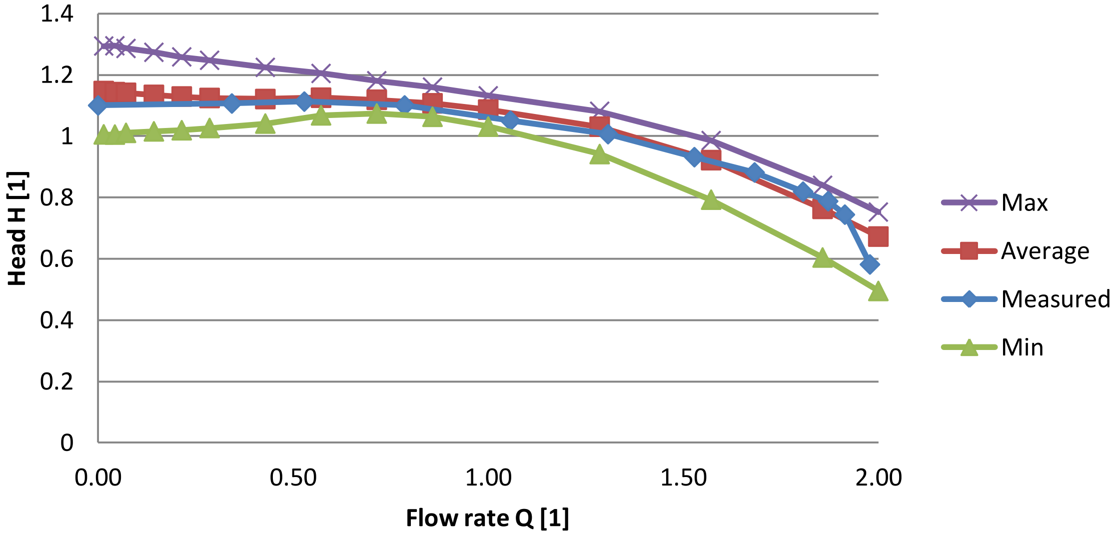

Figure 31 Relationship Flow rate *Q* [1] ~ Head *H* [1]

The measured *Q~H* curve exhibits suspicion of instability, which was not proved by numerical investigation, however it must be emphasized again, that for low values of the flow rate the inaccuracy in head prediction must be expected. Behind the non-dimensional flow rate of 1.857 [1] a sudden head drop can be observed in case of measurement, which can be caused by cavitation. In numerical simulation cavitation model was not included. Around the best efficiency point (BEP) the results are in good agreement.

6.2. Comparison efficiency curve

The numerical experiment shows hydraulic efficiency, but the measured data show total efficiency. We must calculate hydraulic efficiency from measured values by equation (26):

$$\eta_{hydraulic} = \sqrt{\eta_{total}} - 0{,}03 \tag{26}$$

From equation

$$P = M\,\omega \tag{27}$$

the moment can be calculated

$$\begin{aligned} M &= \frac{P}{\omega} \\ &= \frac{P_{hydraulic}}{\eta\,\omega} \\ &= \frac{Q\,\Delta p}{\eta\,\omega} \end{aligned} \tag{28}$$

Then, the Fluent hydraulic efficiency can be calculated by equation:

$$\eta_{Fluent\_hydraulic} = \frac{Q\,\Delta p}{M\,\omega} = \frac{Q\left(p_{t2} - p_{t1}\right)}{M\,\omega} \tag{29}$$

where

p_{t1} is total pressure at inlet of pump

p_{t2} is total pressure at outlet of pump

M is general moment (torque) of impeller on x-axis

ω is angular velocity

The total pressure at inlet and outlet of the pump can be evaluated from numerical simulation. The moment of pump's runner can be derived by equation:

$$M = \left(\int_S \left(\vec{r}\ x \left(\overline{\overline{\tau}} \cdot \hat{n} \right) \right) dS \right) \cdot \hat{a} \tag{30}$$

where

S area of all parts

$\overline{\overline{\tau}}$ total stress tensor

$\hat{n}$ unit vector in the direction normal to the surface

$\vec{r}$ position vector

$\hat{a}$ unit vector parallel to the axis of rotation

In the Fluent package, the total force component along the specified force vector $\vec{a}$ on a wall zone is computed by summing the dot product of the pressure and viscous forces on each face with the specified force vector. The terms in this summation represent the pressure and viscous force component in the direction of the vector $\vec{a}$ [12]:

$$\underbrace{F_a}_{\text{total force component}} = \underbrace{\vec{a} \cdot \vec{F}_p}_{\text{pressure force component}} + \underbrace{\vec{a} \cdot \vec{F}_v}_{\text{viscous force component}} \tag{31}$$

where

$\vec{a}$ specified force vector

$\overrightarrow{F}_p$	pressure force vector
$\overrightarrow{F}_v$	viscous force vector

The total moment vector about a specified centre A is computed by summing the cross products of the pressure and viscous force vectors for each face with the moment vector $\overrightarrow{r}_{\mathrm{AB}}$, which is the vector from specified moment centre A to the force origin B (see Figure 32). The terms in this summation represent the pressure and viscous moment vectors:

$$\underbrace{\overrightarrow{M}_{\mathrm{A}}}_{\text{total moment}} = \underbrace{\overrightarrow{r}_{\mathrm{AB}} \times \overrightarrow{F}_p}_{\text{pressure moment}} + \underbrace{\overrightarrow{r}_{\mathrm{AB}} \times \overrightarrow{F}_{\mathrm{v}}}_{\text{viscous moment}} \tag{32}$$

where

A	specified moment centre
B	force origin
$\overrightarrow{r}_{\mathrm{AB}}$	momentum vector
$\overrightarrow{F}_p$	pressure force vector
$\overrightarrow{F}_v$	viscous force vector

Direction of the total moment vector follows the right hand rule for cross products.

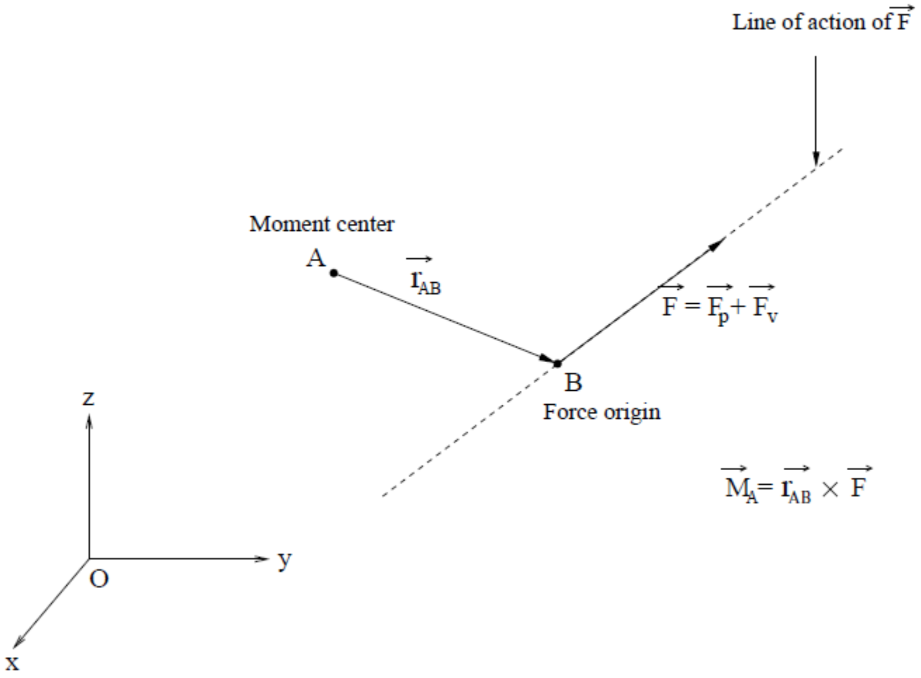

Figure 32 Moment about a specified moment centre [12]

The total moment M_x can be evaluated from CFD Fluent and gives positive value

$$M = |M_x| \tag{33}$$

The angular velocity can be calculated by equation:

$$\omega = \frac{2\pi\, n}{60} = \frac{2\pi \cdot 2900}{60} = 303\left[\,\mathrm{rad.s^{-1}}\right] \tag{34}$$

The comparison of efficiency is shown in Figure 35.

Moment centre is a point on axis X with x = 4.55 mm = 0.00455 m.

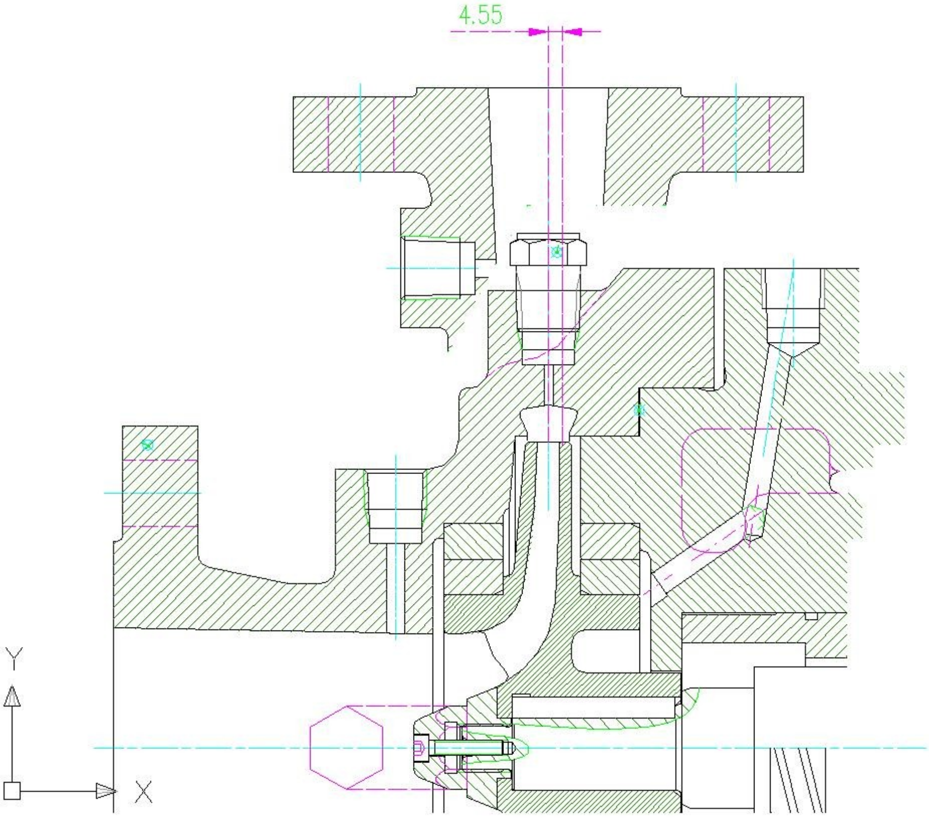

Figure 33 Scheme of the pump with the coordinate system

The moments are calculated for Wall Zone ***blade*** (impeller). The dialogue has been shown on Figure 34 below.

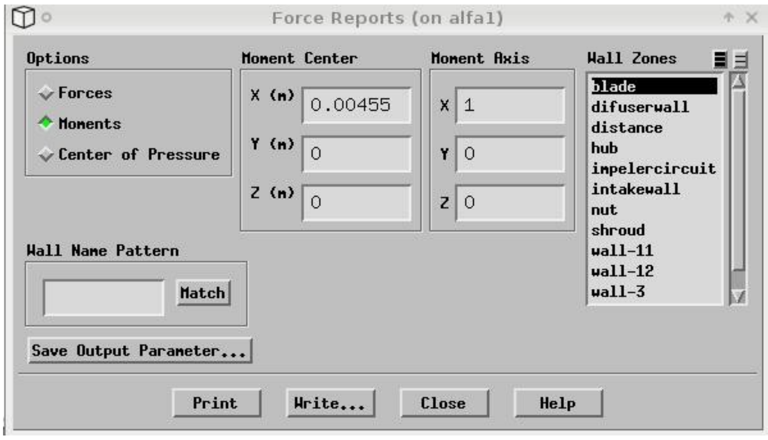
Force Reports (on alfa1)

Options
◇ Forces
◆ Moments
◇ Center of Pressure

Moment Center
X (m) 0.00455
Y (m) 0
Z (m) 0

Moment Axis
X 1
Y 0
Z 0

Wall Zones
blade
difuserwall
distance
hub
impelercircuit
intakewall
nut
shroud
wall-11
wall-12
wall-3

Wall Name Pattern

Figure 34 Dialogue of moment calculation

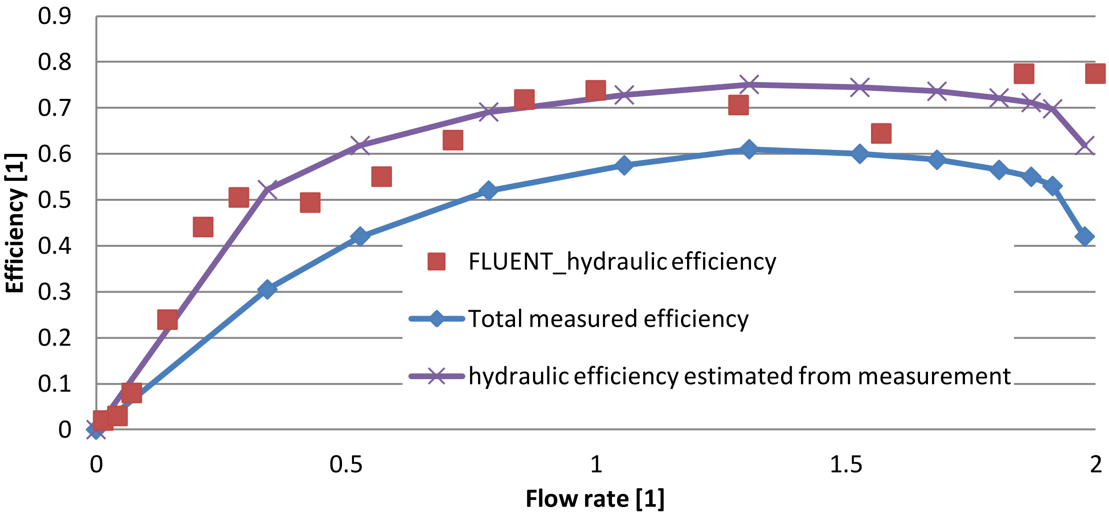

Figure 35 Relationship of Flow rate and Efficiency

At design point with flow rate *Q* = 7 dm^3.s^{-1}, the hydraulic efficiency evaluated from measured data according to equation (26) and hydraulic efficiency predicted by numerical modelling are in good agreement. But for lower and also higher values of flow rate, calculated efficiency and measured efficiency have larger imparity. In the chapter 8, the efficiency will be calculated with new model which includes also the pump casing.

6.3 The dissipation function

The hydraulic efficiency calculated from the power balance does not allow estimating the contribution of individual pump components to the losses. To obtain such estimation, the loss in individual pump hydraulic parts must be investigated. For this purpose an approach can be applied which is based on evaluation of dissipation performance.

The hydraulic efficiency includes all hydraulic losses between the suction and discharge nozzles, i.e. in the inlet, impeller, diffuser and discharge casing. It is possible do derive the input power of the pump *P* as the sum of hydraulic power and a power dissipation

$$P = \rho Y Q + 2 D_s \tag{35}$$

Hydraulic efficiency can be defined as a ratio of power output and input

$$\eta_h = \frac{P_{hydraulic}}{P} = \frac{\rho Q_v Y}{\rho Q_v Y + 2 D_s} \tag{36}$$

For fluid mechanical energy loss per unit time (power dissipation) an expression is valid

$$2D = \eta \int_V S_{ij} S_{ij} dV \tag{37}$$

where η is the dynamic viscosity and the velocity deformation tensor S_{ij} is defined by [12]:

$$S_{ij} = \frac{1}{2}\left(\frac{\partial u_j}{\partial x_i} + \frac{\partial u_i}{\partial x_j}\right) \qquad (38)$$

In Fluent the *Strain rate* [s^{-1}] can be evaluated from *Derivatives* category. The volume integral (see Figure 36) is computed by summing the product of the cell volume and the selected field variable:

$$\int \phi dV = \sum_{i=1}^{n} \phi_i |V_i| \qquad (39)$$

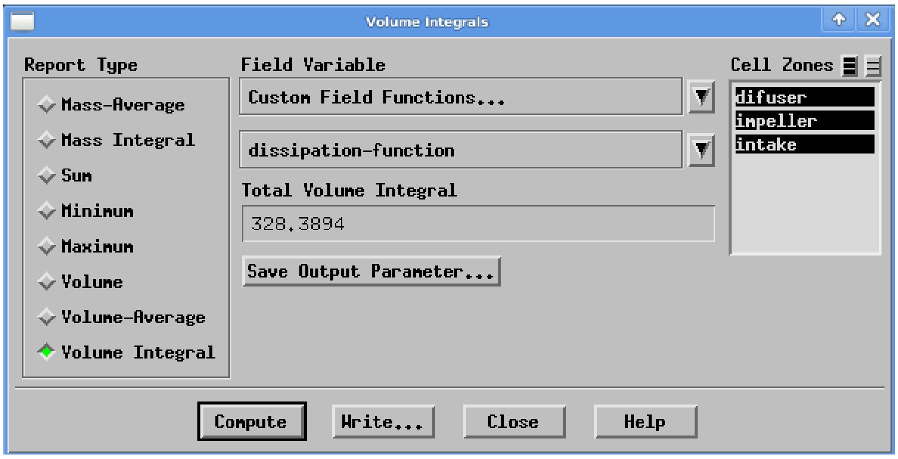

Report Type: ● Volume Integral

Field Variable: Custom Field Functions...

dissipation-function

Total Volume Integral: 328.3894

Cell Zones: difuser, impeller, intake

Figure 36 Dialogue of Volume Integral [12]

6.3.1 Dissipation function in laminar pipe flow

To verify the method, the steady flow in a horizontal pipe of constant cross-section (diameter *d* = 15mm) and length *l* = 1m was modelled as 3D problem. To ensure laminar flow, high viscosity liquid was defined to reach low Reynolds number. The basic parameters and physical constants are defined in the Table 3 below.

Table 3 Pipe parameters in case of laminar pipe flow

Pipe parameters			
Pipe diameter	d =	0.015	m
Pipe length	l =	1	m
Mean pipe velocity	v =	6	m.s^{-1}
Liquid: Engine-Oil			
Density	ρ =	889	kg.m^{-3}
Dynamic viscosity	μ =	1.06	Pa.s
Kinematic viscosity	ν =	0.001192	m^2.s^{-1}

Flow of a fluid in a pipe requires mechanical energy. In a horizontal pipe of uniform cross-section and steady flow, the mechanical energy is completely dissipated as there is no acceleration and no change in the potential energy. The pressure drop (friction loss) along the pipe length l can be calculated using the Darcy-Weisbach formula:

$$\Delta p = \lambda \cdot \frac{l}{d} \cdot \frac{v^2}{2} \rho = 0.8478 \cdot \frac{1}{0.015} \cdot \frac{6^2}{2} \cdot 889 = 904533.3 [\mathrm{Pa}] \tag{40}$$

where λ means friction coefficient

$$\lambda = \frac{64}{\mathrm{Re}} = \frac{64}{75.48} = 0.8478 \tag{41}$$

and Reynolds number corresponds to laminar flow

$$\mathrm{Re} = \frac{v \cdot d}{\nu} = \frac{6 \cdot 0.015}{0.001192} = 75.48 \; . \tag{42}$$

The calculated power loss:

$$P_z = Q_v \cdot \Delta p = S \cdot v \cdot \Delta p = \frac{\pi d^2}{4} \cdot v \cdot \Delta p = \frac{\pi \cdot 0.015^2}{4} \cdot 6 \cdot 904533.3 = 959.1 [\mathrm{W}] \tag{43}$$

Numerical modelling has been carried out in Fluent. 3D geometry of the pipe has been created in pre-processor Gambit, computational grid was generated with boundary layers at walls. The reason of 3D solution was the evaluation of volumetric integral according to (39).

Inlet boundary condition was defined by parabolic velocity profile corresponding to laminar flow. The pressure at the inlet and outlet cross-section of the pipe was obtained as *Area weighted average*. Using these values, pressure drop along the distance *l* was determined

$$\Delta p_{Fluent} = 908806.6 [Pa] \tag{44}$$

Using the procedure $Custom\ field\ function \rightarrow volume\ integral \rightarrow strain\ rate$^2

$$\int_V S_{ij} S_{ij} dV = 913.1648 [\mathrm{s^{-2} m^3}] \tag{45}$$

Assuming constant laminar viscosity

$$2D = E = \eta \int_V S_{ij} S_{ij} dV = 967.9547 [\mathrm{W}] \tag{46}$$

The difference of 8 W can be caused by slightly different pressure loss but it is less than 1%.

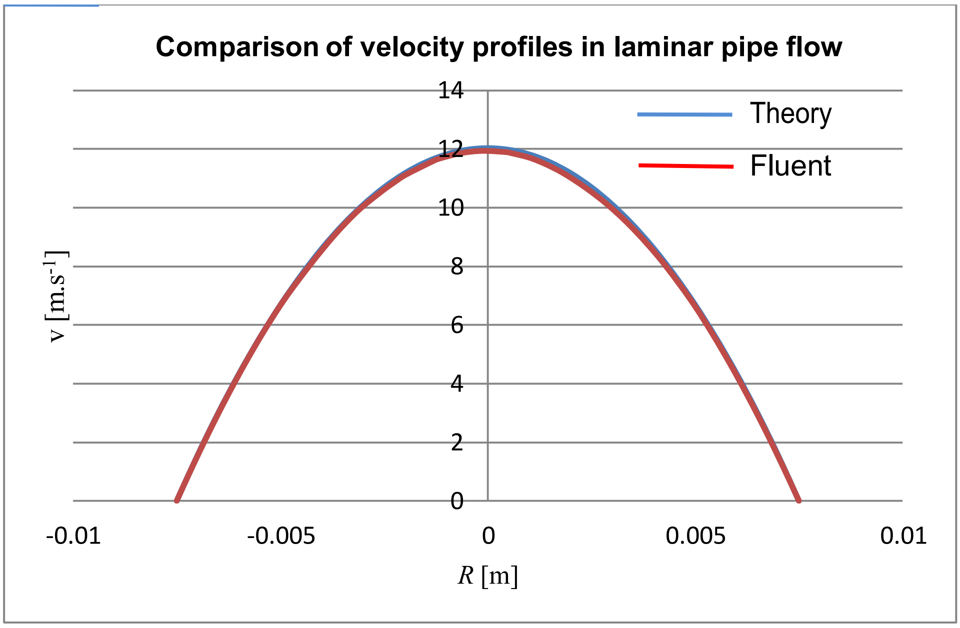

Figure 37 Laminar pipe flow-comparison of theoretical and calculated velocity profile

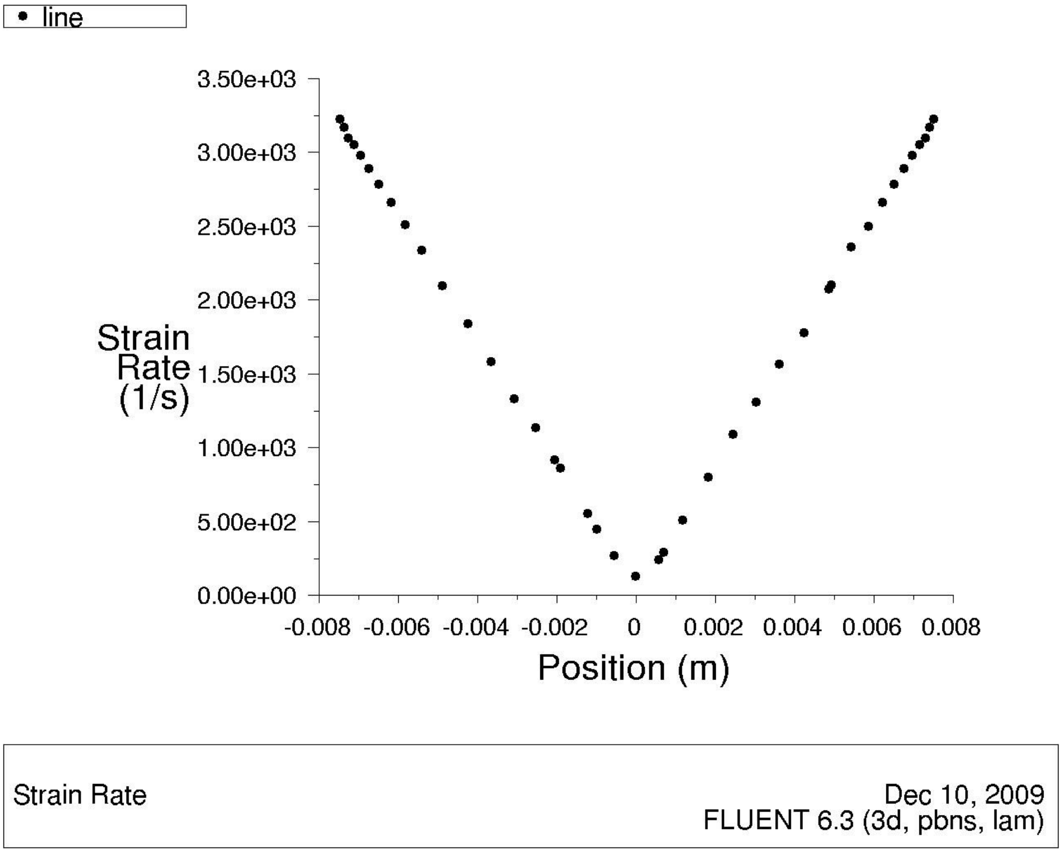

Figure 38 Laminar pipe flow - evaluation of strain rate prediction in the cross-section

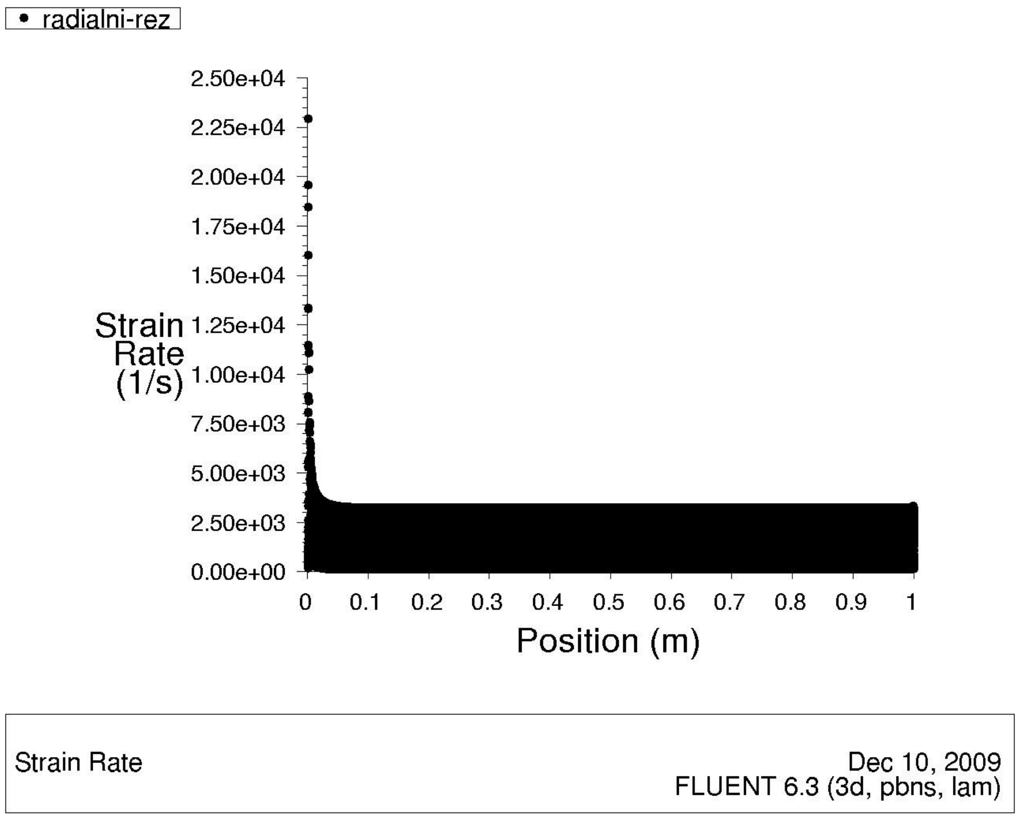

Figure 39 Laminar pipe flow - evaluation of strain rate prediction along the pipe length

6.3.2 Dissipation function in turbulent pipe flow

The same simulation was done for turbulent pipe flow. The basic parameters and physical constants are defined in the Table 4 below.

Table 4 Pipe parameters in case of turbulent pipe flow

Pipe parameters			
Pipe diameter	*d* =	0.015	m
Pipe length	*l* =	1	m
Mean pipe velocity	*v* =	4.5	$m.s^{-1}$
Liquid: Engine-Oil			
Density	ρ =	998.2	$kg.m^{-3}$
Dynamic viscosity	μ =	0.001003	Pa.s
Kinematic viscosity	ν =	0.000001	$m^2.s^{-1}$

Calculated value of the Reynolds number corresponds to the smooth pipe turbulent flow

$$\mathrm{Re} = \frac{v \cdot d}{\nu} = \frac{4.5 \cdot 0.015}{1 \cdot 10^{-6}} = 67000 \qquad (47)$$

The friction coefficient λ was calculated using Blasius formula

$$\lambda = \frac{0.3164}{\sqrt[4]{\mathrm{Re}}} = \frac{0.3164}{\sqrt[4]{67000}} = 0.019653\,[1] \qquad (48)$$

The pressure drop (friction loss) along the pipe length *l* can be calculated using the Darcy-Weisbach formulae:

$$\Delta p = \lambda \cdot \frac{l}{d} \cdot \frac{v_s^2}{2} \cdot \rho = 0.019653 \cdot \frac{1}{0.015} \cdot \frac{4.5^2}{2} \cdot 998.2 = 13241.97 \left[\mathrm{Pa}\right] \tag{49}$$

The calculated power loss

$$P_z = Q_v \cdot p_z = S \cdot v \cdot \Delta p = \frac{\pi d^2}{4} \cdot v \cdot \Delta p = \frac{\pi \cdot 0.015^2}{4} \cdot 4.5 \cdot 13241.97 = 10.53 \left[\mathrm{W}\right] \tag{50}$$

Numerical modelling has been carried out in Fluent. 3D geometry of the pipe has been created in pre-processor Gambit, computational grid was generated with boundary layers at walls. The reason of 3D solution was the evaluation of volumetric integral according to (39).

Inlet boundary condition was defined by power law velocity profile corresponding to turbulent flow in a smooth pipe. The pressure at the inlet and outlet cross-section of the pipe was obtained as Area weighted average. Using these values, pressure drop along the distance l was determined

$$\Delta p_{Fluent} = 13288.96 \left[Pa\right] \tag{51}$$

It can be seen that the pressure drop defined in Fluent is in good agreement with previous calculation. The difference is about 0.355%.

The prediction of the dissipated power was less successful. In turbulent flow we must account for the turbulent viscosity the prediction of which much depends on the applied turbulent model and the grid quality. The turbulent viscosity is dependent of the properties of the flow itself, it can chase with coordinates and in time. In the Table 5 below the range of molecular, turbulent and effective viscosity is presented, which was defined by numeric simulation.

Table 5 The range of viscosity

Molecular (dynamic) viscosity	$\mu =$	0.001003	Pa.s
Turbulent viscosity	$\mu_{\mathrm{turb.}} =$	0.003561 – 0.157	Pa.s
Effective viscosity	$\mu_{\mathrm{eff.}} =$	0.004564 – 0.158	Pa.s

It can be seen that the viscosity is significantly changing within the whole pipe volume. Using the "*Custom field function*", the "*strain rate*" can be multiplied by defined viscosity and then integrated over the volume. By this procedure the dissipated power should theoretically be defined. The results obtained by this approach are given in Table 6.

Table 6 Dissipated power

Definition of viscosity		Dissipated power	
Molecular (dynamic) viscosity	$\mu =$	4.25	W
Turbulent viscosity	$\mu_{\mathrm{turb.}} =$	22.29	W
Effective viscosity	$\mu_{\mathrm{eff.}} =$	26.54	W
Calculate dissipated power		10.53	W

It is evident that numerical simulation of this turbulent pipe flow leads to nearly three times higher values of dissipated power if effective viscosity is accounted for.

Further attempts were made to investigate the influence of turbulence models, grid quality and the near wall modelling technique. For the mesh in the near-wall region, different strategies had been tested [12].

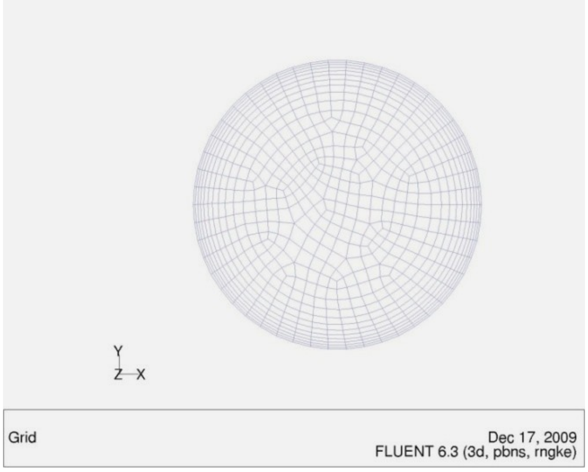

3D_1 - 771.012 cells

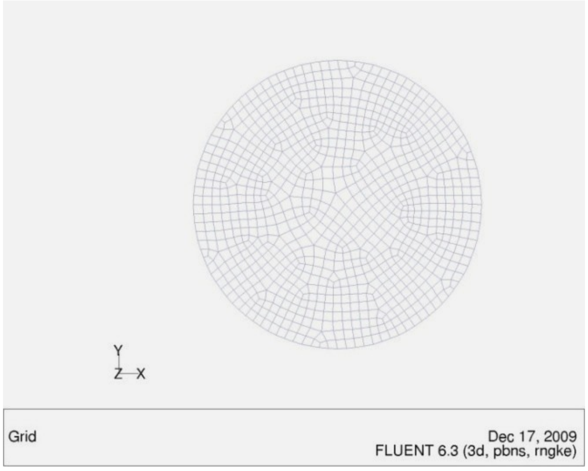

3D_2 - 1.892.824 cells

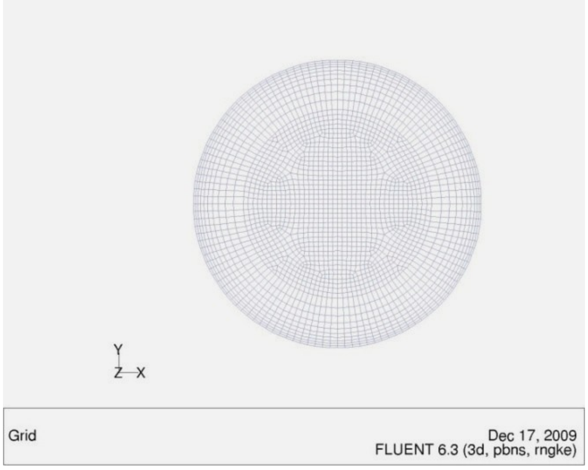

3D_4 - 2.484.000 cells

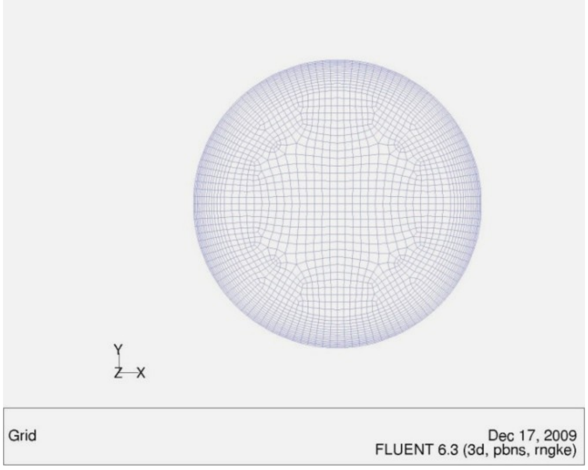

3D_5 - 2.724.000 cells

In spite of the extended testing of turbulent models applied on different grid, no unique grid or turbulence model can be mentioned as the most suitable. The results differed in hundreds of percent. The most accurate results if compared with the calculation according to (50) were reached with 3D_1 grid, which was further adapter to reach the value of Y^* near 11. Non equilibrium wall function was applied. It can be concluded, the control of grid quality and appropriate technique of wall bounded flow modelling is of great importance in this case. The quality of the near-wall mesh can be controlled by displaying the values of Y^*, which is the distance between the cell centroid and the wall for wall-adjacent cells defined by [12]:

$$y^* = \frac{\rho k_P^{1/2} C_\mu^{1/4} \Delta y_P}{\mu} \tag{52}$$

where

κ	von Kármán constant (=0.42)	[1]
E	empirical constant (=9.81)	[1]
$\overline{u}_p$	mean velocity of the fluid at point *P*	[ms $^{-1}$]
k_p	turbulent kinetic energy at point *P*	[m ^{2}s $^{-2}$]
Δy_p	distance from point *P* to the wall	[m]
μ	dynamic viscosity of the fluid	[kg·m $^{-1}$·s $^{-1}$]

The parameters *Y**, *Y+* are solution dependent and they can significantly change with the variables governing the flow as well as with grid adaption. From the testing of turbulent pipe flow no unique conclusion and recommendations for optimum definition of the grid quality and choice of turbulent model can be derived in this case.

6.3.3 Evaluation of dissipated power in hydrodynamic pump

Based on the testing on the simple pipe geometry, as the next step the evaluation of dissipated power was done on the modelled hydrodynamic pump. The main objective was estimating of the contribution of individual pump components to the hydraulic losses, however there exact quantities were not expected to be reached.

Distribution of the strain rate was evaluated near the point of zero discharge and for optimal flow rate. Graphic evaluation of the strain rate in the impeller and the volute in the range up to 5000 s^{-1} shows the opposite trend for the impeller and volute. In the case of the impeller the deformation speed (strain rate) decreases with increasing flow rate (Figure 40), (Figure 41).

(Figure 42) and (Figure 43) show a volute where the speed of deformation on the contrary increases with increasing flow rate. It is possible to say, that local swirl in the runner has extensive influence on the dissipative energy (big value of dissipative energy). Big values of dissipative energy are at the output of the runner to volute casing, too. In the volute case, there are big values of dissipative energy in the region of volute tongue. Results are motivating in the process of hydraulic design.

To calculate the power loss, laminar, turbulent and effective viscosity was substituted to the equation (50) for all main parts of radial pump (intake, impeller, volute). The power loss was evaluated for various values of the dimensionless flow rate ranging from 0.014 [1] to 1.857 [1]. The results are presented in Table 7.

.

Table 7 The power loss of pumps’ parts

	Effective viscosity				Turbulent viscosity				Laminar viscosity			
Q_v	volute	impeller	intake	Total power loss	volute	impeller	intake	Total power loss	volute	impeller	intake	Total power loss
[1]	[W]	[W]	[W]	[W]	[W]	[W]	[W]	[W]	[W]	[W]	[W]	[W]
0.014	141.27	321.74	35.25	498.25	139.54	317.89	35.04	492.47	1.73	3.85	0.208	5.79
0.043	133.88	302.03	31.07	466.98	132.21	298.30	30.88	461.38	1.68	3.73	0.193	5.60
0.071	134.68	291.53	27.16	453.37	132.97	287.88	26.98	447.83	1.71	3.65	0.178	5.54
0.143	138.77	271.84	19.36	429.98	136.86	268.29	19.22	424.37	1.91	3.55	0.144	5.61
0.214	140.50	250.30	14.04	404.84	138.54	246.88	13.92	399.34	1.96	3.42	0.116	5.49
0.286	140.65	237.32	10.51	388.48	138.63	233.98	10.42	383.03	2.02	3.34	0.094	5.45
0.429	146.18	219.17	6.27	371.62	144.02	216.04	6.21	366.27	2.16	3.13	0.066	5.36
0.571	151.23	197.90	3.12	352.25	148.97	195.02	3.08	347.07	2.26	2.88	0.041	5.18
0.714	161.13	167.13	0.13	328.39	158.73	164.48	0.13	323.33	2.40	2.65	0.005	5.06
0.857	175.13	142.83	0.01	317.97	172.56	140.24	0.01	312.81	2.57	2.59	0.001	5.17
1.000	190.25	129.47	0.02	319.74	187.52	126.99	0.02	314.53	2.73	2.48	0.002	5.21
1.286	231.24	107.24	0.04	338.52	228.25	104.85	0.04	333.14	2.99	2.39	0.003	5.38
1.571	349.01	97.09	0.08	446.18	345.64	94.59	0.07	440.31	3.36	2.50	0.004	5.87
1.857	614.59	97.98	0.12	712.70	610.62	95.29	0.12	706.03	3.97	2.69	0.005	6.67

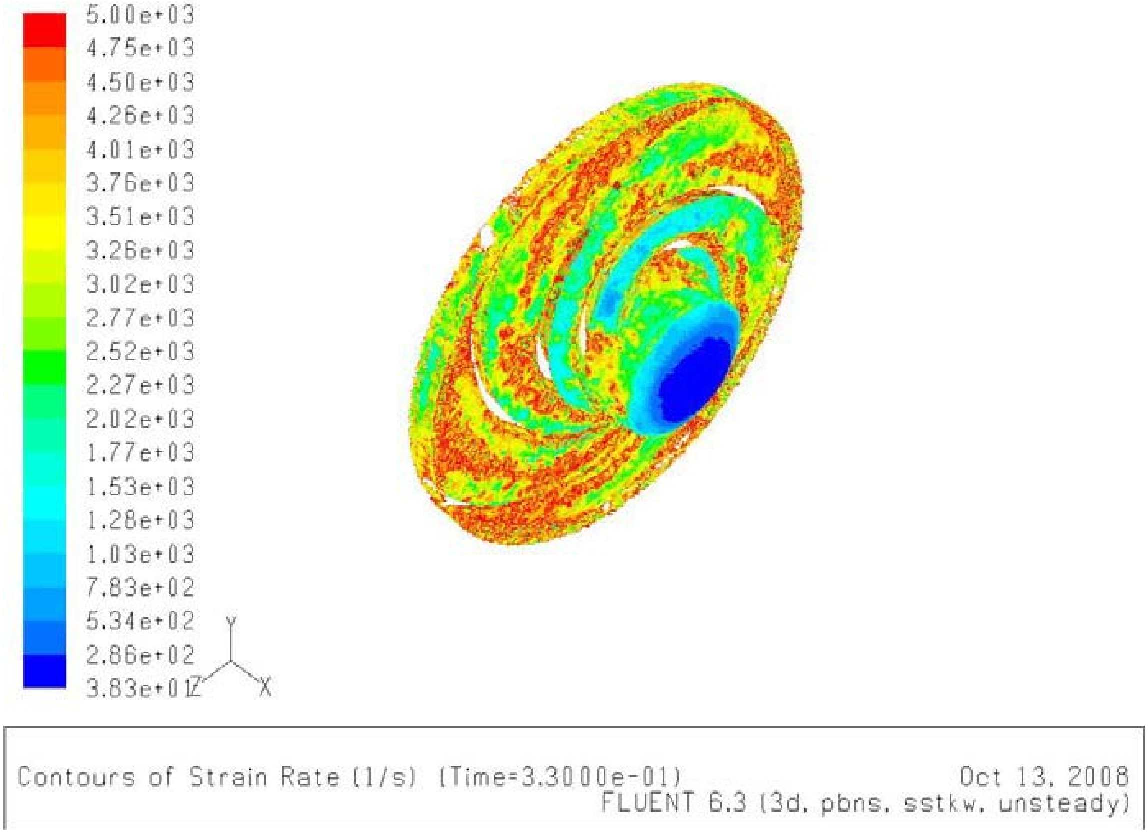

Figure 40 Strain Rate S_{ij}, impeller, Q = 1 dm^3.s^{-1}

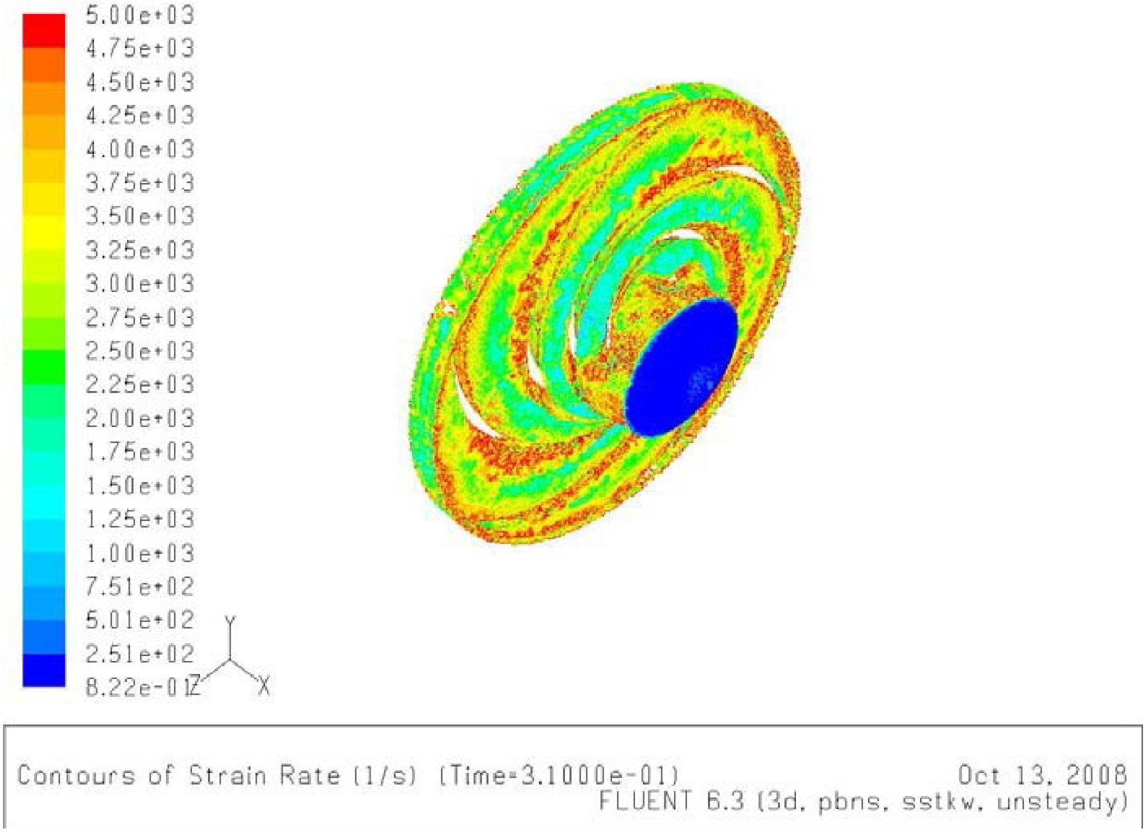

Figure 41 Strain Rate S_{ij}, impeller, Q = 7 dm^3.s^{-1}

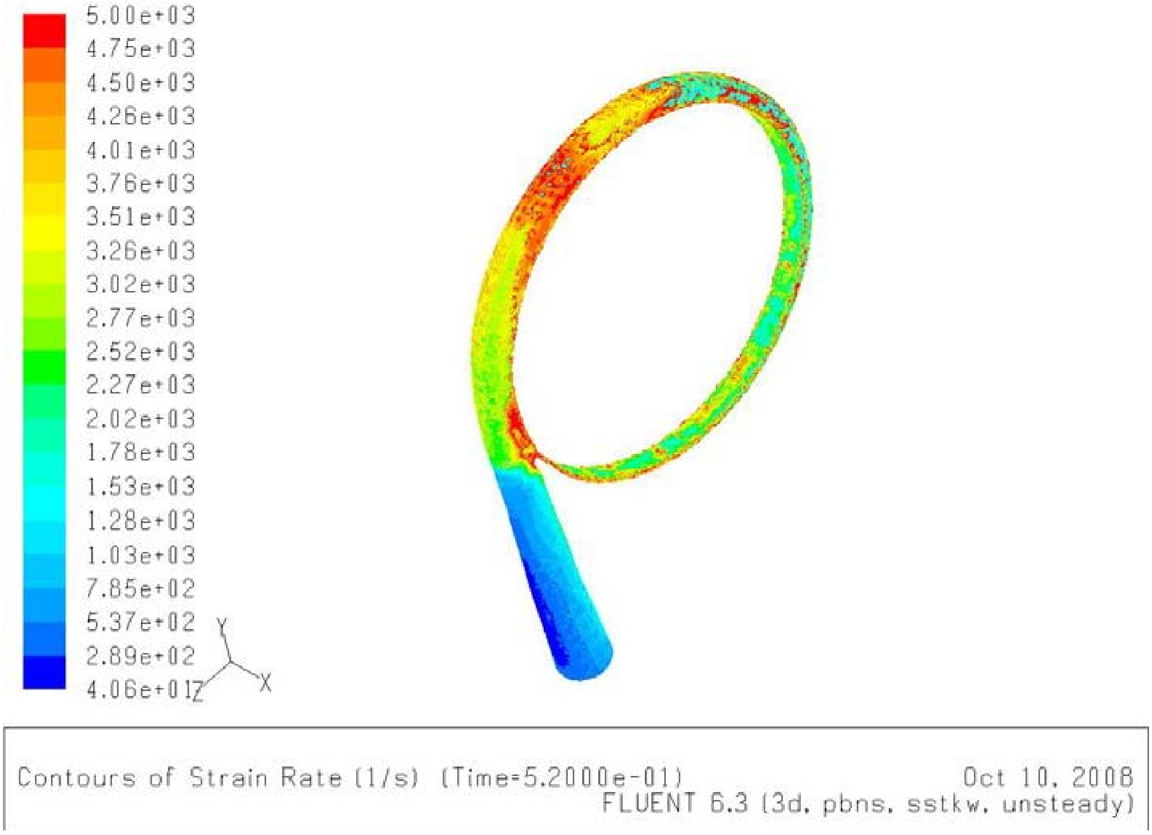

Figure 42 Strain Rate S_{ij}, volute, Q = 1 dm^3.s^{-1}

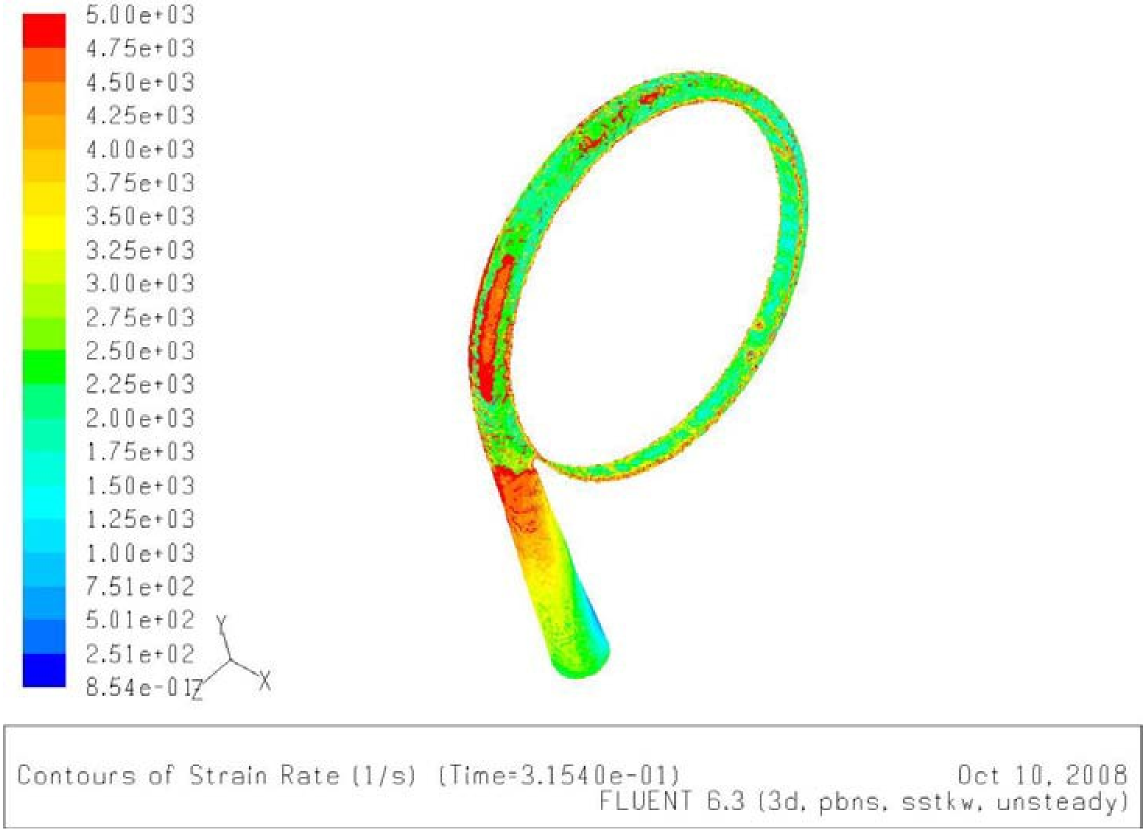

Figure 43 Strain Rate S_{ij}, volute, Q = 7 dm^3.s^{-1}

Diagrams of power loss in dependence on flow rate are shown on Figure 44 to Figure 46. In case of intake dissipated power is decreasing with the growing flow rate. For the impeller and volute opposite trend can be observed. In case of impeller the power dissipation is decreasing with increasing flow rate, for the volute (diffuser) we can see power dissipation increasing with flow rate. The stability is favourably influenced inside of the runner, on the contrary of flow inside of the spiral case. The cause of instability is consequently found out in the spiral case. Therefore the hydraulic design of this part of the pump is very important for *Q~Y* stability.

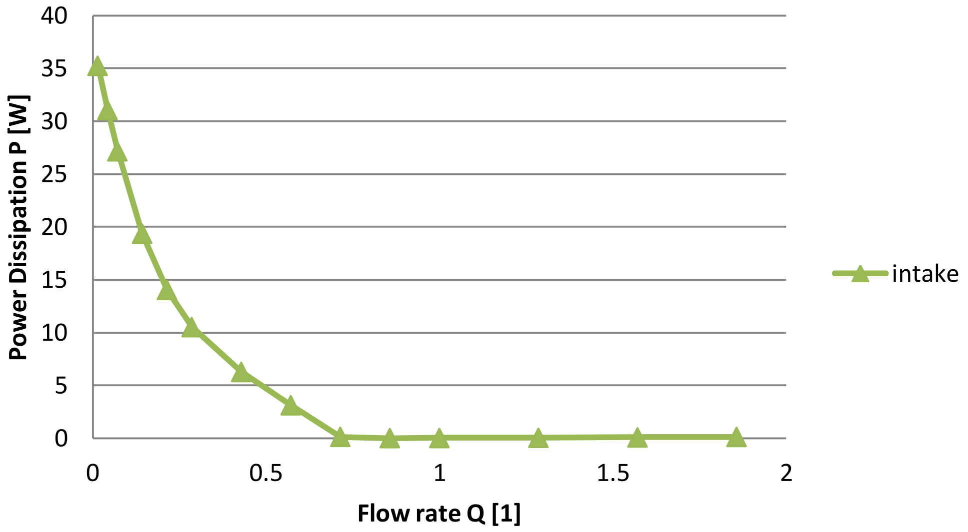

Figure 44 Power Dissipation - intake

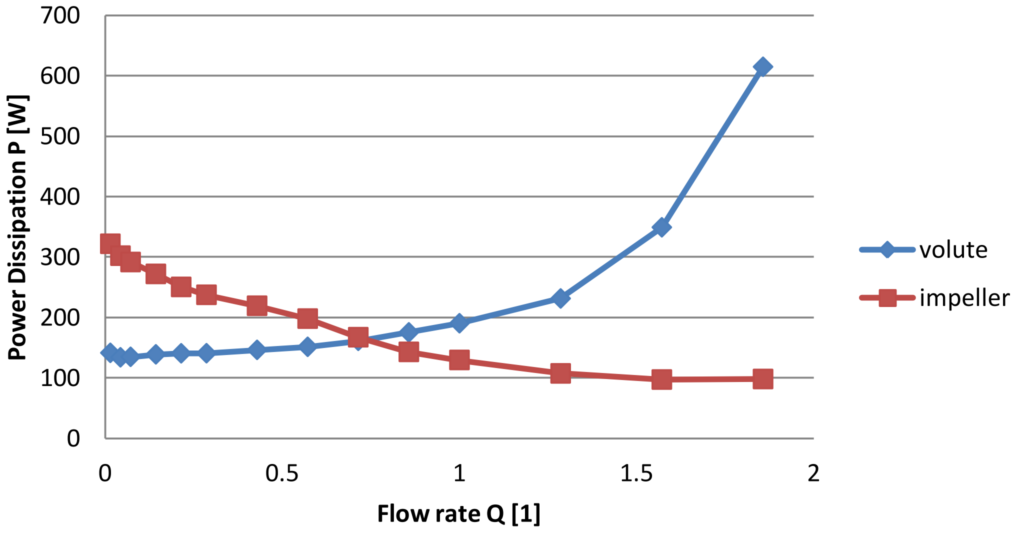

Figure 45 Power Dissipation - impeller and volute

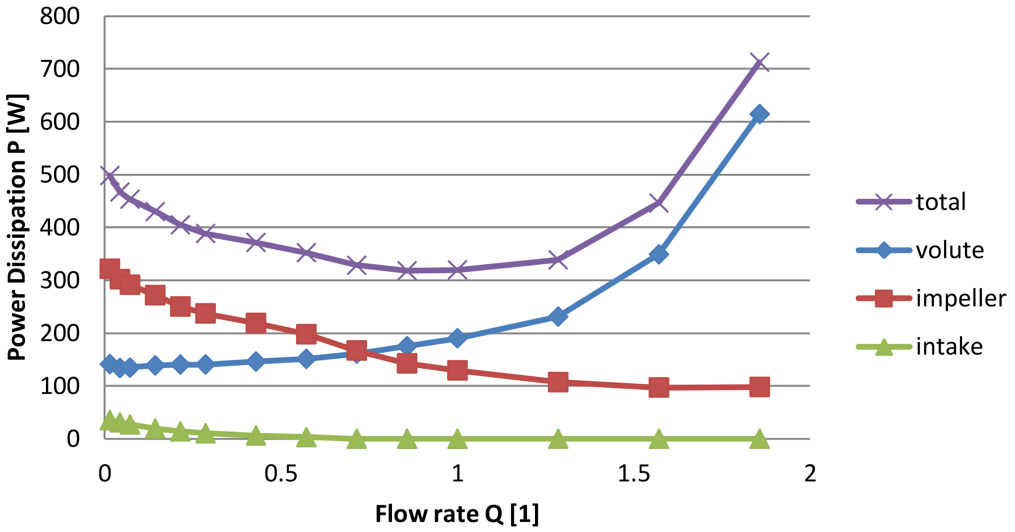

Figure 46 Power Dissipation - overview

The distribution of power dissipation reaches its minimum around $Q = Q_o$, that is also point of best efficiency. However the calculated values are lower than expected and the predicted dissipated power for optimum flow rate is 319.74 W.

If we calculate the dissipate power according to (35) with parameters corresponding to optimum flow rate: $Q_v = 0.007\ \mathrm{m^3.s^{-1}}$; $H = 85$ m; $\eta = 0.57$, this yields:

$$\eta = \frac{\rho Q_v Y}{\rho Q_v Y + 2D} \Rightarrow 2D = \frac{\rho Q_v Y}{\eta} - \rho Q_v Y \qquad (53)$$

and after substitution we obtain.

$$2D = \frac{1000 \cdot 0.007 \cdot 85 \cdot 9.81}{0.57} - 1000 \cdot 0.007 \cdot 85 \cdot 9.81 = 4403.313\ [W] \qquad (54)$$

In the simulation the SST k-ω model was applied and the grid with 1 028 416 cells which contains boundary layer on the blades. However further refinement of the grid leads to rapid increasing of the number of cells. It is very difficult to ensure and control the grid quality near the wall in this complex geometry.

It can be concluded that the prediction of the contribution on losses for main pump parts corresponds to reality, and the dependence of losses on the flow rate gives valuable information, but the amplitude of power losses is inaccurate.

7. Radial force

The pressure rise in the impeller generates hydraulic forces and moments which act on the rotor. In particular forces in axial and radial direction are significant for appropriate sizing of shaft and bearings. While the radial forces is determined by the pressure distribution around the impeller circumference, the axial forces is governed by the flow through the impeller sidewall gaps and the resulting pressure distribution on the shrouds [18].

Both radial and axial hydraulic forces act on the impeller of a centrifugal pump. The radial forces are due to three different mechanisms:

- radial thrust due to non-uniform pressure distribution around the impeller
- labyrinth forces
- impeller-diffuser interaction forces.

7.1. Introduction

The radial force of the impeller is caused by non-uniform pressure distribution around the impeller periphery in centrifugal pump. The value of radial force often is minimal in the best efficiency, but depend experiment from VUT-Brno, the minimal value is min at point which has flow rate *Q* is a bit higher than Q_o. The value of radial force grows high with both lower and higher flow rate. As a result shaft deflection appears, the consequences of severe shaft deflection include high wear rate on bearings, shaft seal leakage, and fatigue bending of the pump shaft.

Design of the volute can affect behaviour and magnitude of radial force. For example double volute (Figure 47) has constant value of radial force over range of capacity, but usually the efficiency decrease. Figure 47 shows relation between radial force and capacity for commonly used type of volute casing.

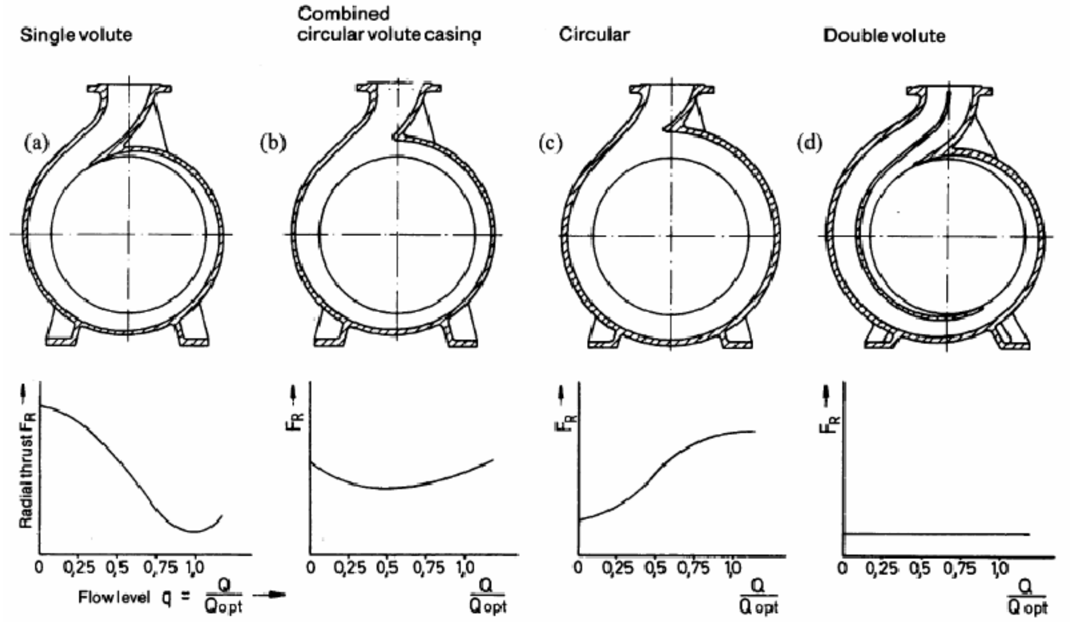

Figure 47 The shape of the volute casing and radial thrust [11]

Numerical modelling was also applied to investigate the flow in this centrifugal pump.

7.2. Results obtained from modelling

In Ansys – Fluent package software, forces acting on selected walls can be reported through the function Reports – Forces – select Wall Zone – blade, as is shown in figure below.

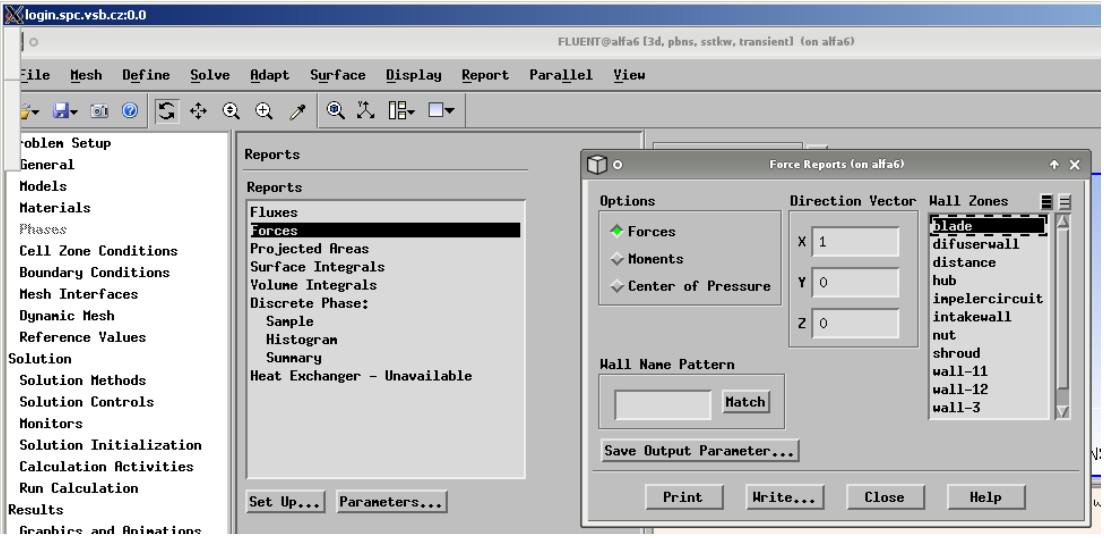

Options: Forces

Direction Vector: X 1, Y 0, Z 0

Wall Zones: blade

Figure 48 Function Force Reports in Fluent

With the results of modelling, radial force F_r can be calculated:

$$F_r = \sqrt{F_y^2 + F_z^2} \tag{55}$$

The radial force obtained from modelling is shown in Table 8:

Table 8 Radial forces loads on blade

Q	Q	F_y	F_z	F_r
[1]	[dm^3.s^{-1}]	[N]	[N]	[N]
0.01	0.10	-496.88	-22.28	497.38*
0.04	0.30	-466.40	7.27	466.46*
0.07	0.50	-445.02	6.91	445.08*
0.14	1.00	-424.13	13.12	424.33*
0.21	1.50	-397.18	13.53	397.41*
0.29	2.00	-374.21	22.39	374.88*
0.43	3.00	-333.75	5.01	333.79*
0.57	4.00	-284.42	4.18	284.45*
0.71	5.00	-215.68	15.18	216.22*
0.86	6.00	-137.87	10.87	138.30*

1.00	7.00	-69.39	28.35	74.96*
1.29	9.00	130.31	52.77	140.58**
1.57	11.00	333.25	98.08	347.38**
1.86	13.00	267.73	121.42	293.98**
2.00	14.00	269.60	167.35	317.32**

* average value in 0.009 [s] (two fifth shaft revolution)

** Value at time 0.54 [s]

The value and direction of radial forces change with the different flow rate. The radial force is shown on plane (*y,z*). With $Q < Q_o$, the radial force is act upon diffuser, with $Q > Q_o$, the radial force is back again. The radial force is smallest with $Q = Q_o$

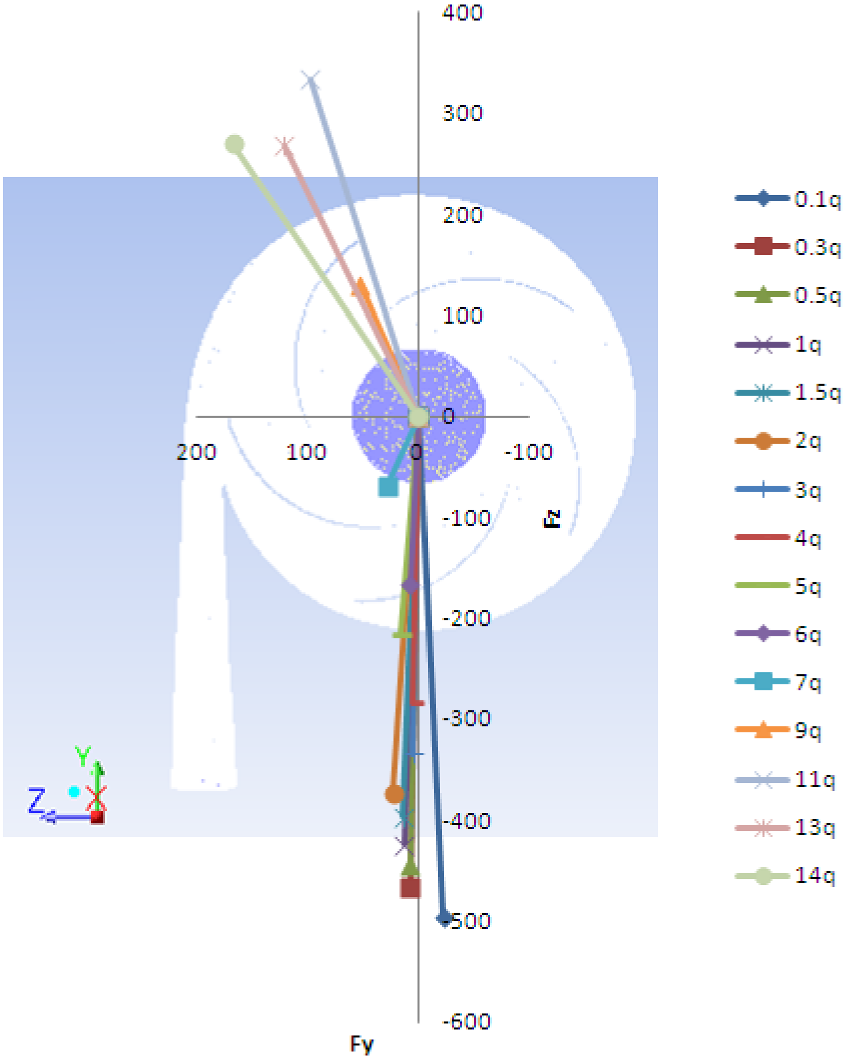

Figure 49 Layout of radial force [N]

0.1q	stands Flow rate = 0.1 $dm^3.s^{-1}$
0.3q	stands Flow rate = 0.3 $dm^3.s^{-1}$
0.5q	stands Flow rate = 0.5 $dm^3.s^{-1}$

1q	stands Flow rate = 1	$dm^3.s^{-1}$
1.5q	stands Flow rate = 1.5	$dm^3.s^{-1}$
2q	stands Flow rate = 2	$dm^3.s^{-1}$
3q	stands Flow rate = 3	$dm^3.s^{-1}$
4q	stands Flow rate = 4	$dm^3.s^{-1}$
5q	stands Flow rate = 5	$dm^3.s^{-1}$
6q	stands Flow rate = 6	$dm^3.s^{-1}$
7q	stands Flow rate = 7	$dm^3.s^{-1}$ this is $Q = Q_o$
9q	stands Flow rate = 9	$dm^3.s^{-1}$
11q	stands Flow rate = 11	$dm^3.s^{-1}$
13q	stands Flow rate = 13	$dm^3.s^{-1}$
14q	stands Flow rate = 14	$dm^3.s^{-1}$

7.3. Comparison with empirical formulas

The comparison of results with the mathematical model has the empirical formula is needed. Based on the empirical formula has been published by authors such as: Stepanoff (1957), Biheller (1965), Agostinelli (1960), Mackay and KBS Pumps company.

- **Stepanoff** [38]

$$F_0 = K\,H\,D_2\,b_2' \qquad K = 0.36\left[1-\left(\frac{Q}{Q_n}\right)^2\right] \tag{56}$$

where

H	head,	[m]
D_2	outside impeller diameter,	[m]
b'_2	impeller width including shrouds,	[mm]
K	thrust constant	[1]
F_0	radial force,	[kg]

- **Biheller** [38]

$$F_0 = 0.1511 u_2^2\, A_j\, \rho 10^{-\left(1.13\frac{\Delta A}{A}\right)} \sqrt{1+\left(\frac{Q}{Q_n}\right)^2 - 2\left(\frac{Q}{Q_n}\right)\cos\left(\frac{\pi}{2}\left(\frac{Q}{Q_n}-1\right)\right)} \tag{57}$$

where

ρ	specific mass,	[$kg.sec^2.m^{-4}$]
A_j	total impeller project area ($A_j = b_2 d_2$),	[m^2]
F_0	radial force,	[kg]

- **Agostinelli** [19]

$$F_r = k\,K_r\,(sp.gr.)\,H\,D_2\,b_2 \tag{58}$$

where

sp.gr.	specific gravity of the liquid pumped (equal to unity for cold water)	
k	9790 (SI)	
K_r	experimentally determined coefficient	
H	pump head,	[m]
b_2	impeller width at discharge including shrouds,	[m]
D_2	outside diameter of impeller,	[m]
F_r	radial thrust,	[N]

Values of K_r is determined in Figure 50

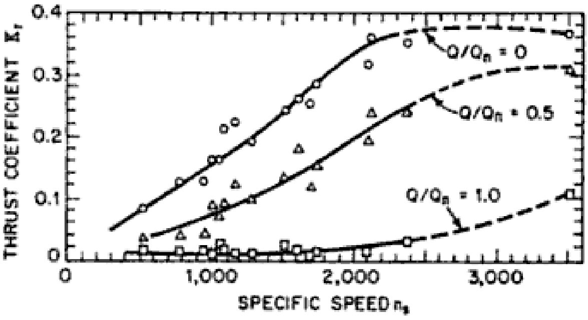

Figure 50 K_r as function of specific speed and flow rate for single-volute pumps [19]

- **Mackay** [23]

$$F_r = F_{SO}\left[1-\left(\frac{Q}{Q_o}\right)^x\right] \tag{59}$$

$$F_{SO} = K_{SO} P_{SO} D B$$

where

K_{SO}	radial thrust factor that can be established from the impeller design and tends to vary between 0.15 and 0.38 depending on design and its specific speed.
P_{SO}	differential pressure at shutoff, [psi]
D	impeller diameter, [in]
B	impeller with at perimeter including shrouds, [in]
x	exponent, may be assumed to vary linearly between 0.7 at an impeller specific speed 500 and a value of 3.3 at impeller specific speed of 3500
F	radial force, [pounds]

- **KBS Pumps** [31]

$$F_R = \kappa\,\rho\,H\,D_2\,b_2 \tag{60}$$

where

K	radial thrust factor	[1]

ρ	density of pumped liquid,	[kg.m^{-3}]
g	gravity,	[m.s^{-2}]
H	head,	[m]
D_2	impeller diameter,	[m]
b_2	impeller width,	[m]
F_R	radial force,	[N]

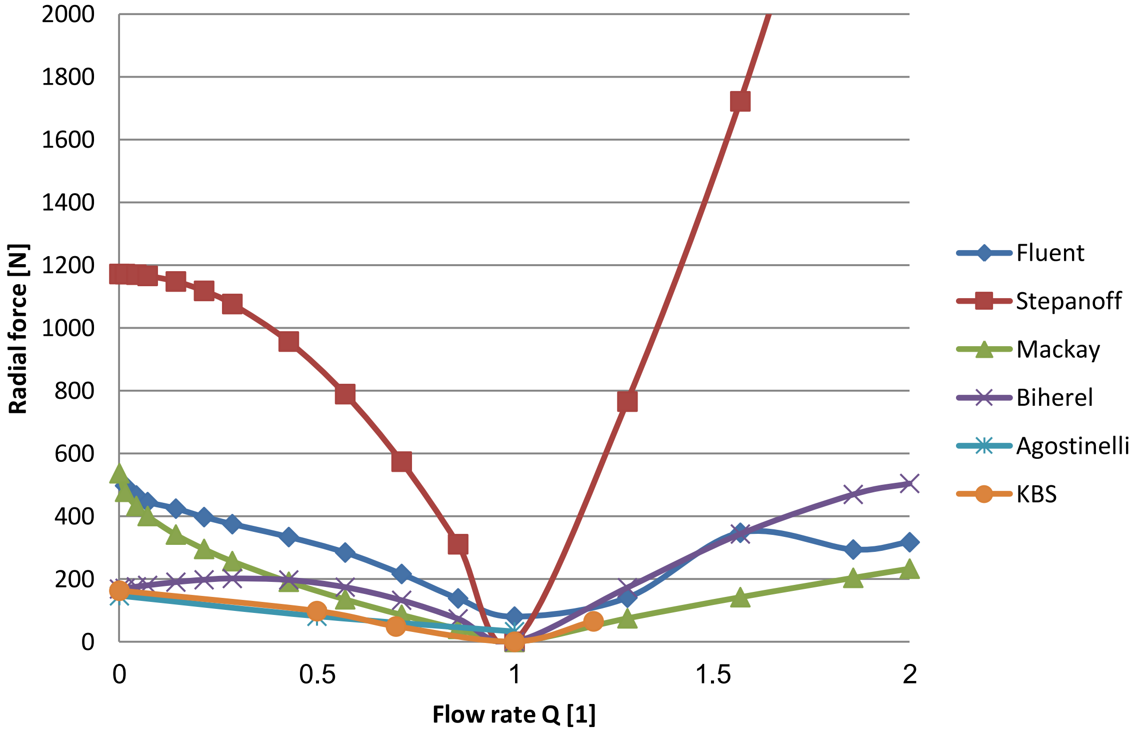

Figure 51 Comparison of radial force obtained by numerical modelling with result obtained from empirical formulas

Results of numerical modelling were compared with values obtained from empirical formulas. The results are close to those predicted by Biheller and Mackay. Stepanoff's equation gives higher values then others, but this can contribute to the safety of the shaft design. The most adequate is Biheller's equation for calculation of static component of the radial forces.

The benefit of numerical modelling is shown the value and direction of the (total) radial forces.

8. Axial force

Axial force of pump is result from hydrodynamic loading on all wetted surfaces of the impeller. The net thrust can be minimized by carefully optimizing pressure distributions within the rotor side gaps.

8.1. Introduction

For reasons of mechanical design, axial clearances are required between the shrouds of a closed impeller and the casing (impeller sidewall gaps). Width and shape of the resulting liquid-filled spaces between impeller and casing are essentially determined by aspects of the mechanical design. The fluid contained in the impeller sidewall gaps cannot be at rest when the impeller rotates: immediately at the shroud the fluid adheres to the solid wall and has thus the velocity $c_u = \omega \times r$. A boundary layer is formed in which the tangential velocity drops with increasing distance from the shroud. The fluid also adheres to the casing wall where the velocity is zero $c_u = 0$. The velocity increases in the casing wall boundary layer, Figure 52.

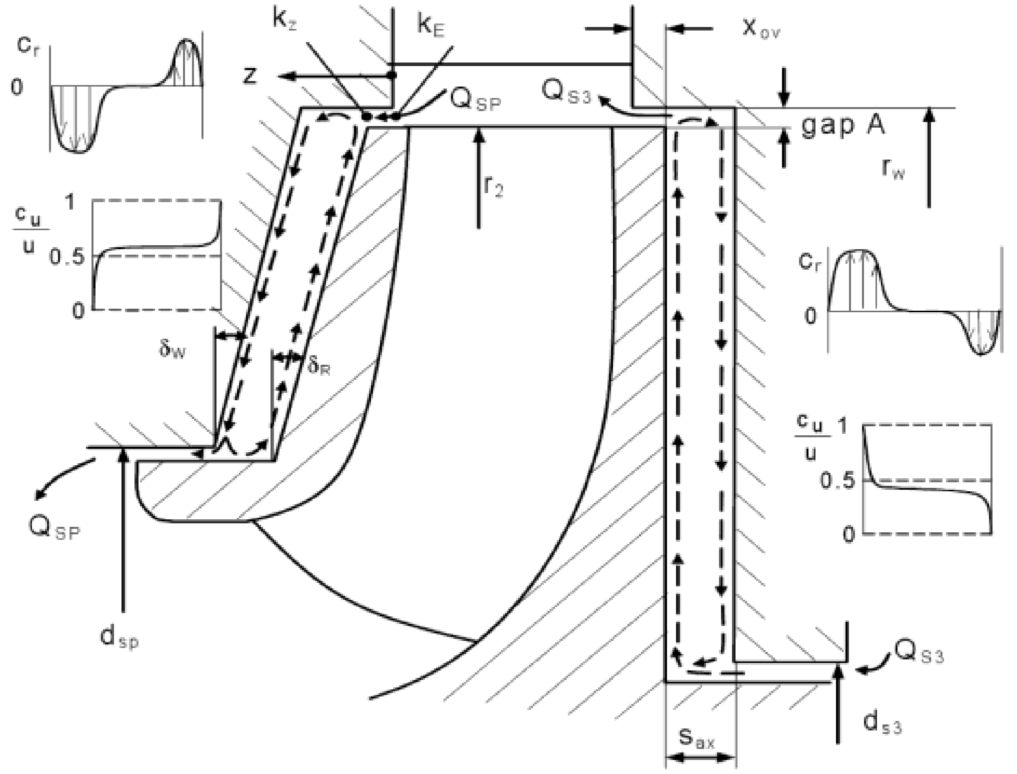

Figure 52 Velocity distribution in the impeller side gaps [18]

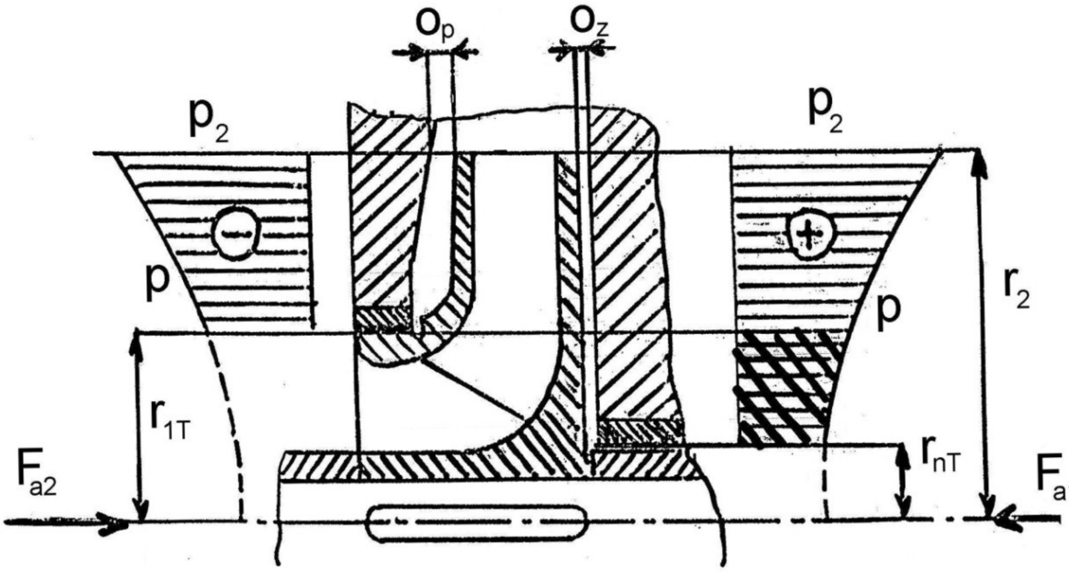

Figure 53 Pressure distribution and axial forces on impeller of a single-stage pump [34]

8.2. The theory of single-stage centrifugal pumps axial forces

The calculation of axial thrust can be carried out according to the following procedure. However it is based on ideal assumptions and is accompanied with many uncertainties. The resultant force comprises the forces F_{a2} and F_{a2}, as depicted in Figure 53. These forces result from the pressure distribution acting on the impeller shrouds. As a boundary condition for the calculation of pressure distribution the static pressure p_2 at the impeller outlet must be determined. It can be specified based on the energy transfer in the impeller described by Euler equation.

Based on equation of specific energy :

$$Y_t = u_2 \, c_{u2}$$

$$c_{u2} = \frac{Y_t}{u_2} = \frac{Y_s}{\eta_h \, u_2} \tag{61}$$

where

$$u_2 = \pi \, D_2 \, n \tag{62}$$

in velocity triangle

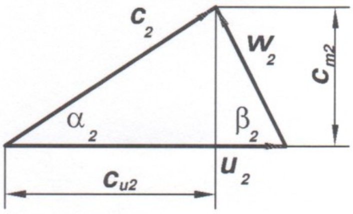

$$c_2 = \sqrt{c_{m_2}^2 + c_{u_2}^2}$$

$$c_{m_2}^2 = \frac{Q_{v_t}}{\pi D_2 b_2 \varphi_2} = \frac{Q_v}{\eta_o \pi D_2 b_2 \varphi_2} \tag{63}$$

$$Q_{v_t} = \frac{Q_v}{\eta_o} = (1.03 \div 1.05) Q_v$$

The outlet pressure p_2 from impeller is defined from the specific energy Y_s.

$$Y_s = \frac{p_2}{\rho} + \frac{c_2^2}{2}$$

$$\Rightarrow p_2 = \rho\left(Y_s - \frac{c_2^2}{2}\right) = \rho\left(Y_s - \frac{c_{m_2}^2 + c_{u_2}^2}{2}\right) \tag{64}$$

In the gaps between the impeller and the stator wall, the fluid gets into the rotation due to friction with the outer side of the impeller. Assume the friction is the same on the stator surface, on the impeller.

The fluid rotates with a half of angular speed: $\omega_k = \frac{\omega}{2}$

The fluid cause a pressure as parabolic with height

$$H_p = \frac{(r\,\omega)^2}{2g} \tag{65}$$

Pressure at point 2 (Figure 54):

$$H_2 = \frac{p_2}{\rho g} \tag{66}$$

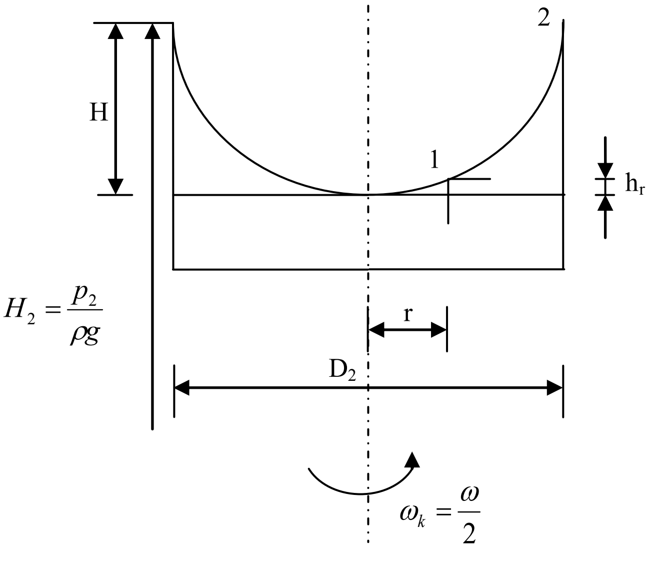

Figure 54 Distribution of pressure on rotating disk [2], [31]

Pressure at point 1 (Figure 54):

$$H_1 = \frac{p}{\rho g} \tag{67}$$

Then

$$\begin{aligned} \frac{p}{\rho g} &= \frac{p_2}{\rho g} - H + h_r \\ p &= p_2 - \rho g (H - h_r) \\ &= p_2 - \rho g \left(\frac{D_2^2 \omega^2}{32 g} - \frac{r \omega^2}{8 g} \right) \\ &= p_2 - \frac{\rho \omega^2}{8} \left(\frac{D_2^2}{4} - r^2 \right) \end{aligned} \tag{68}$$

Put

$$\begin{aligned} a_1 &= \frac{\rho \omega^2}{8} \\ a_2 &= \frac{D_2^2}{4} = R_2^2 \end{aligned} \tag{69}$$

We have

$$p = p_2 - a_1 (a_2 - r^2) \tag{70}$$

In ideal case, the force generated by pressure on front surface and back side of the suction disk can be calculated by interval from radius r_2 to r_{1T}. On back disk concepts pressure above atmospheric, which loads on distance r_{1T} and r_{nT} make reduce axial force, the force has direction to suction side of pump.

$$\begin{aligned} dF_a &= p\, dS = p\, 2\pi r\, dr \\ F_a &= 2\pi \int_{r_{nT}}^{r_{1T}} p\, r\, dr \\ &= 2\pi \int_{r_{nT}}^{r_{1T}} \left[p_2 - a_1 (a_2 - r^2) \right] r\, dr \\ &= 2\pi \left[\int_{r_{nT}}^{r_{1T}} (p_2 - a_1 a_2) r\, dr + \int_{r_{nT}}^{r_{1T}} a_1 r^3\, dr \right] \\ &= 2\pi \left[\frac{(p_2 - a_1 a_2) r^2}{2} + \frac{a_1 r^4}{4} \right]_{r_{nT}}^{r_{1T}} \\ &= \pi \left[(p_2 - a_1 a_2)(r_{1T}^2 - r_{nT}^2) + \frac{a_1}{2} (r_{1T}^4 - r_{nT}^4) \right] \\ &= \pi (r_{1T}^2 - r_{nT}^2) \left[(p_2 - a_1 a_2) + \frac{a_1}{2} (r_{1T}^4 + r_{nT}^4) \right] \end{aligned} \tag{71}$$

Because of equation (69) we have

$$\begin{aligned} F_a &= \pi\left(\mathrm{r}_{1\mathrm{T}}^2 - r_{nT}^2\right)\left[\left(p_2 - \frac{\rho\omega^2}{8}R_2^2\right) + \frac{\rho\omega^2}{16}\left(\mathrm{r}_{1\mathrm{T}}^2 + r_{nT}^2\right)\right] \\ &= \pi\left(\mathrm{r}_{1\mathrm{T}}^2 - r_{nT}^2\right)\left[p_2 - \frac{\rho\omega^2}{8}\left(R_2^2 - \frac{\mathrm{r}_{1\mathrm{T}}^2 + r_{nT}^2}{2}\right)\right] \end{aligned} \tag{72}$$

8.3. Numerical simulation

Because the the gaps between the impeller and pump casing are essential for the axial force determination, numerical modelling was applied on the new geometry accounting also for the pump stator. Three more parts were added to the geometry (back-plate, hub-leakage, shroud-leakage), then we have in total 6 volumes (back-plate, hub-leakage, shroud-leakage, inlet, impeller, and diffuser) with 12 interfaces [41]. The overview of the applied geometry for axial force prediction is illustrated in Table 9 ANSYS FLUENT 13.0 was applied for numerical modelling of flow through a pump.

Table 9 Three overviews of geometry for calculation of axial force

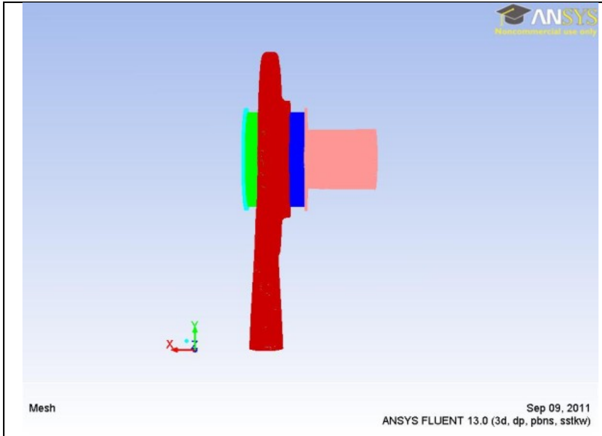	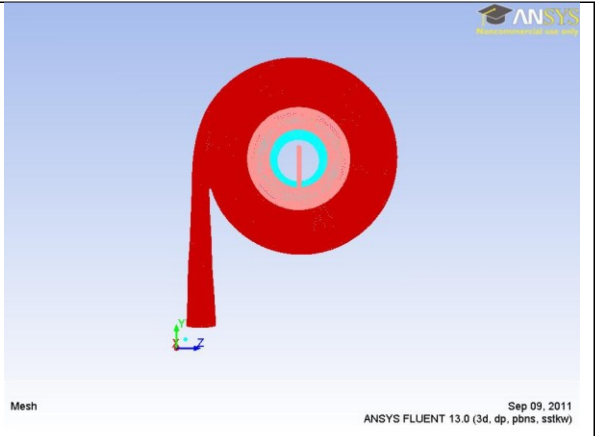
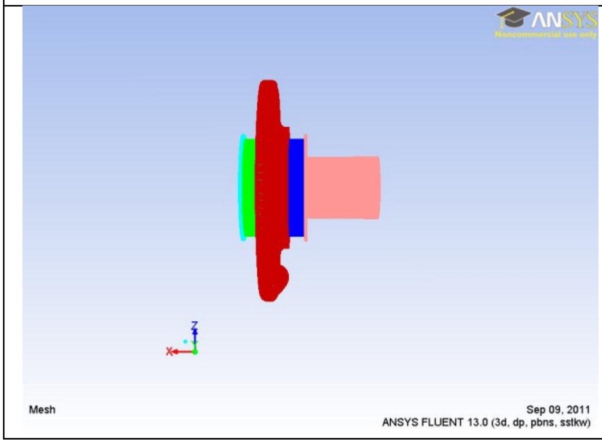	6 volumes (6 cell zones): inlet (pink), diffuser (red), back plate (cyan), hub leakage (green), shroud leakage (blue) and impeller 12 interfaces 4372347 cells 9668536 faces (55 face zones) 1252600 nodes 4 partitions

The computational parameters leading to the most reasonable result were as follows:

- 3d, double precision, pressure-based, SST *k-ω* solver.
- unsteady formulation: 1st Order Implicit
- time step: 0.0001 [s], max iteration per time step: 20.

All the simulation had to be run for long time. However the calculations were run for a long period, the calculated flow time in all tested cases was 0.06 [s] (three rounds of the impeller), which means “Number of Time Steps” was 600.

Near boundary (interface between impeller and volute), the grid had to be refined. The liquid flows from inlet, through all parts to outflow shown in Figure 55 below.

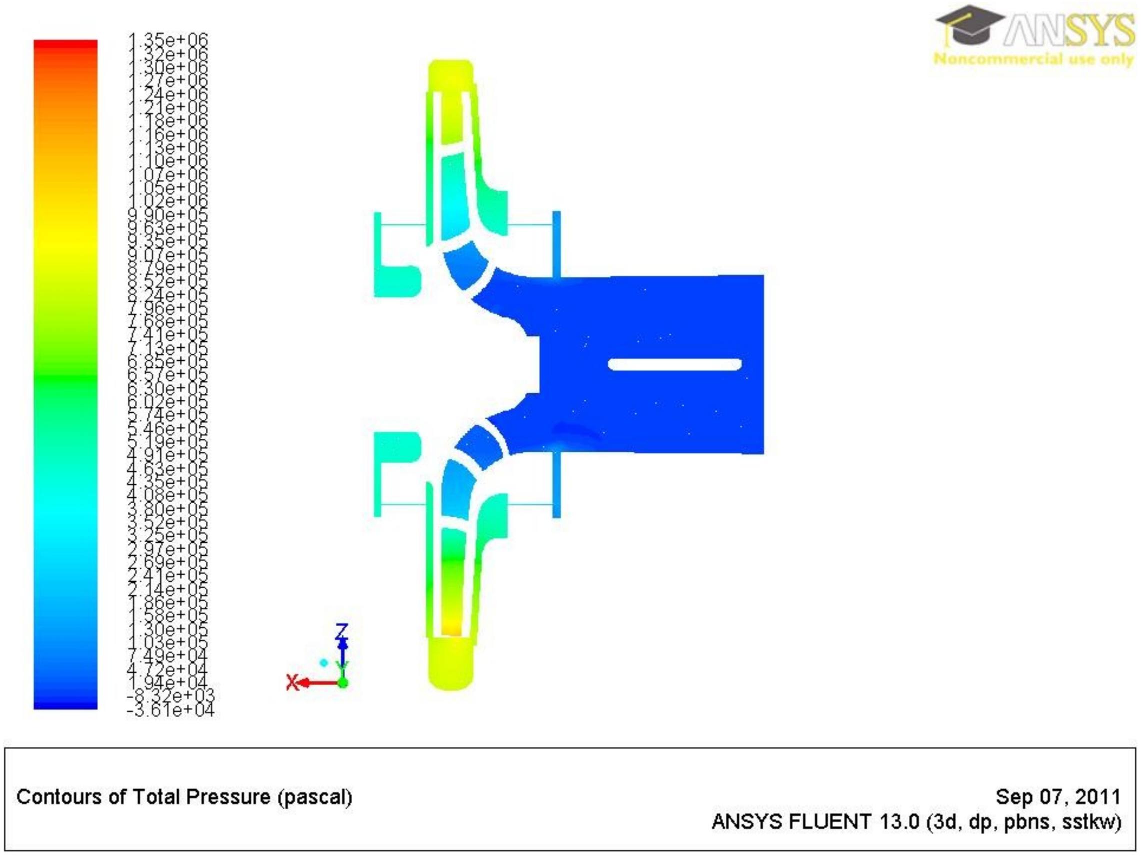

Figure 55 Overview of liquid in pump from inlet to outflow

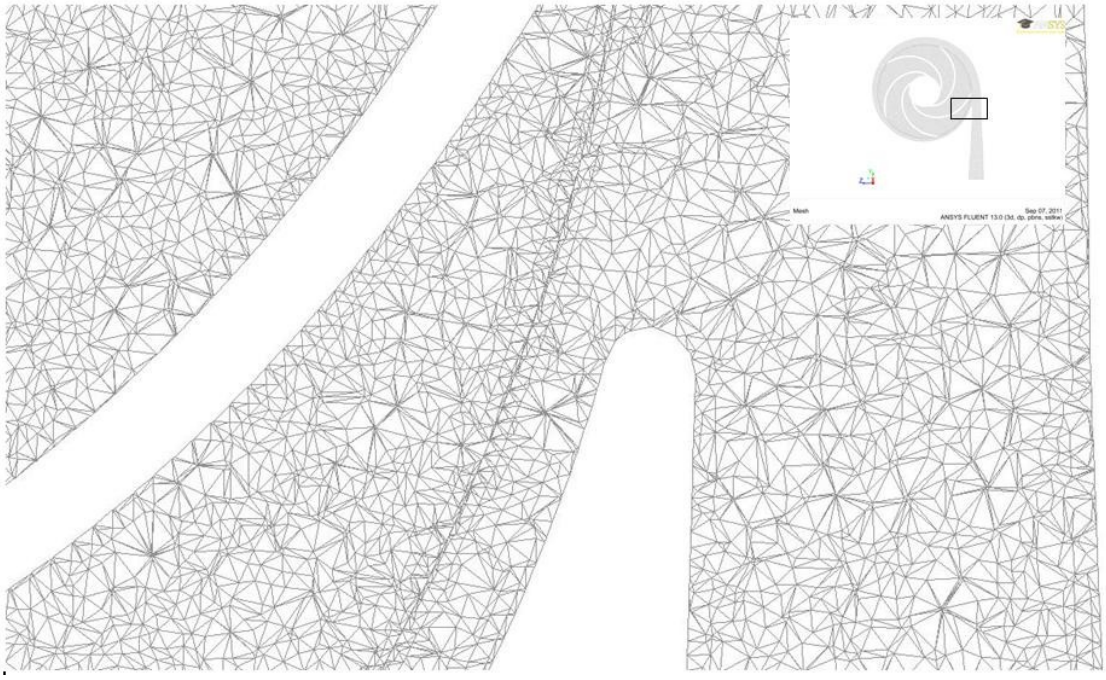

Figure 56 Detail of the computational grid

8.4. Results

In the case of steady solution, the precision of residuals was set to 10^{-5} for pressure and to 10^{-4} (x-velocity, y-velocity, z-velocity, k, and ω). The number of iterations reached 22000 in case $Q = Q_0$, The number of iteration was significantly lower for the flow rates above the Q_0, i.e. 9, 10, and 11 [dm^3.s^{-1}]. On the contrary, it was difficult to obtain converged solution for low values of the flow rate.

The convergence of the solution was controlled through the axial force monitoring. It can be observed that the axial force is increasing with number of iteration but after about 20000 of iterations it remains constant.

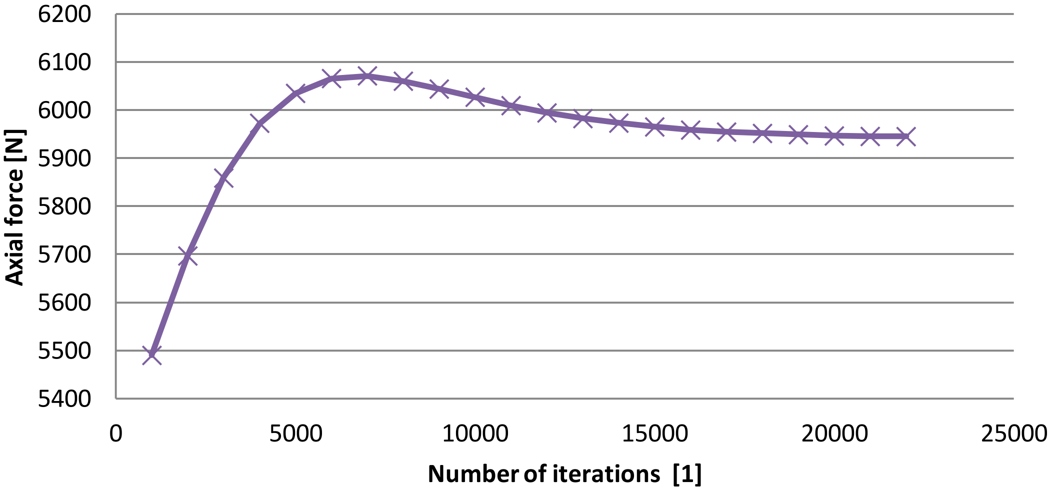

Figure 57 Axial force in steady case, $Q = Q_o$

Table 10 Axial forces load on impeller (steady case)

Number of iterations to reach convergence	Flow-rate [dm^3.s^{-1}]	Flow-rate [1]	Axial forces [N] load on			
			back-plate	hub	shroud	total
4000	1	0.143	-4726.20	-19954.26	18638.12	-6042.34
4000	2	0.286	-4623.79	-19620.19	18170.42	-6073.56
4000	3	0.429	-4518.64	-19258.04	17744.05	-6032.63
4000	4	0.571	-4432.12	-18964.29	17436.87	-5959.53
4000	5	0.714	-4357.29	-18698.70	17113.79	-5942.19
4000	6	0.857	-4311.17	-18534.01	16886.92	-5958.26
22000	7	1.000	-4279.57	-18421.35	16756.03	-5944.89
4000	8	1.143	-4251.85	-18319.23	16685.14	-5885.94
1489	9	1.286	-4384.02	-18624.57	17230.72	-5777.87

2092	10	1.429	-4328.43	-18441.02	16977.58	-5791.88
1000	11	1.571	-4378.10	-18496.46	17165.38	-5709.18

The result of total axial force from Table 10 is compared with other results obtained with empirical formulas in Figure 66.

The positive value of x direction is shown in the Figure 58. The axial force is acting in the opposite direction and has negative value.

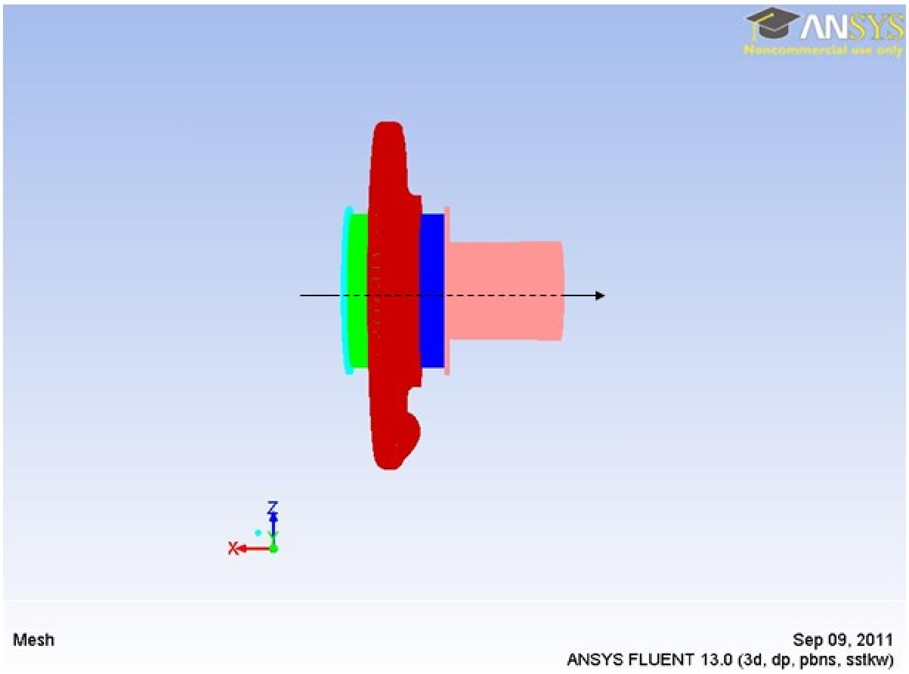

Figure 58 Direction with positive value of axial forces

Time dependent solution was carried out for the similar values of the flow-rate to obtain comparison with the steady prediction. Time step was constant and set to 0.0001 [s], “Max Iteration/Time Step” was 20 for all values of the flow-rate (from 1 $dm^3.s^{-1}$ to 11 $dm^3.s^{-1}$). “Number of Time Steps” reached 2000 in case $Q = Q_{o.}$

During the one shaft revolution the oscillation of the axial force can be observed, corresponding to the pressure oscillations (see Figure 59).

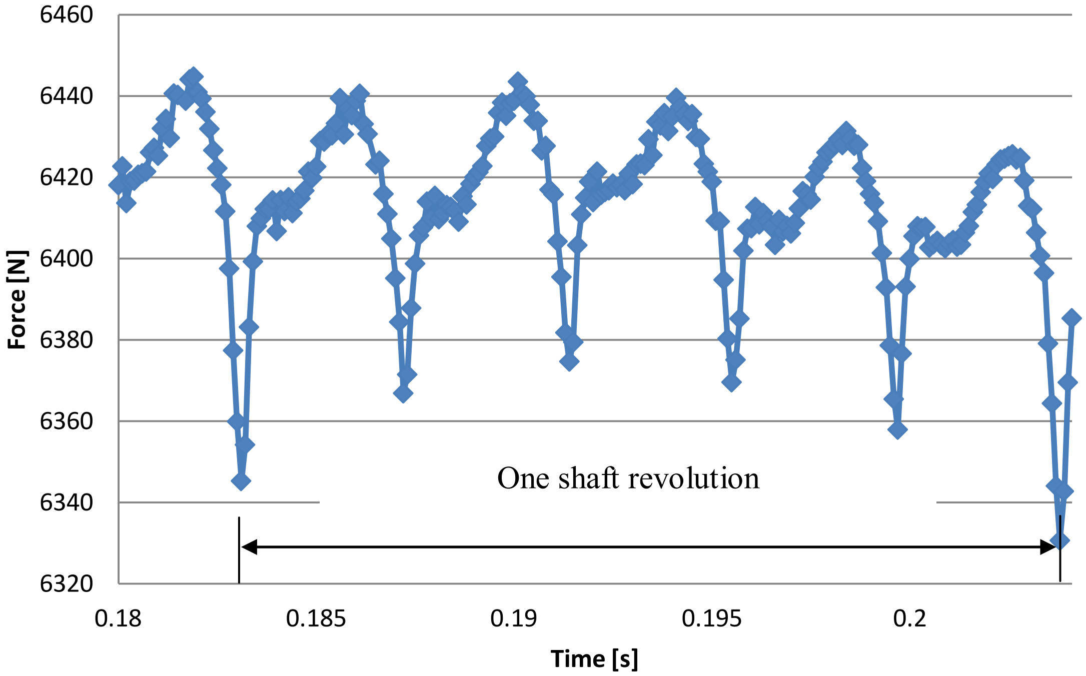

Figure 59 Axial force in unsteady case, $Q = Q_o = 7\ dm^3.s^{-1}$

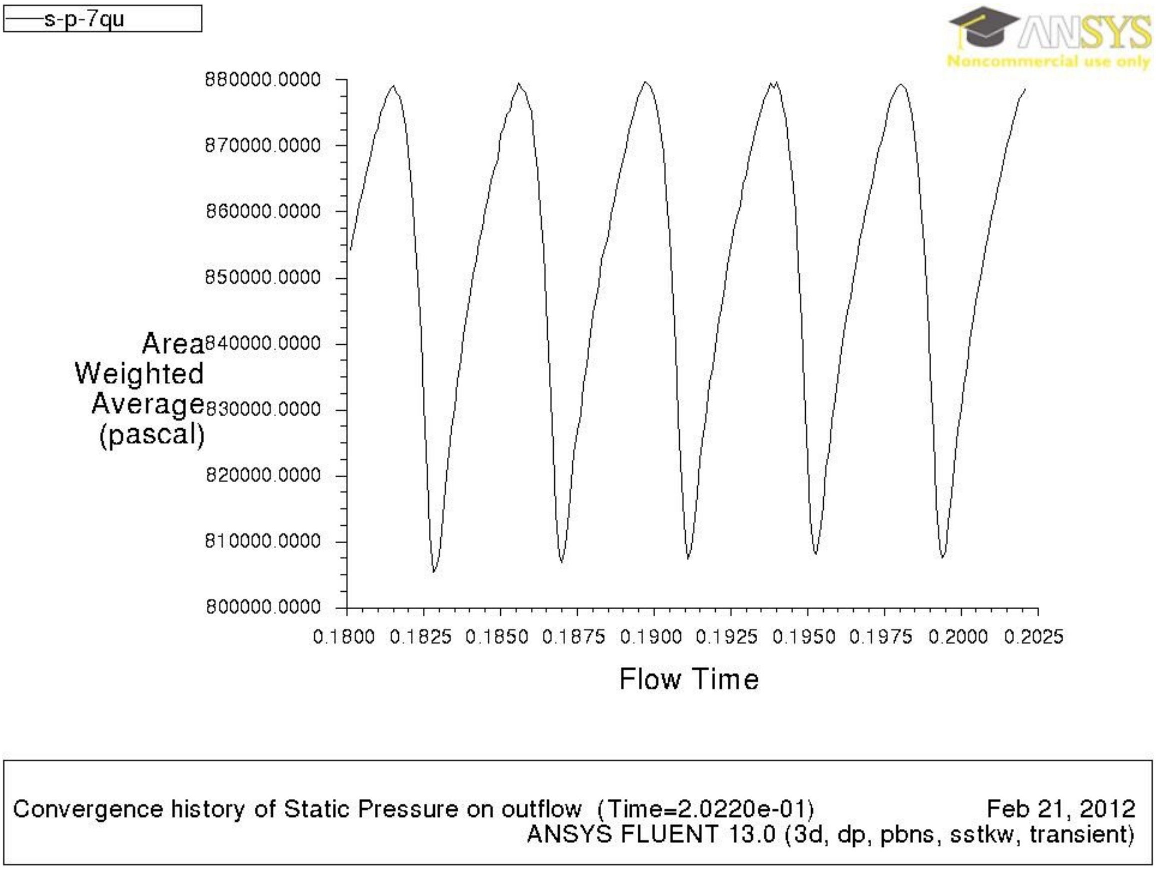

Figure 60 Static Pressure on outflow in case unsteady, $Q = Q_o$

From Figure 59 and Figure 60, we can derive the time difference for maximum and minimum of axial force and static pressure, which is presented in Table 11 and Figure 61 below.

Table 11 Difference time between max and min of axial force and static pressure

Time	Difference time	Max axial force (absolute value)	Max static pressure	Min axial force (absolute value)	Min static pressure
[s]	[s]	[N]	[Pa]	[N]	[Pa]
0.2022	0.0004		879057.1		
0.2026		6425.633			
0.2035	0.0003				805470.9
0.2038				6330.63	

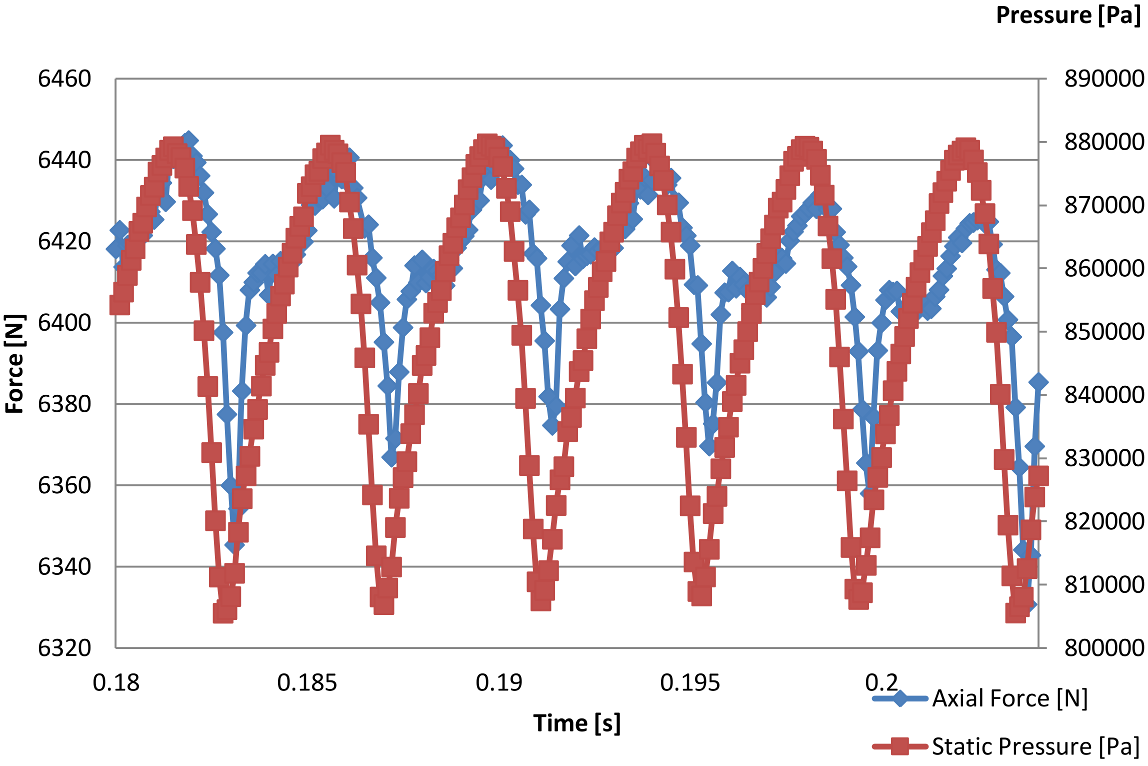

Figure 61 Axial force on impeller and static pressure at outflow in case $Q = Q_o$

The position of blades in case of axial force and static pressure maximum and minimum is presented in Figure 62 to Figure 65.

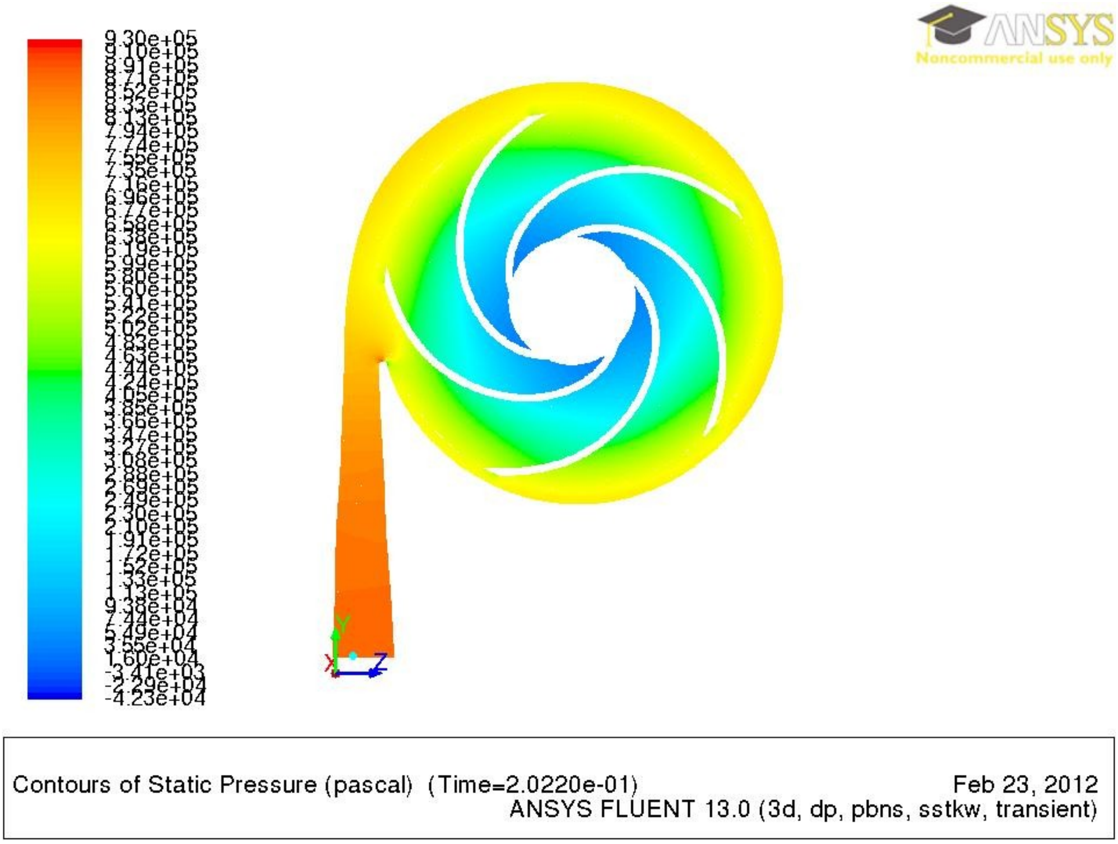

Figure 62 The position of blades in case of maximal static pressure at outflow

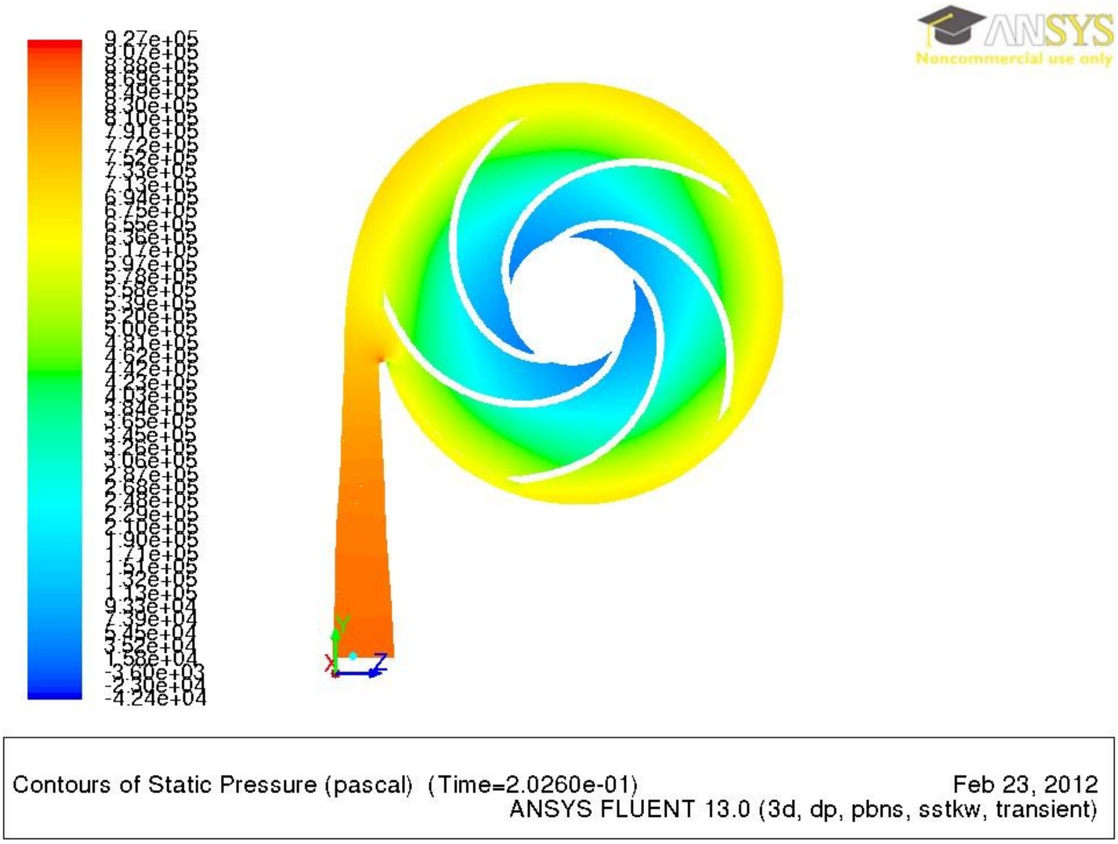

Figure 63 The position of blades in case of maximal axial force

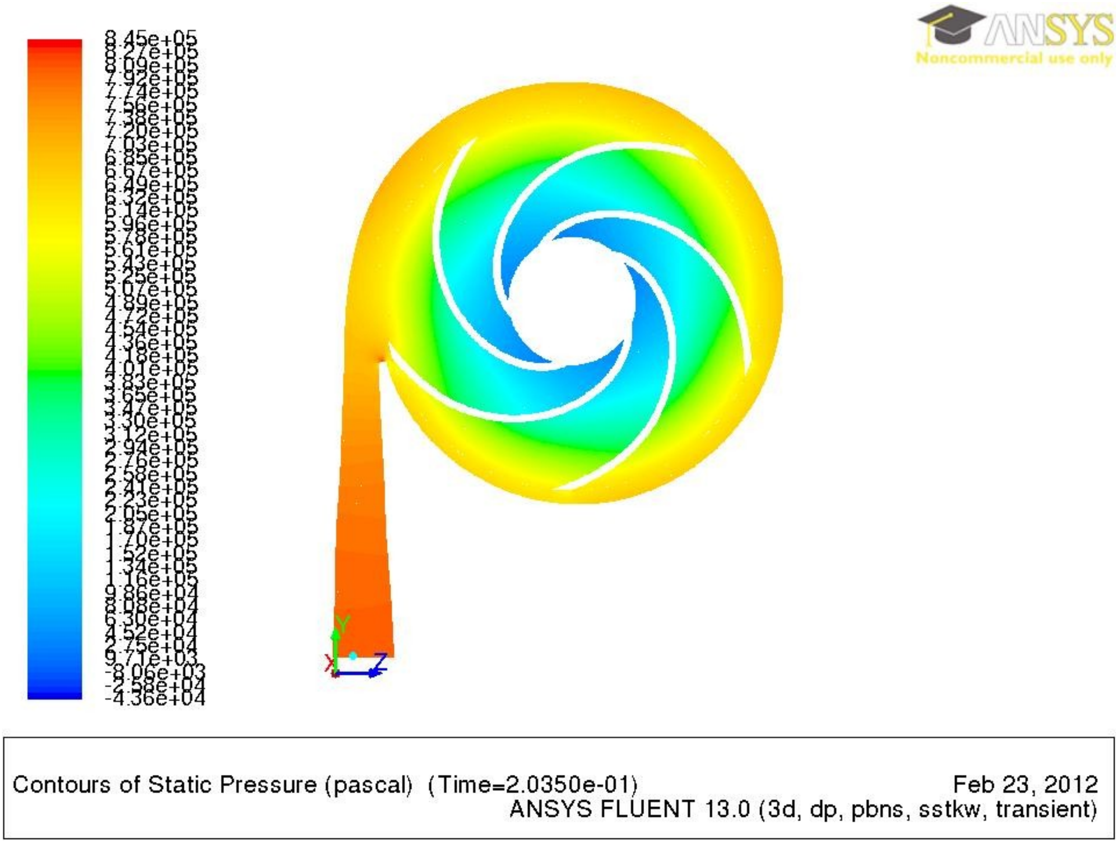

Figure 64 The position of blades in case of minimal static pressure at outflow

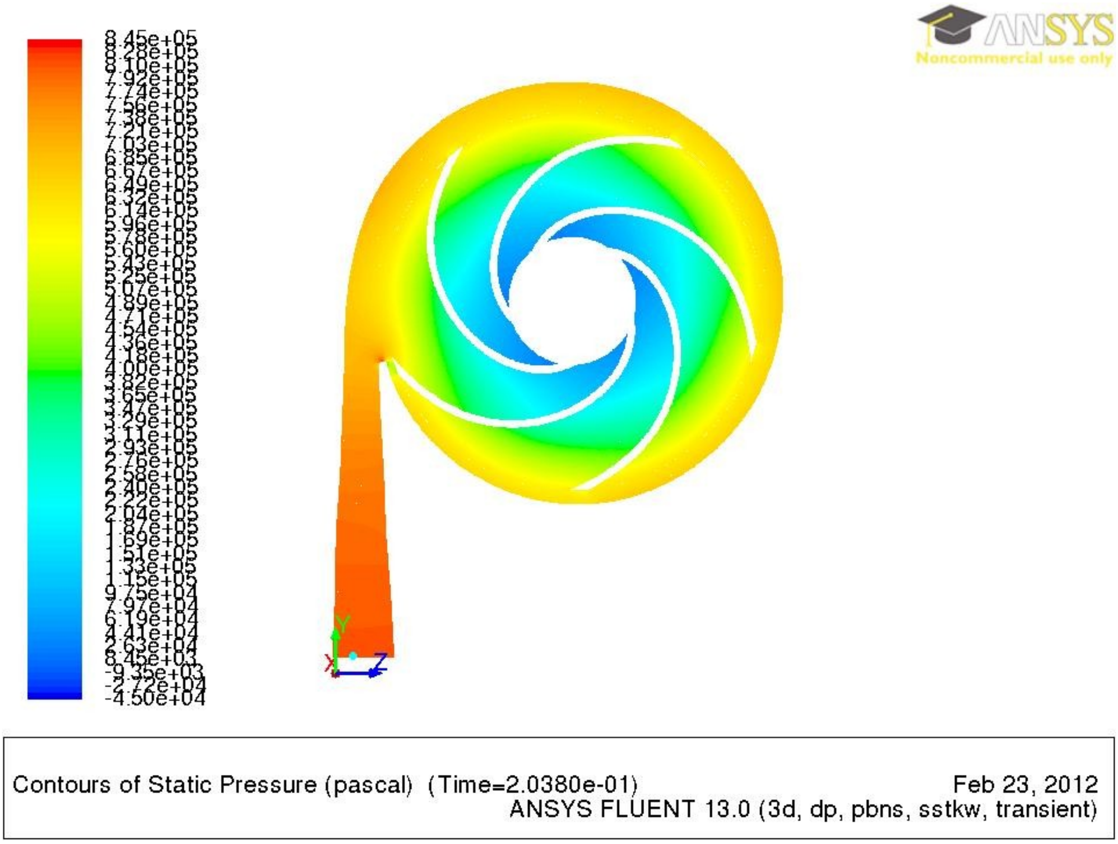

Figure 65 The position of blades in case of minimum axial force

Table 12 Axial forces load on impeller (case unsteady – average value)

Time Step Size [s]	Flow-rate [$dm^3.s^{-1}$]	Flow-rate [1]	Axial forces [N] load on			
			back plate	hub	shroud	total
0.0001	1	0.143	-4929.571	-19915.87	18223.1	-7060.578
0.0001	2	0.286	-5770.662	-22150.52	20983.7	-6937.487
0.0001	3	0.429	-5644.578	-21682.20	20532.3	-6794.497
0.0001	4	0.571	-5405.557	-21129.25	19799.3	-6735.473
0.0001	5	0.714	-5397.828	-20847.27	19747.9	-6497.235
0.0001	6	0.857	-5303.813	-20491.29	19388.6	-6406.545
0.0001	7	1.000	-5228.7295	-20225.264	19107.476	-6346.517*
0.0001	7	1.000	-4593.584	-19433.68	17516.5	-6511.886**
0.0001	8	1.143	-5181.381	-20027.77	18861.0	-6348.127
0.0001	9	1.286	-5069.457	-19721.07	18569.2	-6221.318
0.0001	10	1.429	-5047.584	-19605.42	18376.4	-6276.621
0.0001	11	1.571	-5005.907	-19500.56	18269.3	-6240.849

* In this case $Q = Q_o$= 7 $dm^3.s^{-1}$, this value is average value from 0.001 [s] to 0.06 [s]

** In this case $Q = Q_o$= 7 $dm^3.s^{-1}$, this value is average value from 0.001 [s] to 0.2 [s]

The result of total axial force from Table 12 is compared with other results obtained with empirical formulas in Figure 66.

8.5. Comparison with empirical formulas

The comparison of results with the mathematical model has the empirical formula is needed. Based on the empirical formula has been published by authors such as: Oldřich Strýček (1994), Johann Friedrich Gülich (1999) [18].

- **Oldřich Strýček** [35]

$$F_a = \pi \rho \left(r_1'^2 - r_n^2 \right) \left[0.97Y - \left(r_2^2 - \frac{r_1'^2 + r_n^2}{2} \right) \frac{\omega^2}{8} \right] \tag{73}$$

where

r_n	shaft radius
r'_1	radius at inlet of impeller
r_2	radius at outlet of impeller
ω	angular velocity
Y	specific energy

- **Johann Friedrich Gülich** [18]

$$F_{Hy} = \frac{\pi}{4}\left(d_{sp}^2 - d_D^2\right)\left[\Delta p_{La} - \frac{\rho}{2}\bar{k}^2 u_2^2\left(1 - \frac{d_{sp}^2 - d_D^2}{2d_2^2}\right)\right] \tag{74}$$

$$\Delta p_{La} = p_2 - p_1$$

where

$\bar{k}$	average rotation factor from the measurement of a pressure difference in the impeller side-wall gaps (for this impeller, calculate and choice is 0.7)
d_D	diameter at shaft seal
d_{sp}	seal diameter (Figure 52)
Δp_{La}	the average pressure difference
d_2	diameter at outlet
u_2	impeller peripheral velocity (at outlet of impeller)

Table 13 Comparison axial forces

Flow-rate	Flow-rate	Strýček	Gülich	Fluent Steady (absolute value)	Unsteady (absolute value)
[dm^3.s^{-1}]	[1]	[N]	[N]	[N]	[N]
1	0.14	4585.848	5429.01	6042.337	7060.578
2	0.29	4608.775	5362.423	6073.559	6937.487
3	0.43	4596.115	5301.452	6032.631	6794.497
4	0.57	4567.935	5270.868	5959.533	6735.473
5	0.71	4540.977	5202.149	5942.194	6497.235
6	0.86	4509.884	5133.357	5958.257	6406.5448
7	1	4461.815	5052.398	5944.89	6346.517*
8	1.14	4399.377	4983.089	5885.937	6348.127
9	1.29	4128.439	4896.058	5777.87	6221.318
10	1.43	4149.329	4784.858	5791.878	6276.621
11	1.57	3933.615	4690.28	5709.181	6240.849

* In this case $Q = Q_o$= 7 dm^3.s^{-1}, this value is average from 0.001 [s] to 0.06 [s]

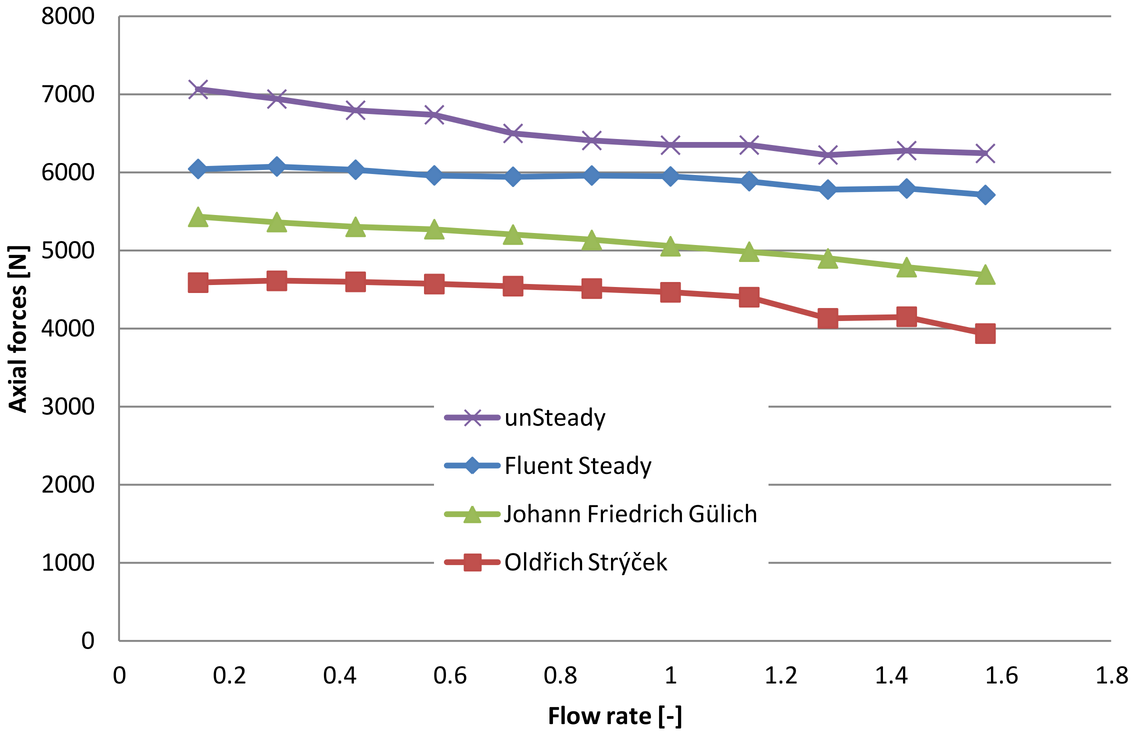

Figure 66 Comparison of results obtained by numerical modelling with result obtained from empirical formulas

The results obtained by numerical modelling were compared with those calculated with empirical formulas. For unsteady case the data were obtained as average value from 0.001 [s] to 0.06 [s].

At the pumps of low specific speed, the empirical formulas gave lower values of axial thrust, while the numerical simulation predicted higher values. The unsteady solution requires long time for calculation but gave time dependent results for all calculate cases.

To reduce axial force, the balance pistons, the stepped piston, back-to-back design, or closed ring can be used [18], [39].

Balance pistons generate a force opposing the axial thrust. As an approximation, the force created by the piston and the pressure created by the piston can be calculated from the area of the piston and the pressure at the entrance to the piston.

Stepped balance piston: with this design it is attempted to benefit from the advantages of the balance disks without incurring the disadvantage of the piston.

Back-to-back design: the axial thrust of multistage, double-entry pumps is almost perfectly balanced without any sacrifice in efficiency.

Closed impeller with rings on both sides, which is the case of this radial pump, use balancing holes in back shroud. Balance holes through the impeller allow liquid leaking across the wear ring clearance to flow back to the suction side of the impeller. Most often once balance hole is drilled in each impeller channel. The total area of all holes should be at least 4-5 times as big as the flow area in the annular seal clearance [18]. Balance holes increase the leakage losses and so can have negative influence on the efficiency.

8.6. Head and efficiency with new model

Using this new model with the stator (six_parts_simulation, other predicted values: moment, inlet pressure and outlet pressure, the efficiency) have been evaluated and compared with the old model (three_parts_simulation) in Chapter 6.

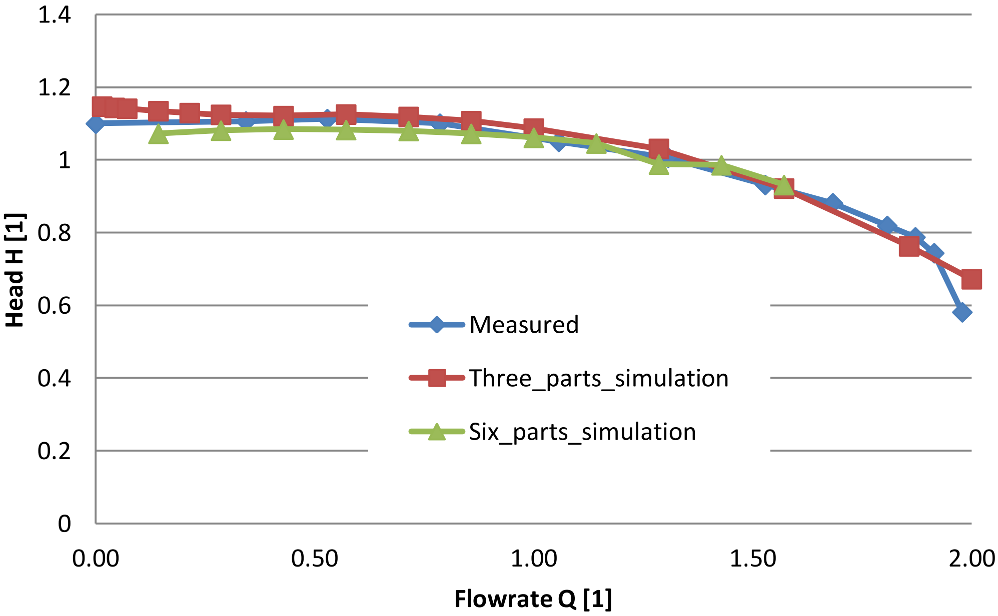

Figure 67 Comparison of *Q~H* curve

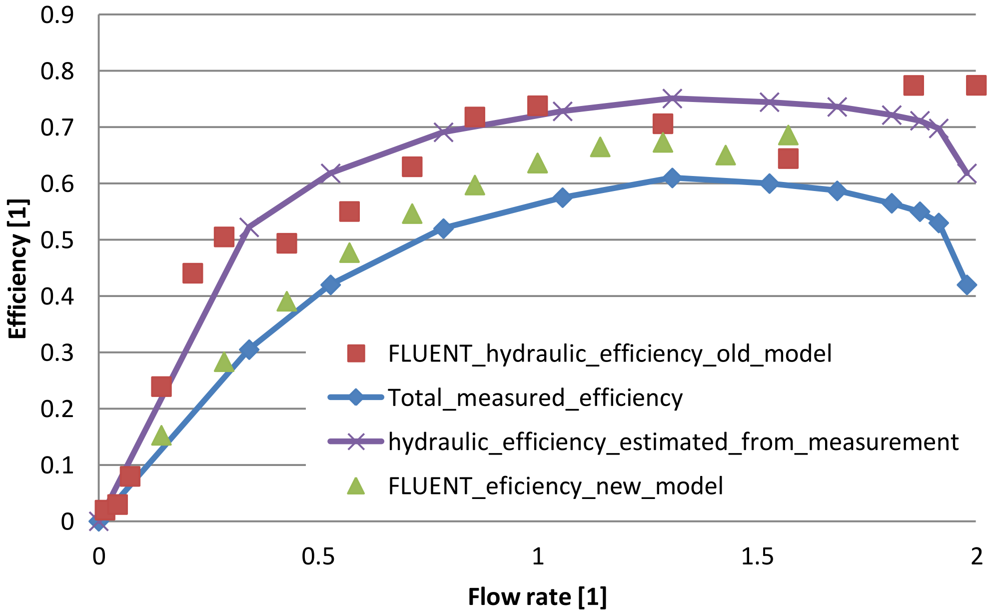

Figure 68 Comparison of efficiency

Both of models are not suitable to simulate the flow rate *Q* higher than 10 [$dm^3.s^{-1}$] or 1.42 [1] in non-dimensional form.

9. Conclusion

Analysis of the fluid flow inside operating area of the centrifugal pump is a difficult problem, and more difficult in case of the pump with low specific speed. This thesis deals with numerical modelling of flow inside the impeller from inlet through the volute to outlet. Based on real impeller designed at VUT-Brno, different geometry and meshes have been design in Gambit and then used for the calculations in Fluent.

The calculations used turbulence models k-ε and k-ω and two methods of rotor modelling: Moving Reference Frame and Moving Mesh. The method MRF provides only stationary solution of values, but the Moving Mesh approach shows time variation of them and enables to account for interaction of impeller and volute. Comparing with the experimental data and the other available numerical results, the current method is reliable enough to be utilized as a general approach to treat complex turbulent flow encountered in engineering.

This work had following objectives that are given in their time order:

- evaluation of different approaches to rotor-stator interaction modelling
- evaluation of the influence of computational grid quality
- determination of Q~H curve and its stability
- determination of Q~η curve
- prediction of the radial force in centrifugal pump
- prediction of the axial force in centrifugal pump
- comparison of experimental results with the results obtained with numerical simulation
- application of various methods of post processing (concerning efficiency)
- investigation of the mathematical model's restrictions.

Both steady and unsteady cases were modelled. Both approaches have their advantages as well as limitations. Using the steady solution based on Moving Reference Frame, average values of variables describing the flow in a pump can be obtained. This method allows obtaining quick estimation of pump parameters and in many practical cases it is sufficient. For unsteady solution we must record the result on one round or one fifth round, because the impeller has five blades. The simulation is time demanding and also more time for data processing is required. On the other hand the dynamic behaviour and interaction between the impeller and volute can be investigated.

Most of the calculation was performed on simplified geometry consisting only of three parts: intake, impeller and volute. Using this approach, performance curves can be evaluated with limitations. This concerns mainly the input and efficiency. In this case only hydraulic losses are included in the model, while volumetric and disk losses are not accounted for. Two different grids were tested, one consisting of 233 259 cells (non-conformal grid) and the second one with refined boundary layer with 802 555 cells (conformal grid). For both grids the calculated Q~H curves were nearly the same, but the head was over predicted for both grids when compared with measurement.

After adaption of the conformal mesh to 1 028 416 cells better agreement with experimental measurement was achieved.

One of the first objectives was to predict the stability of Q~H curve for the given pump. This objective is very difficult to reach. For low values of flow rate the calculation is accompanied with inaccuracy and in many cases it is not possible to obtain converged solution. The results are dependent on applied model of turbulence as well as the grid quality. From time dependent solution oscillation of parameters can be observed that reach maximum for values of flow rate converging to zero. It can be stated that in this case numerical modelling is not enough reliable to prove *Q~H* curve stability.

For the prediction of pump efficiency several approaches can be applied. Most common is evaluation of torque (moment) resulting from the forces acting on the rotor. This approach was applied both on reduced geometry consisting only of three main parts (intake, impeller and volute) as well as on geometry including also the pump casing. In the first case only hydraulic losses can be modelled, which results in prediction of hydraulic efficiency only. With pump casing, also volumetric losses and disc losses are accounted for, which increases the accuracy of efficiency prediction.

Within this work also another approach of efficiency prediction was tested which is based on the estimation of dissipation function. Fluent enables to evaluate the strain rate and to define dissipation function using the custom field function. The investigation was made for intake, impeller and volute and the dissipative output was determined in dependence on the flow rate. The observed trends in dissipative output variation on the flow rate correspond well to reality, but the calculated values are very low. In the definition of dissipation function dynamic (laminar) viscosity is accounted for, while the flow in a pump is turbulent. Turbulent viscosity is very important in such case, but its prediction depends on applied turbulent model. Beside this, also the grid quality is important, especially at the boundary layer.

In the case of radial force prediction numerical modelling can be applied as a tool with reasonable accuracy. While the radial forces can be determined using the simplified geometry (without pump casing), the axial forces are governed by the flow through the impeller sidewall gaps and thus require complex geometry definition. Results from unsteady numerical modelling show the oscillation of radial forces and enable to determine the mean load, magnitude and direction of these forces. Radial force is expected to reach its minimum in BEP. This was not confirmed by numerical modelling as minimal values of these forces were predicted behind BEP.

Axial force acting on the rotor was predicted from both steady and unsteady solution carried out on the complex geometry including the pump casing. The results obtained by numerical modelling were compared with those calculated with empirical formulas. The highest values were reached with unsteady solution. Steady solution predicted lower values, but in both cases the values were higher in comparison with results obtained with empirical formulas.

Empirical formulas are useful for determination of static component of the radial force and axial force. The value of dynamic load is higher and this fact must be accepted during the design of impeller shaft. Experimental and numerical approaches contributed to the understanding of the highly complex flow interaction that occurs in a centrifugal pump. Results from numerical modelling show the oscillation of these forces and enable to determine the mean load, magnitude and direction of these forces.

These forces are expected to reach its minimum in BEP. This was not confirmed by numerical modelling as the minimal values of these forces were predicted behind BEP. Further numerical experiments are required to increase the accuracy of these forces prediction. There are others questions which can be tested for example influence of computational grid and applied turbulence model.

The data obtained by numerical modelling were partly compared with results from measurement. From the measurement carried out by Sigma Lutín group *Q~H* curve, Q~*P* and *Q~eta* curve were available.

From the calculations it can be concluded that unsteady cases required long time calculation but gave more accurate results than steady solution. For the flow rates near BEP, the results are almost the same for both steady and unsteady solution, but at the point near zero and the point with higher flow-rate, the results of unsteady cases are in better agreement with experiment than the steady cases.

Limitations of pump efficiency were discussed in the above text. Using only the simplified geometry without casing, only hydraulic efficiency can be predicted and compared with experiment. Definition of complex geometry with pump casing enables to account also for the disk losses and volumetric losses. So in this case more accurate prediction of efficiency can be obtained. In both cases (simplified and complex geometry), the best agreement with experiment was reached near BEP, while for small flow rates and flow rates behind BEP the prediction was less accurate.

Beside the calculations, also the data post processing and evaluation becomes very important, especially in case of time dependent solution. Graphics tools available in FLUENT allow us to process the information contained in our CFD solution and easily view the results.

In FLUENT we can generate graphics displays showing grids, contours, profiles, vectors, and path lines. Some graphics are generated using variables that are plotted directly from the FLUENT data file once the file has been read. The variables listed in the data file depend on the models active at the time the file is written. Variables that are required by the solver, based on the current model settings, but are missing from the data file, are set to their default values. Tools are available for creating videos from FLUENT.

Post processing of time dependent simulation is more demanding than in case of steady solution. The calculated values of variables have to be saved in time for one shaft revolution or at least for one fifth shaft revolution. From the data series the oscillation of variables can be observed and the maximum, the minimum and the average value in time can be processed for comparisons or use for next calculation. In radial force evaluation also its direction becomes important besides its amplitude. That is why we need calculate the averaged quantity and averaged direction then show the average force acting on time period. The forces and momentum can be evaluated via monitoring.

Monitoring enables to save the convergence history of forces and momentum and to save the data in an external file for further processing. Beside this, the Data Sampling for Time Statistics option is available in Fluent which enables to compute the time average (mean) of the instantaneous values and root-mean-squares of the fluctuating values sampled during the calculation.

Development of computer technique and simulation software encourages to model complex fluid flow phenomena including the pump flow. This approach brings many benefits but also implies restrictions. Care must be taken from the beginning of the precise geometry definition and control of the grid quality. The number of computational cells is up till now the limiting factor, however it is possible to solve the grids consisting of millions cells. The pump geometry includes spacious channels as well as narrow gaps (sealing rings). This leads to problems in grid generation and transition from the very fine grid in gaps to the course grid in the main pump parts. Generation of boundary layers on blades contributes to extreme increase of number of cells.

Other limitations connected with the choice of the turbulence model. There is not any unique model suitable for pump flow. From the literature and experience the most recommended model for rotating flows is k-ω model of turbulence, but its application requires quite fine grid.

Nowadays the objective of pump designers is focused mainly on the Q~H curve stability and efficiency increase. The precision of numerical simulation often decreases in case of low flow rates and it is difficult to obtain converged solution. So the prediction of Q~H curve stability becomes problematic. Same conclusion can be done in case of efficiency. It can be stated that the best agreement with experimental data is reached in BEP, which was expected.

Beside all these restrictions, numerical modelling brings a deep insight into the pump flow and helps to evaluate pump characteristics and propose the improvements in hydraulic solution of the main pump parts.

10. References

[1] KROUZA V. *Čerpadla odstředivá a jim příbuzná*. Praha: Nakladatelství ČSAV, 1956.

[2] ALFÖLDI, C. *Návrh hydraulických tvarů odstředivé hospirálního čerpadla.* Brno: VUT Brno, FSI, Energetický ústav, Odbor fluidního inženýrství Victora Kaplana – disertační práce, 1998.

[3] ASWATHA, Narayana. P. A.; SEETHARAMU, K. N. *Engineering fluid mechanics.* Alpha Science: Harrow, U.K. 2005. 581p. ISBN 1-84265-101-3.

[4] BENEDIKTER, Simon. *Hydraulic engineering and strategic group formation in Vietnam and the Mekong Delta*<http://www.wisdom.caf.dlr.de/en/content/hydraulic-engineering-and-strategic-group-formation-vietnam-and-mekong-delta> January 2010

[5] BLÁHA, J.; BRADA, K. *Hydraulické stroje.* 1st edition Praha: SNTL, 1992. 747p. ISBN 80-03-00665-1.

[6] BLÁHA J. *Hydrodynamická čerpadla* ČVUT, Praha, 1985. 293p.

[7] BRADA, Karel; HLAVÍNEK, Petr. *Čerpadla ve vodním hospodářství.* Brno: NOEL 2000. 195p. ISBN 80-86020-43-6.

[8] BRENNEN, C. E. *Hydrodynamics of Pumps*, Cambridge 1994, 287p. ISBN 978-1-107-00237-1

[9] BRETTSCHNEIDER, A. and colleague. *Příručka čerpací techniky.* STNL, Praha, 1968.

[10] CASEY, M. Validation of Turbulence Models for Turbomachinery Flows – A Review. In *Proceedings of the 5th International Symposium on Engineering Turbulence Modelling and Measurements*, Mallorca, Spain, September 16 – 18, 2002. 1st ed. Oxford: Elsevier Science Ltd., 2002. ISBN 0-08-044114-9. s. 43–57.

[11] *Centrifugal pump design*. Technical appendix, KSB, Frakenthal, Germany.

[12] Fluent Inc. *Fluent 6.2.16 – User's guide* [online].c2005.

[13] Fluent Inc. *Gambit 2.2.30 – User's guide* [online].c2004.

[14] FOX, Robert W.; MCDONALD, Alan T.; PRITCHARD Philip J. *Introduction to FLUID MECHANICS*. 6th ed. John Wiley & Sons, Inc: USA, 2004. 787p. ISBN 978-0-471-20231-8.

[15] GOLHA M. *Hydraulický návrh a numerické modelovanie prúdenia v hydrodynamickom čerpadle*. 152p. Doctoral thesis, Department of Hydraulic machinery, Slovak University of Technology, Bratislava, 2005.

[16] HALLIDAY, D., RESNICK, R., WALKER, J. *Fyzika část 2 Mechanika-Termodynamika* Brno: VUT Brno, Nakladatelství VUTIUM, Nakladatelství PROMETHEUS 2000 ISBN 80-214-1868-0 (VUTIUM) ISBN 81-7196-213-9 (PROMETHEUS)

[17] JANALÍK, J. *Vybrané kapitoly z mechaniky tekutin*, VŠB-TU Ostrava, 2008. 180p<*http://www.338.vsb.cz/PDF/Janalik-Vybrane kapitoly z mechaniky tekutin.pdf>ISBN 978-80-248-1910-5.*

[18] JOHANN FRIEDRICH GÜLICH: *Centrifugal Pumps*, Second Edition, Springer, 2010 964p ISBN 978-3-642-12823-3.

[19] KARASSIK, I. J., MESSINA, J. P., COOPER, P., HEALD, CH. C. *Pump handbook third edition.* 1790p. U.S. 2001 ISBN 0-07-034032-3.

[20] KOZUBKOVÁ, M.; DRÁBKOVÁ, S. *Numerické modelování proudění – FLUENT I* [online]. c2003, version 20.4.2006 [cit.2006-04-20]. Available from: <http://www.338.vsb.cz/PDF/Kozubkova-Fluent.pdf>.

[21] LESIEUR, M.; YAGLOM, A.M.; David, F. *New Trends in Turbulence.* Les Houches: France, 2001. ISBN 3-540-42978-6.

[22] LIU, G.R.; TAN, V.B.C.; HAN, X. *Computational Methods* 2006. The Netherlands: Springer, 2006, 1002p. ISBN-10 1-4020-3952-2.

[23] MACKAY, R.:*Shaft Deflection Part One: The Cause.* 2004 Available from <http://www.pump-zone.com/articles/22.pdf>

[24] MELICHAR, Jan; BLÁHA, Jaroslav. *Problematika soudobé čerpací techniky.* Praha: ČVUT, 2007. ISBN 978-80-01-03719-5.

[25] NGUYỄN, H. H.; NGUYỄN, T. L.; TRƯƠNG, T. T.; LÊ, S. G.: *Studying the dynamic of the 3-d turbulent impinging jet.* Hanoi, 2001,

[26] NGUYỄN, T. Y. *Modelling tidal power turbines* 2010.

[27] NOSKIEVIČ, J. *Mechanika tekutin.* SNTL/ALFA. Praha: 1987. 354p.

[28] PACIGA, A.; STRÝČEK, O.; GANČO, M. *Čerpacia technika.* Bratislava: Alfa Bratislava – SNTL Praha, 1984, 224p, 63-557-84.

[29] PAVLUCH, L. *Porovnání některých metod řešení proudění v oběžných kolech odstředivých čerpade l*Strojírenství 17, 1967, číslo 13 strana 883-891.

[30] PHAM, V. T. *Some research results about the pump with small head*<http://www.ihr.org.vn/detail/mot-so-ket-qua-nghien-cuu-moi-ve-bom-cot-nuoc-thap.html> 2007.

[31] *Projektování čerpadel.* KSB pumpy&armaturys.r.o., 48p.

[32] RODI, W.; FUEYO, N. *Engineering turbulence modelling and experiments 5.* Elsevier, 2002.ISBN 0-08-044114-9.

[33] SLOUPENSKÝ, Z. *Návrh odstředivého čerpadla metodami diferenciální geometrie*, VUT-Brno 2009. 30p.

[34] Some hand written documents from k388 - Department of Hydrodynamics and Hydraulic Equipment , VŠB-TUO.

[35] STRÝČEK, Oldřich. *Hydrodynamické čerpadlá.* 2nd edition. STU, Bratislava, 1994. 297p. ISBN 80-227-0662-0.

[36] TÓTH, P. *Vplyv interakcie rotora a statora na radiálnu silu hydrodynamického čerpadla.* Doctoral thesis. 2000. Department of Hydraulic machinery. Slovak University of Technology, Bratislava. 103p.

[37] TUZSON John. *Centrifugal pump design.* 2000, 320p, ISBN 0-471-36100-3.

[38] UCHIDA, N., IMAICHI, K., SHIRAI, T. *Radial Force on the Impeller of a Centrifugal Pump*

[39] VAL S. LOBANOFF, ROBERT R. ROSS *Centrifugal pumps: design and application,* Second Edition USA 1992 577p ISBN 0-87201-200-X.

[40] World Pumps *A brief history of pumps* http://www.worldpumps.com/view/813/a-brief-history-of-pumps-/

[41] ZAVADIL, L. *Vyšetřování parametrů hydraulických strojů s využitím numerických metod.* ISBN 978-80-248-2691-2. 43p. VŠB-TUO 2012.

11. List of publications

[V1] PHAN, T. H. L. The transition of hydropower machine with influence of turbine characteristics. In *Transactions of Agriculture, Forestry and Fishing Conference 1st. Hanoi, 23-25 October 2003*, p. 154-158.

[V2] PHAN, T. H. L.; DRÁBKOVÁ, S. *Numerical modelling as a tool of centrifugal pump Q~H CURVE investigation*. Lutin Sigma Group a.s. 2008.

[V3] PHAN, T. H. L.; DRÁBKOVÁ, S. Vyšetření stability Q~H charakteristiky odstředivého čerpadla s využitím numerického modelování proudění. In *Sborník vědeckých prací Vysokké školy báňské – Technické univerzity Ostrava číslo 1, rok 2008, ročník LIV, řada strojní*. Ostrava 2008, p. 211-216. ISBN 978-80-248-1891-7.

Cooperation in grant projects:

DRÁBKOVÁ, S., PHAN, T. H. L.: FT-TA3/166 – Výzkum problematiky nestability *Q~H* charakteristik hydrodynamických čerpadel. *Zpráva o řešení dílčí části grantového úkolu*: Numerické modelování proudění v hydrodynamickém čerpadle. Ostrava, 2008. 9p.

12. Curriculum vitae

Name and surname: Tran Hong Long PHAN

Address: Jugoslávská 2847/53 Ostrava Zábřeh

Address in Vietnam: 27 KhuongThuong, Dong Da, Ha Noi.

Date of birth: 18-11-1980

Phone number: +420 773 063 598
+84 4 38532986

E-mail address: PHANLLQ@WRU.EDU.VN
PHANLLQ@GMAIL.COM

Marital status: married

Education:

2005-2012: Doctoral study programme at VSB

1998-2003: University education at Water Resources University, Hanoi, Vietnam

1995-1998: Chemical High school, Hanoi University of Science, Vietnam national university, Hanoi, Vietnam.

Working experiences:

2003-2005: Lecturer at Faculty of Hydropower, Water Resources University, Hanoi, Vietnam.

Software skills:

AutoCAD, Microsoft Office, C, Java, Turbo Pascal, ANSYS Fluent, ANSYS Gambit.

Languages:

Native: Vietnamese.
Intermediate: Czech, English.
Elementary: French.

13. Appendix

13.1. Appendix 1: The calculated model in chapter 5, 6, and 7

```
FLUENT
Version: 3d, pbns, sstkw, unsteady (3d, pressure-based, SST k-omega or k-
epsilon, unsteady or steady)
Release: 6.3.26
Title:

Models
------

   Model                        Settings
   ---------------------------------------------------------
   Space                        3D
   Time                         Unsteady, 1st-Order Implicit
   Viscous                      k-omega turbulence model
   Heat Transfer                Disabled
   Solidification and Melting   Disabled
   Species Transport            Disabled
   Coupled Dispersed Phase      Disabled
   Pollutants                   Disabled
   Pollutants                   Disabled
   Soot                         Disabled
Boundary Conditions
-------------------

   Zones

name                           id      type
      ------------------------------------------------------
difuser                        6       fluid
impeller                       17      fluid
intake                         65530   fluid
wall-12                        12      wall
wall-11                        11      wall
wall-4                         4       wall
wall-3                         3       wall
outlet                         9       mass-flow-inlet
      int_created_material_4         7       interior
difuserwall                    8       wall
difuserin                      10      interface
      int_created_material_15        18      interior
blade                          19      wall
impellerout                    20      interface
impellerin                     21      interface
hub                            22      wall
shroud                         23      wall
nut                            24      wall
distance                       25      wall
impelercircuit                 26      wall
      int_created_material_4.65529   65529   interior
intakeout                      65528   interface
      inlet                          65527   mass-flow-inlet
intakewall                     65526   wall
```

13.2. Appendix 2: The calculated model in chapter 8

```
FLUENT
Version: 3d, dp, pbns, sstkw, transient (3d, double precision, pressure-
based, SST k-omega, transient)
Release: 13.0.0
Title:

Models
------

   Model                        Settings
   -----------------------------------------------------
   Space                        3D
   Time                         Steady
   Viscous                      k-omega turbulence model
   Heat Transfer                Disabled
   Solidification and Melting   Disabled
   Species                      Disabled
   Coupled Dispersed Phase      Disabled
NOx Pollutants               Disabled
SOx Pollutants               Disabled
   Soot                         Disabled
   Mercury Pollutants           Disabled

Material Properties
-------------------

   Material: water-liquid (fluid)

      Property                        Units      Method     Value(s)
      ---------------------------------------------------------------
      Density                         kg/m3      constant   998.20001
Cp (Specific Heat)              j/kg-k     constant   4182
      Thermal Conductivity            w/m-k      constant   0.6
      Viscosity                       kg/m-s     constant   0.001003
      Molecular Weight                kg/kgmol   constant   18.0152
      Thermal Expansion Coefficient   1/k        constant   0
      Speed of Sound                  m/s        none       #f

   Material: air (fluid)

      Property                        Units      Method     Value(s)
      ----------------------------------------------------------------
      Density                         kg/m3      constant   1.225
Cp (Specific Heat)              j/kg-k     constant   1006.43
      Thermal Conductivity            w/m-k      constant   0.0242
      Viscosity                       kg/m-s     constant   1.7894e-05
      Molecular Weight                kg/kgmol   constant   28.966
      Thermal Expansion Coefficient   1/k        constant   0
      Speed of Sound                  m/s        none       #f

   Material: aluminum (solid)

      Property               Units    Method     Value(s)
      ---------------------------------------------------
      Density                kg/m3    constant   2719
Cp (Specific Heat)     j/kg-k   constant   871
      Thermal Conductivity   w/m-k    constant   202.4
```

13.3. Appendix 3: Design example with method 1D

This appendix is descried and calculated with typical method pump design.

This method is illustrated on the case of radial impeller with given parameters.

13.3.1. Basic parameters for the pump design

Discharge	$Q = 30\ dm^3.s^{-1} = 0.03\ m^3.s^{-1}$
Head water	$H = 27.8$ m
Speed	$n = 1\ 450$ round.min^{-1}= 24 round.second^{-1}
Density	$\rho = 1\ 000$ kg.m^{-3}
Allowed stress	$\tau_a = 15.10^6$ Pa

Specific speed:

$$Y = g\,H = 9.81 \cdot 27.8 = 272.718 \quad [J.kg^{-1}]$$

$$n_q = 330\frac{n\,Q^{0.5}}{Y^{0.75}} = 330\frac{24 \cdot 0.03^{0.5}}{272.718^{0.75}} = 20.6 \qquad (75)$$

$$n_s = 3.65 \cdot 330\frac{n\,Q^{0.5}}{Y^{0.75}} = 75.1 \quad [\min^{-1}]$$

This value (n_q = 20.6) corresponds to radial type of impeller, as can be seen from Figure 3 and Figure 4.

Efficiency was predicted using the following diagram (see Figure 69). Based on flow rate and specific speed the efficiency reaches the value of 73%.

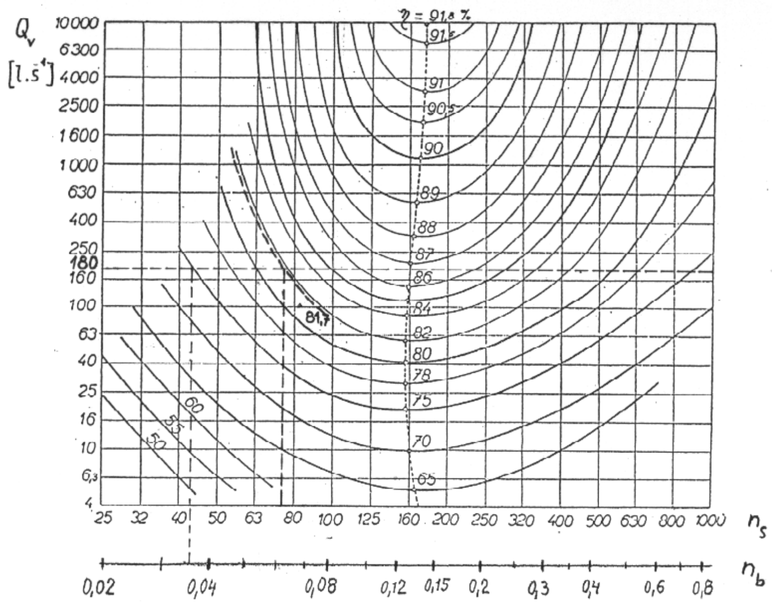

Figure 69 Efficiency based on flow rate and specific speed

Pump input power:

$$P = \frac{\rho Q Y}{\eta} = \frac{1000 \cdot 0.03 \cdot 272.718}{0.73} = 11207.6 \quad [W] \tag{76}$$

Electric motor input power (rounds the result down):

$$P_M = \kappa P = 1.34 \cdot 11207.6 = 15000\, W = 15 \quad [MW] \tag{77}$$

Shaft diameter is determined from load by torsion torque:

$$\begin{aligned} \omega &= \frac{\pi n}{30} = \frac{3.14 \cdot 1450}{30} = 151.84 \\ T &= \frac{P_M}{\omega} = \frac{15000}{151.84} = 98.8 \\ d_h &= \sqrt[3]{\frac{5T}{\tau_a}} = 0.032 \quad [m] \end{aligned} \tag{78}$$

Hub diameter:

$$d_n = 1.2 d_h = 0.0385 \quad [m] \tag{79}$$

Flow back:

$$q = 0.05 \cdot 0.03 = 0.0015 \quad [m^3 s^{-1}] \tag{80}$$

The velocity:

$$c_{m1} = k_{m1} \sqrt{2 g H} = 0.145 \sqrt{2 \cdot 9.81 \cdot 27.8} = 3.386 \tag{81}$$

where k_{m1} is coefficient, was calculating by equation:

$$k_{m1} = 0.12 + 0.5617 \left(n_b - 0.041\right)^{0.8} \tag{82}$$

Area of impeller‘s inlet:

$$S_1 = \frac{Q + q}{c_{m1}} = \frac{0.0315}{3.386} = 0.0093 \quad [m^2] \tag{83}$$

Also calculate by equation:

$$S_1 = \pi D_1 b_1 - S_{bl} = \pi D_1 b_1 - z \frac{s_1 b_1}{\sin \beta_1} = \varphi_1 \pi D_1 b_1 = \varphi_1 \frac{\pi \left(D_0^2 - d_n^2\right)}{4} \tag{84}$$

Then we have the eye diameter:

$$\begin{aligned} \varphi_1 &= 0.84 \\ D_0 &= \sqrt{\frac{4}{\pi} \frac{Q + q}{c_{m1} \varphi_1} + d_n^2} = \sqrt{\frac{4}{\pi} \frac{0.0093}{0.84} + 0.0385^2} = 0.125 \quad [m] \end{aligned} \tag{85}$$

Outlet diameter:

$$u_2 = k_u \sqrt{\frac{0.84}{\eta_h}} \sqrt{2gH} = 23.1$$
$$k_u = 0.98$$
$$\eta_h = \sqrt{\eta} - (0.02 \div 0.04) = \sqrt{0.73} - 0.03 = 0.8244 \tag{86}$$
$$D_2 = \frac{60 k_u \sqrt{\frac{0.84}{\eta_h}} \sqrt{2gH}}{\pi n} = \frac{60 \cdot 23.1}{3.14 \cdot 1450} = 0.3043 \quad [m]$$

Outlet area:

$$c_{m2} = k_{m2} \sqrt{2gH} = 0.103\sqrt{545.436} = 2.4$$
$$\varphi_2 = 0.93 \tag{87}$$
$$b_2 = \frac{Q+q}{c_{m2}\, \pi\, D_2\, \varphi_2} = \frac{0.0315}{2.4 \cdot 3.14 \cdot 0.352 \cdot 0.93} = 0.0147 \quad [m]$$

Diameter on the middle streamline:

$$\frac{D_1 - D_M}{D_0 - D_M} = f(n_s) = 0.63$$
$$D_M = \sqrt{\frac{D_0^2 + d_n^2}{2}} < D_1 < D_0$$
$$D_M = \sqrt{\frac{0.125^2 + 0.0385^2}{2}} = 0.0925 \tag{88}$$
$$D_1 = 0.63 \cdot (0.125 - 0.09235) + 0.09235 = 0.113$$
$$b_1 = \frac{\pi\, D_2\, b_2\, \varphi_2\, c_{m2}}{\pi\, D_1\, \varphi_1\, c_{m1}} = \frac{0.3043 \cdot 0.0147 \cdot 0.93 \cdot 2.4}{0.113 \cdot 0.84 \cdot 3.386} = 0.031$$
$$b_i = \frac{\pi\, D_2\, b_2\, \varphi_2\, c_{m2}}{\pi\, D_i\, \varphi_i\, c_{mi}}$$

Speed input u_1:

$$u_1 = \pi\, D_1\, n = 3.14 \cdot 0.113 \cdot 24.167 = 8.58 \quad [m.s^{-1}] \tag{89}$$

Input angle β_1:

$$\beta_1 = arctg\left(\frac{c_{m1}}{u_1}\right) = 21.53766^o \tag{90}$$

Determination of output angle β_2 is based on the Euler's equation:

$$\begin{aligned}
&\frac{Y}{\eta_h} = \kappa u_2^2\left(1-\frac{c_{m2}}{u_2}\tan\beta_2\right)\\
&\Rightarrow \beta_2 = \arctan\left(\frac{u_2}{c_{m2}}\left(1-\frac{Y}{\eta_h\,\kappa u_2^2}\right)\right) = f(\kappa)\\
&\kappa = 1.01-\frac{0.359+0.457\sin\beta_2}{\sqrt{z}} = g(z,\kappa)\\
&z = k\frac{r_s}{l_s}\sin(\beta_1+\beta_2) = h(\beta_2)
\end{aligned} \tag{91}$$

Number of blade:

$$z = \kappa\frac{D_2+D_1}{D_2-D_1}\sin\frac{\beta_1+\beta_2}{2} = 7 \tag{92}$$

Outlet blade angle:

$$\begin{aligned}
&\tan\beta_2 = \frac{c_{m2}}{u_2-c_{u2}}\\
&\beta_2 = 51.5662^o
\end{aligned} \tag{93}$$

The meridional geometry defined by 1D approach can be seen on Figure 70:

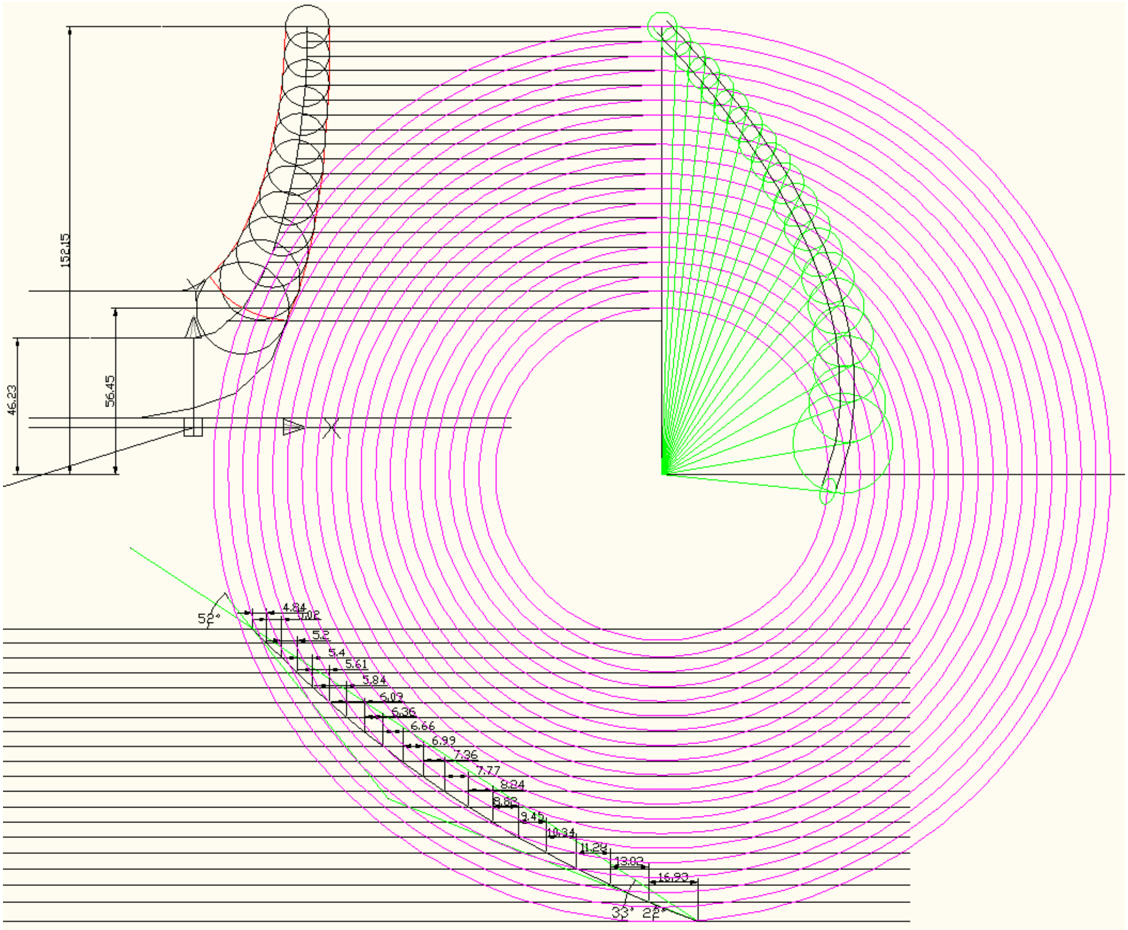

Figure 70 Scheme and section of blade 1D

13.3.2. Design of Spiral casing (volute) stator

The object of the volute is to convert the kinetic energy imparted to the liquid by the impeller into pressure. The spiral casing has no part in the (dynamic) generation of the total head and therefore deals only with minimizing losses [37].

For the design of spiral the Method of constant speed was applied.

$$c_4 = K_4 \sqrt{2Y_1} = 9.88 \quad [\mathrm{m.s^{-1}}] \tag{94}$$

with coefficient

$$K_4 = 0.45 - 2.015(\mathrm{n_b} - 0.049) = 0.4231[1] \tag{95}$$

Based on assumption that c_4 is constant, the cross-sections of volute were calculated given in Table 14. Circle shape was chosen as can be seen on Figure 71.

Table 14 Area of each cross-section due angle

			alpha	*r*	*S'*	delta *S*	*h*	r_a	diameter
			[rad]	[m]	[m^2]	[m^2]	[m]	[m]	[m]
S_8	0.0030	[m^2]	0.7419	0.0331	0.0030	-0.00000020	0.031	0.198	0.066
S_7	0.0027	[m^2]	0.7921	0.0311	0.0027	-0.00000026	0.029	0.196	0.062
S_6	0.0023	[m^2]	0.8543	0.0290	0.0023	0.00000023	0.026	0.193	0.058
S_5	0.0019	[m^2]	0.9346	0.0266	0.0019	-0.00000003	0.024	0.191	0.053
S_4	0.0015	[m^2]	1.0437	0.0241	0.0015	-0.00000002	0.021	0.188	0.048
S_3	0.0011	[m^2]	1.2049	0.0212	0.0011	0.00000004	0.017	0.184	0.042
S_2	0.0008	[m^2]	1.4816	0.0178	0.0008	-0.00000005	0.013	0.180	0.036
S_1	0.0004	[m^2]	2.1671	0.0136	0.0004	0.00000002	0.006	0.173	0.027

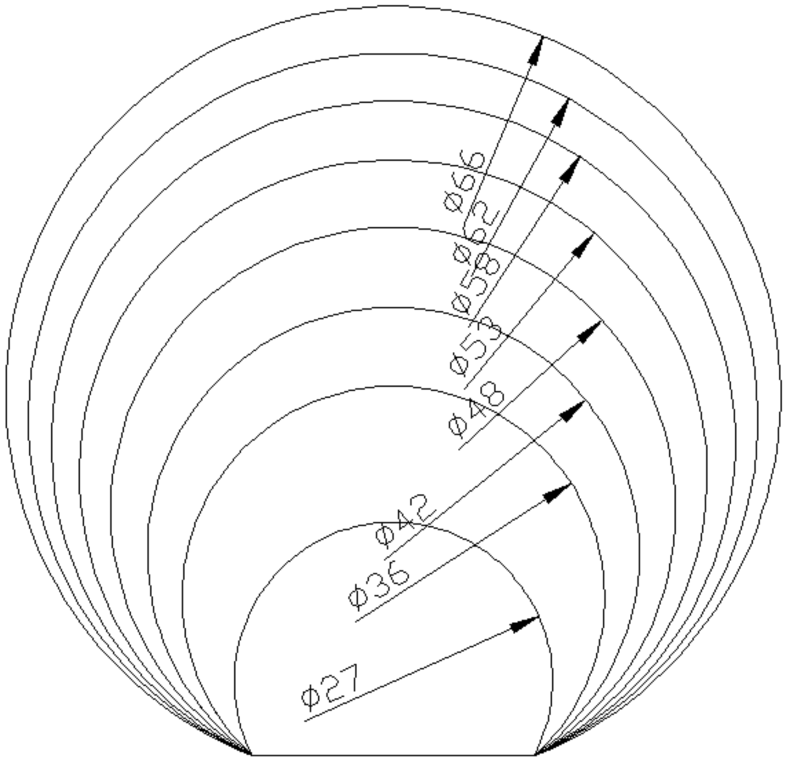

Figure 71 Scheme of spiral cross-sections (8 sections) – diameter in millimetre